Magnetic Resonance Imaging and Modeling of Brain Magnetic Susceptibility

Jingjia Chen

Electrical Engineering and Computer Sciences
University of California, Berkeley

Technical Report No. UCB/EECS-2024-7
http://www2.eecs.berkeley.edu/Pubs/TechRpts/2024/EECS-2024-7.html

February 7, 2024

Magnetic Resonance Imaging and Modeling of Brain Magnetic Susceptibility

By

Jingjia Chen

A dissertation submitted in partial satisfaction of the

requirements for the degree of

Doctor of Philosophy

in

Engineering - Electrical Engineering and Computer Sciences

in the

Graduate Division

of the

University of California, Berkeley

Committee in charge:

Professor Chunlei Liu, Chair
Professor Michael Lustig
Professor Steven Conolley
Assistant Professor An Vu

Spring 2023

Magnetic Resonance Imaging and Modeling of Brain Magnetic Susceptibility

Abstract

Magnetic Resonance Imaging and Modeling of Brain Magnetic Susceptibility

by

Jingjia Chen

Doctor of Philosophy in Engineering - Electrical Engineering and Computer Sciences

University of California, Berkeley

Professor Chunlei Liu, Chair

In magnetic resonance imaging (MRI), the human body's magnetic susceptibility causes a slight resonance frequency shift of the nuclear spins. This frequency shift is reflected in the phase of MRI signals. By solving a magnetic dipole model using the frequency shift map, we can recover the tissue's local magnetic susceptibilities using a method called quantitative susceptibility mapping (QSM). However, QSM is inaccurate if non-homogeneous magnetic susceptibility sources exist within one imaging voxel. To address this issue, we developed a compartmentalized tissue signal model named DECOMPOSE-QSM.

The DECOMPOSE-QSM considers three susceptibility components within one imaging voxel: paramagnetic component, diamagnetic component, and neutral component which is serving as the susceptibility reference. The multi-echo gradient echo signal of a voxel with a susceptibility mixture can be expressed as the summation of the complex single exponential signal coming from each component. By solving for the parameters that characterize this summation of three complex exponentials, paramagnetic and diamagnetic component susceptibility maps can be resolved. An optimization-based solver is proposed to solve this highly non-linear model. The solver alternates between solving three sub-problems: 1) a constraint linear least square problem, 2) a log-modified constraint linear least square problem, and 3) a log-modified nonlinear constraint least square problem. Additionally, in an attempt to accelerate the calculation, a deep learning-based solver is developed, which uses a multi-layer perceptron framework to explore the signal model's behavior in higher dimensions. The DECOMPOSE-QSM is validated by imaging susceptibility mixture gel phantoms made in-house and verifying the Curie's Law relation for the paramagnetic components with a series of temperature-varying imaging experiments.

Using the DECOMPOSE-QSM technique, the anisotropic paramagnetic susceptibility in the brain was discovered with a multi-orientation dataset on a postmortem chimpanzee brain. The paramagnetic susceptibility anisotropy is believed to be reflecting a microstructural order of oligodendrocytes wrapping around axons. The anisotropy due to the arrangements

of oligodendrocytes has been observed in previous studies using polarized light imaging. Our finding is the first observation of such anisotropy using an MRI-based technique.

To my family and my friends.

Contents

List of Figures

List of Tables

Acknowledgments

Throughout this incredible journey, I am profoundly grateful to the numerous people who have supported me, encouraged me, and shaped who I am today. It is a challenging task to acknowledge everyone in just a few pages, but I will do my best to express my appreciation for as many individuals as possible.

To my parents, thanks for providing a safe and worry-free environment for me and for fostering my early interest in science. Thanks for being awesome, hardworking, inspiring, and encouraging me through my endeavor. Thanks for answering calls at midnight or the crack of dawn during my most difficult times.

To my advisor Chunlei Liu, thanks for this life-changing experience and thanks for the trust and encouragement throughout this journey. Chunlei's knowledge, curiosity, humility, work ethic, and commitment have served as an exceptional example of what a dedicated researcher should be. He is very open to all the topics I am interested in and he is always there giving me advice whenever I feel stuck. And most importantly and magically to me, his suggestions almost always work. He is always in his office and he is always working. He always tries his best to allocate time for my meeting requests in addition to our weekly 1-1 hour. Thanks to his diligence, funding has never been an issue for us and I was given a lot of flexibility to find my thesis topic and for trial and error. I am very grateful to be his student and to have had the chance to work with him. I would not have gained so much in research, in life, and in every aspect without his patience, care, and support. During these six years in Berkeley, we have had many cups of boba and plates of beef stew rice together. I will remember to have a big goal in mind when doing research and "have boba from time to time to keep good mental health".

My thanks go to my committee members, Miki Lustig, An (Joseph) Vu, and Steve Conolly, for their valuable input, advice, and support. To Miki, thank you for sponsoring our servers, and lab space and getting us the scanner with Chunlei. Thank you for showing me how to stay curious and excited about the world while being disciplined, persevering, and awesome at work. Thank you for the time you spent chatting with me and sharing your experiences and advice. To Joseph, thank you for teaching me to scan on the 7T systems at Berkeley and UCSF, for spending time with me to discuss fMRI research, and for your comments on this dissertation. Your tip of taking frequent naps to enhance memory when preparing for a talk has greatly helped me and I wish everyone knows about this strategy. To Steve, thanks for your continuous support from day one, for many meetings and emails of advice on academic career development, and for insights into this dissertation.

I have been fortunate to work alongside an incredible group of labmates and researchers. Some of us became really good friends. To Victor, thank you for being my labmate for the past six years. Thanks for showing me how to use the HeartVista system and for answering my random questions all the time. To Miriam, thank you for brainstorming phantom fabrication ideas with me and for teaching me neuroscience basics. I will not forget the story of me leaving my ID in the fridge and the story of us with Victor figuring out how to handle the human brain samples. Thank you for appreciating my code for the cell

imaging analysis for your brilliant experiments. Thank you for attending all of my chorus concerts. Thank you for being so inspiring, supportive, and encouraging all the time. To Hongjiang and Yuyao, thank you for introducing me to QSM and sharing your experiences and visions in this field. Though you moved to Shanghai after my first year at Berkeley, thank you for your continuous support through chats and emails. To Maruf, thanks for all the discussions we had and for carrying on projects applying the DECOMPOSE-QSM for Alzheimer's Disease. Thank you for showing me Bangladesh food. To Tanya, thanks for bringing so much energy and cheerfulness to the lab. Thanks for hosting me when I was visiting Turkey. Thanks to Zoe for the coffee sessions we had at the beginning of the COVID-19 quarantine time. Thanks to Koyam for being so kind and for the discussions on how we can best detect and quantify neuron spikes for your electrophysiology data. I would also like to thank some of the undergraduate researchers and visiting scholars. Thank you Samantha for all the science and culture discussions, and food exploration we had together. Thanks for being by my side when I needed it the most. To Steven, thank you for being talented, and brilliant while being so humble and fun around people. Thanks for always thinking of me and having food with me whenever you are back visiting Berkeley. Thanks, Xiaojun, for sharing your insights on how to write a good paper. Thanks, Engin, for being so happy and positive all the time.

My experience at Berkeley would not have been the same without the camaraderie and support of Miki Lustig's group. I have been sharing office space, lab, and computing resources with them for the past six years. Thank you for always bringing me along to every single group event. Over the years, Miki has inspired me, helped me, and enlightened me in many different aspects. Thank you, Jon, for the advice and chats when I was confused about my direction. To Suma, thank you for teaching me how to use the BART toolbox, many times. Thank you for our long cubicle chats about almost everything. Thank you for training and running our first-ever half marathon together. Thank you for being so kind and open to me. Thank you, Ekin, for answering my random MRI sequence questions. Thank you for always being so warmhearted and always carefully preparing for everyone's birthday (surprises). Thanks to Ke for being my deskmate, for so many discussions about academia, research, and history, and for always encouraging me. To Shreya, thank you for being so happy and full of smiles all the time. To Alfredo, thanks for being a great collaborator, for helping me with my first deep learning project with your broad experiences and intuitions, and for being my ski guide. Thanks to Rebekah for so many chatting, hiking, and food exploration sessions with me during the COVID-19 pandemic. Thanks to Efrat for showing me the value of being hardworking and proactive. Thank you for introducing me to paddle boarding. Thanks to Julian for showing me what a passionate researcher looks like. Thanks to Karthik for setting up the lab space and for encouraging me to go skiing. Thank you Frank for teaching me your multi-scale low-rank work and helping me apply it to fMRI analysis. Thanks to Jon, Alan, Ke, and Alfredo for setting up and maintaining our servers.

This dissertation would not have happened without the support of my amazing collaborators around the world. It is my honor to be able to work with you all. Thanks to Maria Concepcion Garcia Otaduy from the University of Sao Paulo for performing the scans for

the temperature-varying brain stem dataset. It was one of the key validations of this dissertation. Thanks to Harald Moeller and Dimitrios Gkotsoulias from the Max Planck Institute for Human Cognitive and Brain Sciences for the valuable multi-orientation chimpanzee ex vivo dataset which makes up a part of this dissertation. Thank you for making it to our monthly discussions over Zoom for the past two years. Thank you, Karin Shmueli and Patrick Fuchs from the University College London, for performing reproducibility tests for the DECOMPOSE-QSM. Thank you, Alex Beckett, Sam Torrisi, and Jennifer Townsend at UC Berkeley, for helping me perform lengthy 7T scans on the postmortem human brains hours after hours, days after days.

My time at Berkeley has been enriched by the remarkable people I have encountered. Thanks to Dilveen Goraya, Thuc Tran, and Maryann Rui for showing me around Berkeley and the Bay Area in my first year. Thanks to Efe Aras for being my friend and being by my side to support me whenever I need it. Thanks to Philip Lee for those chats about academia, coffee, puns, jokes, and cats. Thanks to Soham Phade for swimming and running with me. Thanks to Orhan Ocal for showing me that one can do stressful work but still enjoy life. Thanks to Lakshya for being my EECS 126 study partner. Thanks to Daniel for being supportive and keeping my spirits and motivation high. Thanks to Tarang Srivastava and Michael Psenka for co-teaching the CS 70 with me. It was a pleasure working with you.

I have spent the first 22 years of my life in one city, Nanjing, China. Thanks to my friends who are from my hometown but now living in the U.S.: Menglu Cao, Wen Cong, Luyan Yu, Yu Wu, Xiaoxi Huang, Enze Cheng, Rongbing Zhou, and Qihui Lyu. Thank you for reminding me who I am and who I want to be. It is not easy to move across the globe, but I am lucky to have you all with me.

My time at Berkeley has been transformative and rewarding, and I am forever grateful to everyone who has been a part of it. Thank you all.

Chapter 1

Introduction

1.1 Magnetic Resonance Imaging

A compass can indicate north because the magnetized needle has the tendency to be aligned with the Earth's magnetic field. It turns out that the proton (^{1}H, the hydrogen nucleus in water molecules) behaves just like a little magnet.

Under a static magnetic field, the proton (hydrogen nucleus) tends to align with the field and its intrinsic angular momentum (or 'spin') precesses about the field at the "Larmor frequency" $\omega = \gamma B_0$, where γ is the gyromagnetic ratio. For a proton, γ evaluates to 42.58 MHz/T. If only a static B_0 field exists, a parallel alignment of the proton will reach an equilibrium. When a transient radiofrequency (RF) magnetic field at the Larmor frequency is introduced to the system of aligned spins, the spins will absorb the RF energy, and through a resonating mechanism will feel a torque. The torque will push the spin slightly away from being parallel with the B_0 direction and the spin will start precessing. Despite the proton spin itself and the resonating and precessing of a spin being quantum phenomena, a classical description can be used to understand the mechanism of MRI. The motion of precession can be imagined as a spinning gyroscope being pushed a little bit. The gyroscope will continue spinning but now about a rotating axis. Eventually, since there is a static B_0 field, the spins will re-align and reach equilibrium again. This process of returning to the parallel alignment state is often called "relaxation". We can use a three dimensional vector $\mathbf{M}(t) = M_x(t)\hat{\mathbf{x}} + M_y(t)\hat{\mathbf{y}} + M_z(t)\hat{\mathbf{z}}$ to describe the spin dynamics where $\hat{\mathbf{z}}$ is defined as the B_0 direction which the spins are rotating about. As the spins go through relaxation, $M_z(t)$ in the longitudinal axis recovers while M_x and M_y in the transverse plane decay.

Different parts of the human brain contain different tissue compositions, creating a varying micro-environment where the water protons will have relaxation at various rates. The precession of spins (little magnets) will induce current flowing in the receiver coils (Lenz's Law). When the precession of spins disperses due to variations in the local tissue composition, the signal received from the coil will reflect such relaxation differences. Specifically, if the pulsed RF field is applied every TR period, and the sampling is always taken at a certain

time TE after each RF pulse, the received signal is proportional to the magnitude of the transverse magnetization M_{xy}. The MR signal is usually represented as a complex quantity and written as $M_{xy} = M_x + iM_y$, where i is the complex unit. The M_x and M_y are measured with orthogonal channels and $\sqrt{M_x^2 + M_y^2}$ gives the magnitude in MRI; $\angle(M_{xy}, \hat{\mathbf{x}})$ gives the phase in MRI.

1.2 Organization

This dissertation is concerned with complex (both magnitude and phase) MRI signal modeling to reveal magnetic susceptibility in the brain. Chapter 2 reviews the contribution of magnetic susceptibility to the formation of MRI signals and common MRI contrasts for revealing biological tissue's magnetic susceptibility. Chapter 3 introduces DECOMPOSE-QSM, a voxel signal model, and an optimization-based solver for resolving paramagnetic and diamagnetic susceptibility mixtures. Chapter 4 provides two validation experiments for the DECOMPOSE-QSM. Chapter 5 discusses the potential clinical applications for DECOMPOSE-QSM in degenerative diseases. Chapter 6 extends the DECOMPOSE-QSM to the susceptibility tensor model and describes the recovery of the paramagnetic susceptibility anisotropy using MRI-based techniques. Chapter 7 considers the practical impact of pre-processing methods on the results of DECOMPOSE-QSM and susceptibility tensor imaging. Chapter 8 describes a multi-layer perceptron framework for accelerating the parameter fitting process of the DECOMPOSE-QSM. Chapter 9 provides potential applications and future directions. Chapter 10 is an appendix for details of derivations and calculations for the DECOMPOSE-QSM model.

Chapter 2

Magnetic Susceptibility in MRI

2.1 Magnetic Susceptibility of Biological Tissue

The human body consists of many different types of molecules, and each one of them contains a different atomic configuration. The electron cloud of each molecule can be polarized under the strong static B_0 field. A physical quantity called volume magnetic susceptibility describes how much a certain type of tissue can be polarized by the main static field. A piece of tissue with susceptibility χ under static field B_0 generates a magnetization field $m \approx \chi B_0/\mu_0$. This induced magnetization perturbs the main B_0 field, causing field inhomogeneity and further affecting the MRI signal. For a region with high magnetic susceptibility, the magnitude of the MRI signal will decay faster due to the field inhomogeneity, and the magnetization field will manifest as spatial variation in the phase of the MRI signal.

In biological tissue, there are mainly two types of magnetic susceptibilities, paramagnetism and diamagnetism. Though the electron's magnetic susceptibility is a quantum effect fundamentally, the classical macroscopic form of Maxwell's equations and the classical electron orbital description is enough to understand this phenomenon and predict a material's behavior under a magnetic field (Figure 2.1).

The electron's spin is like a tiny magnet. Note that the spin we are concern with here is an electron spin, not a proton spin described in Chapter 1.1. Proton spins generate MR signals, while electron spins perturb the magnetic field (B0 field) causing changes in proton spins' relaxation. Based on Pauli's Exclusion Principle, two electrons with different spin quantum numbers ($m_s = +1/2$ or $-1/2$) can reside at one atomic orbital (i.e. for one set of principal, azimuthal, and magnetic quantum numbers) together, and we define these two electrons as paired. On the other hand, electrons with the same magnetic quantum number can not be at one atomic orbital together. An electron that occupies an orbital singly is called an unpaired electron. When the electrons are fully paired in an atom, the total net magnetic moment is zero. The B_0 field will induce the movement of the electrons generating a magnetic moment that is in the opposite direction of B_0 (Lenz's Law). The generated magnetic moment locally weakens the main B_0 field, and this is the origin of diamagnetism

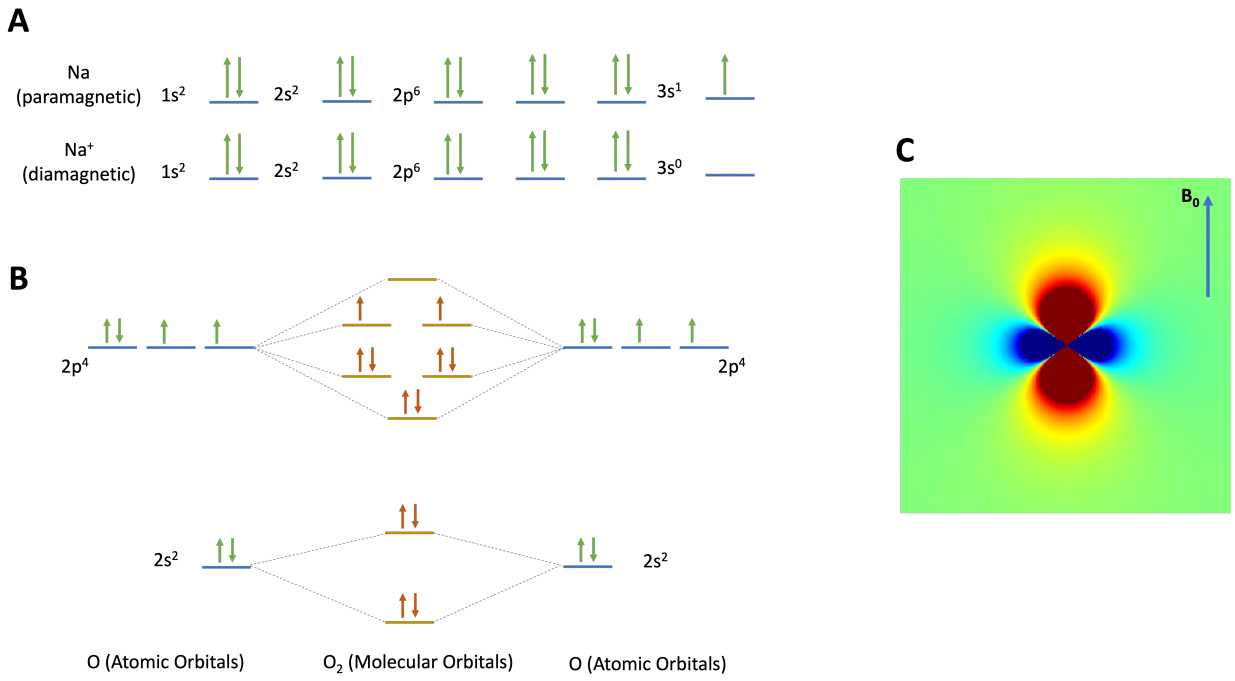

Figure 2.1: **Examples of magnetic susceptibility.** A) The atomic orbital configuration suggests that Na atom is paramagnetic (due to the unpaired 3s single electron) while the Na^+ ion is diamagnetic (all the electrons are paired). B) Using molecular orbital theory, the oxygen molecule O_2 has unpaired electrons at the p molecular orbital, therefore O_2 is paramagnetic. C) The shape of the magnetic dipole moment z component field under B_0.

($\chi < 0$). When there are unpaired electrons, the classical description says that the net magnetic moment is non-zero. Therefore, the unpaired electron spin will experience a torque induced by the B_0 field and align the electron's magnetic moments (dipoles) with the B_0 field. This will locally strengthen the B_0 field, and this is the origin of paramagnetism ($\chi > 0$). The torque turning dipole moments to align with the B_0 field takes thermal energy from the environment, therefore, the paramagnetism is temperature dependent (Curie's Law).

Most biological molecules are diamagnetic and the differences in susceptibility among those are on the order of $10^{-6} \sim 10^{-5}$. Therefore the field inhomogeneities due to the susceptibility distribution of the tissue are on the order of ppm. The human brain consists of 80% water [90]. Although water is slightly diamagnetic ($\chi < 0$), in MRI, we usually use water as the susceptibility reference ($\chi_{\text{water}} := 0$). In this way, oxygenated hemoglobin and other iron-rich tissue are paramagnetic ($\chi > 0$). Myelin lipid, most proteins, and calcification are then diamagnetic ($\chi < 0$).

2.2 Gradient Recalled Echo MRI Signal

An MRI scanner acquires tissue signals from echoes. Either RF or gradient pulses can be used to form such echoes. After the quick excitation RF pulse with a certain flip angle choice (e.g. 90°), the spins have the tendency to recover while going through a dephasing process. After a certain period of time T, if a 180 ° pulse is applied, the spins will then dephase in the opposite direction and refocus after another period of time T, and an echo of the signal is then formed. Since this refocusing is caused by the RF pulse, all the dephasing effects during the initial time period T will be reversed and eventually cancel out after another time period T.

Gradient recalled echo (GRE) imaging uses gradients to create such an echo of the signal. After the excitation pulse with a certain flip angle choice α, a gentle gradient is applied to intentionally dephase the spin for a certain period of time T followed by another same gentle gradient but with different polarity for another time period T. In this way, the dephasing caused by the first gradient with T duration is then reversed by the second opposite gradient, and an echo is formed. This process can be repeated to create multiple echoes so long as there is still enough signal intensity to be recorded (Figure 2.2). Compared to the spin-echo formation, in the gradient echo case, only the dephasing effect due to the first gradient is recalled by the second gradient, therefore, any other dephasing effects for example due to susceptibility (or B_0 field nonuniformity in general) are preserved in the signal envelope.

At voxel $\mathbf{r}$ with field nonuniformity $\Delta B(\mathbf{r})$ under B_0 field, the GRE signal received by a receiving coil tuned at Larmor frequency $\omega_0 = \gamma B_0$ can be described as

$$S(t) = \int m_0(\mathbf{r}) e^{-R_2(\mathbf{r})t} e^{-i\omega_{\Delta B}(\mathbf{r})t} d\mathbf{r} \tag{2.1}$$

where $R_2(\mathbf{r})$ is the transverse relaxation rate ($R_2 = 1/T_2$), $\omega_{\Delta B}(\mathbf{r}) = \gamma \Delta B(\mathbf{r})$ is the frequency distribution due to field inhomogeneity and further causes the spins at location $\mathbf{r}$ to presses out of phase and lose coherence.

A common *in vivo* case of strong susceptibility GRE signal effect is the chemical shift between water and fat. However, in the human brain MRI, this is usually ignored due to the high concentration of water and a negligible amount of fat. In the case of a strong fat signal (e.g. body MRI), water-fat separation needs to be performed (using the 3.5 ppm water-fat resonant frequency difference) before performing other susceptibility-related calculations.

2.3 Apparent Transverse Relaxation Rate (R_2^*)

If the field is perfectly uniform within the imaging voxel, after the excitation pulse, every spin will experience the same relaxation process and the spectrum line will be a very thin peak. Now that there is field imperfection (non-uniformity), the spectral will be widened. This spectral line broadening reflecting the inhomogeneity is called R_2^* effects. Integrating Eq. 2.1 over an imaging voxel, due to the field variation across this voxel, the collective total

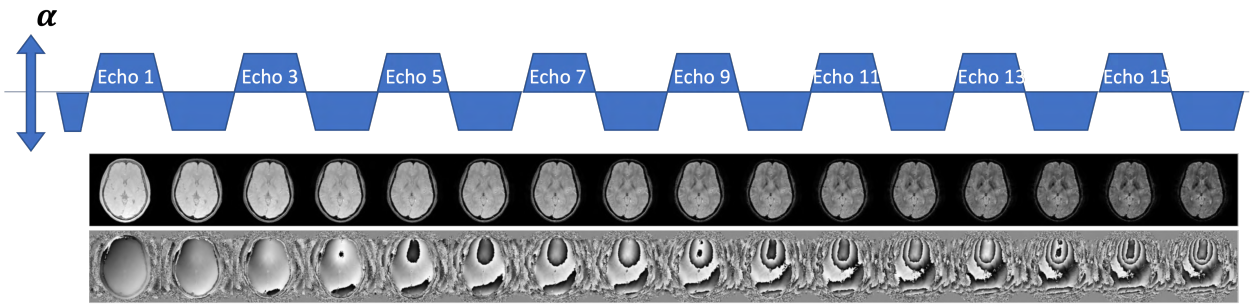

Figure 2.2: **16-echo bipolar GRE sequence scan of a human brain.** After the excitation RF with flip angle α, a small gradient (with the duration to be half of the readout time of each echo) is applied to dephase the spin. Gradients with bidirectional polarities are applied to refocus the spin 16 times. The magnitude images of each echo are shown in the first row; as it gets to the later echoes, the magnitude image gets darker. The corresponding phase of each echo is shown in the second row; as it gets to the later echoes, the phase has more wraps.

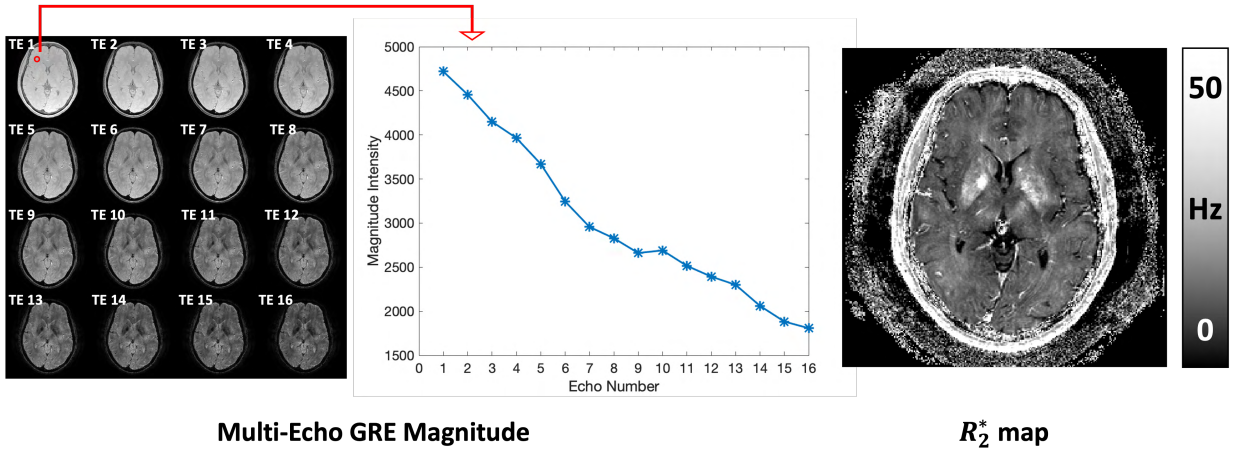

Figure 2.3: R_2^* **reconstruction using multi-echo GRE magnitude images.** Magnitude signal of each imaging voxel of the multi-echo GRE follows exponential decay. R_2^* can be obtained by fitting the magnitude images with corresponding echo times to Eq. 2.2.

signal magnitude will decay faster than the intrinsic $R_2 = 1/T_2$ indicates. This effective signal decay rate is referred to as the apparent transverse relaxation rate $R_2^* = 1/T_2^*$. By choosing a proper flip angle, TE, and TR combination, this susceptibility-induced signal magnitude effect can be observed using GRE imaging sequences. The flip angle is chosen to be the Ernst angle ($\alpha = \cos^{-1}(e^{TR/T1})$) for the best magnitude signal intensity based on the lowest possible TR. According to Eq. 2.1, the R_2^* is best observed when the echo time TE is on the order of the $T_2^* = 1/R_2^*$ of the tissue.

To recover the R_2^* mapping (Figure 2.3), at least two echoes of GRE images are needed to fit the signal equation of voxel at $\mathbf{r}$

$$|S(\mathbf{r}, t)| = m_0(\mathbf{r})e^{-R_2^*(\mathbf{r})t} \tag{2.2}$$

2.4 Susceptibility Weighted Imaging (SWI)

The slight variation of susceptibility can create a phase effect in the GRE signal as well. Consider a spin sitting very close to a magnetic susceptibility source, due to the perturbation from the induced magnetization field, the spin will feel a slight change in the magnetic field. Therefore the resonance frequency will change slightly accordingly, i.e. this spin might be processing slightly faster or slower than the ^{1}H's Larmor frequency at the B_0. In this case, the phase of GRE signal can be expressed as

$$\phi(\mathbf{r}, t) = -\gamma \Delta B(\mathbf{r})t \tag{2.3}$$

Susceptibility weighted imaging (SWI) [50] is a technique to enhance vessel and iron content in the magnitude gradient echo images by the susceptibility's phase effect.

In most of the cases of *in vivo* imaging, the phase effect is not only caused by local tissue susceptibility, far away susceptibility source. This part of the non-local field is called the background field. In SWI, a simple high pass filter is enough to remove the slowly varying background field.

After filtering out the background phase, the local phase is threshold filtered and rescaled to 0-1 range so that only the paramagnetic vein will be preserved. The magnitude T_2^* weighted GRE image is then enhanced by multiplying this phase multiple times (the number can be empirically chosen, and typically 4 times of this multiplication is performed) to produce the SWI images (Figure 2.4). Further, by minimum intensity projection (mIP), a venogram can be created.

The thresholding-scaling filter can be suboptimal for enhancing vein structures, especially for the reason that the phase accrual of a cylindrical vein may be > 0 depending on the angle between the vein and B_0. A previous study by *in silico* simulation has shown that an asymmetric triangular phase mask is more appropriate to visualize venograms using SWI [22].

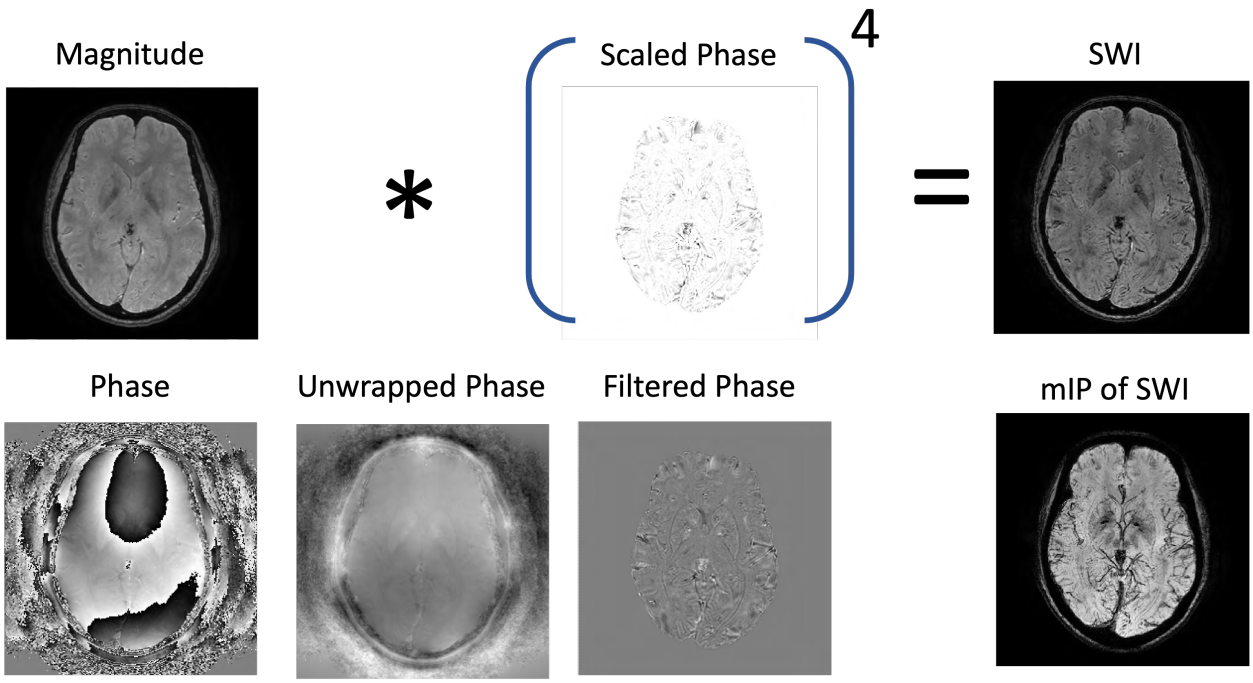

Figure 2.4: **Susceptibility weighted imaging (SWI) reconstruction pipeline.** Raw phase from the GRE acquisition is first unwrapped and then high-pass filtered to remove the slow varying background phase. Threshold the filtered phase by 0 to create a vein mask. The mask is re-scaled such that the value < 1 for vein, and 1 otherwise. The scaled phase mask is then multiplied with the magnitude for four times to create the SWI. The minimum intensity projection (mIP) of SWI along the axial dimension shows the vesicular tree structure of the human brain.

2.5 Quantitative Susceptibility Mapping (QSM)

Quantitative Susceptibility Mapping (QSM) [78, 95] takes a step further from the SWI. It models the underlying relation between local susceptibility, the local tissue field, and the local phase.

As described before, the phase of the GRE signal is caused by both the background field and the local tissue field. While visually the background field is mostly slow varying (spatially), a simple high pass filter used in SWI will suppress some of the local tissue field caused phase as well. A proper physical model needs to bridge the measured GRE phase and the local tissue field. Luckily, within the volume of interests (VOI), the background field originated from outside the VOI and can be characterized as a harmonic field [7] therefore

it follows the Laplacian equation.

$$\begin{aligned} \phi_{total} &= \phi_{local} + \phi_{background} \\ \nabla^2\phi_{background} &= 0 \quad \text{(background phase is harmonic)} \\ \nabla^2\phi_{total} &= \nabla^2\phi_{local} \end{aligned} \tag{2.4}$$

Solving the last partial differential equation with appropriate boundary conditions, the local tissue field can be recovered.

Alternatively, we can explore the properties of the harmonic function, and one of them is the mean value property. The average value of a harmonic function over a ball or sphere is equal to the value at the center of that sphere. In order to directly recover the local tissue phase many methods are proposed to filter out the background based on the harmonic function description of the background field or the mean value property of the harmonic function.

$$\int_{\partial Ball_r(x)} \phi_{background}\, dS = \phi_{background}(x) \quad \text{(mean value property)} \tag{2.5}$$

The process of moving the sphere across the whole VOI can be described as a convolution of a ball ($Ball\circledast$)

$$\begin{aligned} \phi_{total} &= \phi_{local} + \phi_{background} \\ \phi_{total} - Ball \circledast \phi_{total} &= \phi_{local} - Ball \circledast \phi_{local} \\ (\delta - Ball) \circledast \phi_{total} &= (\delta - Ball) \circledast \phi_{local} \\ \phi_{local} &= (\delta - Ball) \circledast^{-1} \{(\delta - Ball) \circledast \phi_{total}\} \end{aligned} \tag{2.6}$$

Therefore, by convolving and deconvolving this $\{\delta - Ball\}$ kernel with the total field, only the local phase will survive in the end.

With the local tissue field, QSM can non-invasively quantify the tissue magnetic susceptibility [14, 32, 67, 78, 77, 121]. A common used quantitative model to link the underlying susceptibility and the local tissue field is the magnetic dipole modelEq. 2.7.

$$\Delta B(\mathbf{r}) = \chi(\mathbf{r}) \circledast d(\mathbf{r}) \tag{2.7}$$

The total tissue field is written as a summation of all the B_0 induced magnetization dipole field of each voxel: a convolution between the underlying susceptibility distribution and the magnetic dipole kernel. To recover the underlying susceptibility distribution $\chi(\mathbf{r})$ using single orientation GRE measurements, an optimization problem of the following needs to be solved

$$\chi(\mathbf{r}) = \arg\min_{\chi} \| \mathrm{FT}^{-1}\{D(\mathbf{k})X(\mathbf{k})\} - \phi_{local} \| + \lambda R(\chi) \tag{2.8}$$

where $D(\mathbf{k})$ is the Fourier transform of the dipole kernel, $X(\mathbf{k})$ is the Fourier transform of the susceptibility distribution and $\mathrm{FT}^{-1}\{\cdot\}$ is the operation of inverse Fourier transform. The kernel itself is heavily ill-posed, and the term of $R(\chi)$ is the regularization term to control

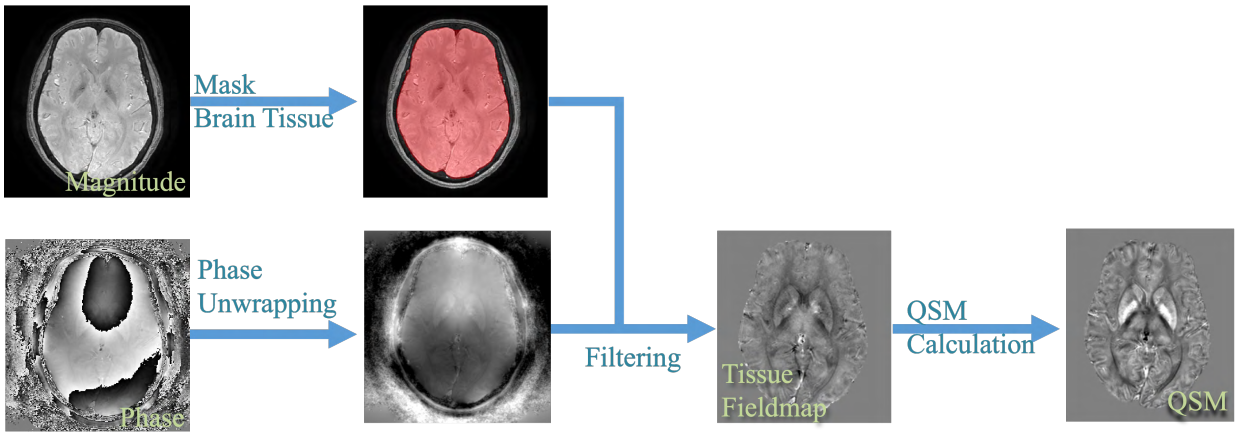

Figure 2.5: **A standard pipeline of the single orientation QSM calculation.** Magnitude GRE image of the brain is used to create a brain tissue mask that is later used to define the volume of interest during background field removal. The raw phase is unwrapped and filtered to reveal the local tissue field map. Dipole inversion is performed according to Eq. 2.8 to calculate the QSM.

the artifacts rising from inverting the ill-conditioned dipole kernel (e.g. STAR-QSM[123], iLSQR-QSM[68], MEDI-QSM[81], etc. and deep learning based approaches [40, 135, 58]). However, any regularization involves some level of parameter tuning and might cause a smoothing effect. If feasible, multi-orientation GRE measurements can be used to recover QSM without regularization strategy (COSMOS-QSM[80]).

Tissue susceptibility change is involved in normal aging and many disease developments in the brain. QSM has shown superior contrast and potential utilities in revealing iron level alternation in brain aging processes [13, 14, 140], imaging myelination during brain development [5, 140], imaging protein accumulations in Alzheimer's disease (AD) [44], uncovering dysmyelination [76] and demyelination in multiple sclerosis (MS) [26, 120, 128, 139], enhancing contrast of calcifications [33, 112, 119] as well as developing biomarkers for Parkinson's Disease (PD) diagnosis [9, 48, 49, 47, 55, 86, 106].

2.6 Susceptibility Tensor Imaging (STI)

Biological tissue's bulk magnetic susceptibility can be measured non-invasively through QSM. The tissue microstructure of an imaging voxel is very complex. In many brain regions, the measured susceptibility depends on the angle between the underlying structure and the B_0 field direction[71, 125, 126]. Similar to the description of diffusivity anisotropy, susceptibility anisotropy can be described by a second-order tensor. Using susceptibility measurements at multiple B_0 orientations, the second-order susceptibility information can be characterized

using the susceptibility tensor model, namely the method of susceptibility tensor imaging (STI) [74]. It has been shown that the major contribution to susceptibility anisotropy is from the radially arranged myelin lipids concentrically wrapping around the axon. Therefore, STI is able to reflect the orientations of white matter (WM) fiber tracts [71, 75, 124].

For tissue with anisotropic magnetic susceptibility, the susceptibility is no longer described by a scaler but by a second-order tensor. The MR field perturbation caused by anisotropic magnetic susceptibility tensor $\overset{\leftrightarrow}{\chi}$ can be written as follows,

$$\theta(t) = \mathrm{FT}^{-1}\Big\{\frac{1}{3}\hat{\mathbf{H}}^T\mathrm{FT}\{\overset{\leftrightarrow}{\chi}\}\hat{\mathbf{H}} - \hat{\mathbf{H}}\cdot\mathbf{k}\frac{\mathbf{k}^T\mathrm{FT}\{\overset{\leftrightarrow}{\chi}\}\hat{\mathbf{H}}}{k^2}\Big\}\gamma B_0 t \tag{2.9}$$

where θ is the phase of gradient echo MR signal at certain sampling echo time t, $\hat{\mathbf{H}}$ is the vector representing B_0 field with the magnitude being H, k is the frequency space coordinate, χ is the macroscopic susceptibility tensor described as a real-valued 3×3 matrix, γ is the gyromagnetic ratio, and $\mathrm{FT}\{\cdot\}$ means the Fourier transform operation. The relation in Eq. 2.9 is defined in the subject reference frame It can also be written in the lab frame (the scanner frame) as

$$\theta(t) = \mathrm{FT}^{-1}\Big\{\frac{1}{3}\mathrm{FT}\{\chi_{33}\} - \frac{1}{3}\frac{\mathbf{k_3^2}}{k^2}\mathrm{FT}\{\chi_{33}\}\Big\}\gamma B_0 t \tag{2.10}$$

According to Eq. 2.10, the rotation of the sample with respect to the B0 direction (z-axis) corresponds to the rotation of the susceptibility tensor. Specifically, Measured Susceptibility $= \chi_{33} = R\ \overset{\leftrightarrow}{\chi}\ R^T$. R is the rotation component of the transformation matrix from each direction to the reference direction.

The inverse problem of the STI model is intrinsically ill-posed when the range of angles is limited. Various approaches have been proposed to improve the robustness of reconstructing STI while mitigating the artifacts. Generally, three types of regularizations are used: 1) using DTI or susceptibility to provide morphological prior in order to improve the STI reconstruction [8, 73, 127]; 2) updating the STI model by allowing the antisymmetric artifact component[24, 104]; 3) data-driven STI reconstruction using deep neural network[39].

Chapter 3

DECOMPOSE-QSM: Separate Diamagnetic and Paramagnetic Components based on Gradient-echo MRI Data

3.1 Introduction

Previously in Chapter 2, we introduced a non-invasive magnetic susceptibility measurement using MRI phase contrast, namely quantitative susceptibility mapping(QSM). QSM, however, does not characterize the sub-voxel susceptibility distribution. With the limited resolution ($\sim$ 1 mm) of MRI, a mixture of paramagnetic and diamagnetic susceptibility sources (at molecular scales) may exist in one voxel. The frequency contribution from the opposing susceptibility components may cancel each other in part or in whole, resulting in the total QSM decreasing or appearing near zero. For instance, deep brain nuclei contain both paramagnetic iron and diamagnetic myelin [29, 52, 114]; fibrotic livers commonly contain both paramagnetic iron and diamagnetic collagens [4, 92, 122]; kidney inflammation and fibrosis contain both paramagnetic iron and diamagnetic collagens [131]; β-amyloid may colocalize with iron in AD brains [20, 36, 64]. Therefore, the ability to separate the opposing susceptibility sources at the sub-voxel level will provide a more specific quantification of the magnetic properties of tissue.

There have been a few attempts to separate the opposing susceptibility sources [62, 100]. Lee et al. used both R_2 and R_2^* measurements to obtain the estimation of R_2'. R_2' is considered to be linearly affected by absolute susceptibilities, while frequency shift is modeled as a linear composition of susceptibilities convolving with the magnetic dipole kernel. Additionally, MEDI regularization [81] was used to reduce artifacts. In Schweser et al.'s work, both R_2^* and bulk susceptibility χ are assumed to depend linearly on the concentration of iron, the concentration of myelin, and a constant term. The coefficients are pre-calculated

from postmortem study and magnetization transfer saturation (MTS) images. These models assume that voxel-average magnetic susceptibility is the linear summation of paramagnetic and diamagnetic susceptibility. However, the fundamental signal progression of a multi-echo gradient echo sequence (GRE) involves complex exponentials. While the linear approximation holds when the phase accumulation is small, in general, this is not the case as it has been shown that the phase evolves nonlinearly as a function of echo time in many brain regions [28, 110].

Hereby, we model the problem with three-pool complex exponentials and develop an algorithm to estimate the opposing susceptibility sources within a voxel using solely multi-echo GRE data. We refer to the method as DiamagnEtic COMponent and Paramagnetic cOmponent SEparation or DECOMPOSE-QSM.

3.2 Three-pool DECOMPOSE-QSM Signal Model

DECOMPOSE-QSM is based on a 3-pool signal model. Each voxel is considered to be composed of three distributed pools of magnetic sources: paramagnetic, diamagnetic, and magnetically "neutral" (with respect to the reference susceptibility of the imaging volume) components (Figure 3.1A). Paramagnetic and diamagnetic sources are modeled as spheres that produce dipole fields outside the spheres but contain uniform magnetization within. The GRE signal of each pool is characterized by a complex exponential with its magnitude following an exponential R_2^*-decay and its frequency shift proportional to its magnetic susceptibility after the magnetic field contribution from outside the voxel is deconvolved. For the neutral pool, the frequency shift is zero. The total GRE signal of the voxel is a weighted summation of these three pools.

The sub-voxel structure in Figure 3.1A illustrates the complex signals originating from multiple compartments. There are 3 components in such a voxel: the paramagnetic component with volume susceptibility χ_+ and transverse relaxation rate $R^*_{2,+}$, the diamagnetic component with volume susceptibility χ_- and transverse relaxation rate $R^*_{2,-}$, and the reference susceptibility medium with volume susceptibility $\chi_0 = 0$ and transverse relaxation rate $R^*_{2,0}$. The reference susceptibility is generally the mean susceptibility within the field of view dominated by water. As derived in Chapter 9.1, transverse relaxation rate is a linear function of corresponding susceptibility at the static dephasing regime [23, 133].

$$R^*_{2,+,-} = a\,|\chi_{+,-}| + R^*_{2,0} \tag{3.1}$$

where $a = \frac{2\pi}{9\sqrt{3}}\gamma B_0$ (details are in Chapter 9.1) that evaluated at 3T is 323.5 Hz/ppm. The intercept of the linear approximation of $R_2^*(\chi)$ corresponds to the transverse relaxation rate of the reference susceptibility medium $R^*_{2,0}$.

The susceptibility sources are initially modeled to be spherical. Later, we show that the specific geometry has little influence on the components' susceptibility we define. For the phase of each susceptibility source, as long as the majority of the dipole field is within the voxel, the total field perturbation of the voxel will predominantly come from the interiors of

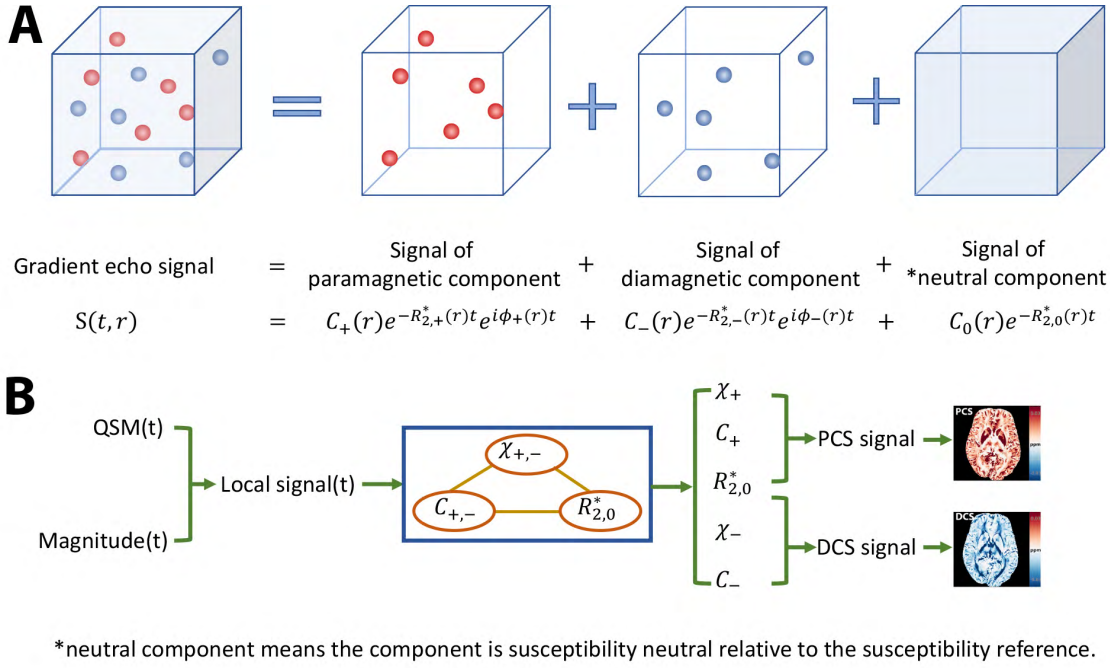

Figure 3.1: **A cartoon illustration of the signal model and the scheme of the solver.** (A)Signal of a voxel with a mixture of paramagnetic and diamagnetic sources can be decomposed into three pools of signal contributions. The signal outside the susceptibility sources has zero phases. (B) A flowchart of the proposed algorithm. The algorithm takes inputs of echo-time-dependent QSM and Magnitude to compose the local signal. The proposed alternating-direction solver processes the local signal and outputs the estimated unknowns. With the estimated parameters, maps of paramagnetic component susceptibility (PCS) and diamagnetic component susceptibility (DCS) are constructed respectively.

the spheres as the exterior fields cancel out due to the symmetrical dipole field distribution (Chapter 9.2). Thus, the field perturbation contributing from the inside of the sphere is then $B_{z,in} = \frac{2}{3}\chi B_0$, where χ is the volume susceptibility of the source and B_0 is the external static field strength.

Therefore, the total GRE signal $S(t)$ of the voxel with the three components can be written as

$$\begin{aligned} S\left(t; C_+, C_-, C_0, \chi_+, \chi_-, R^*_{2,0}\right) =& C_+ e^{-\left(a\chi_+ \,+\, R^*_{2,0} \,+\, i\frac{2}{3}\chi_+\gamma B_0\right)t} \\ &+ C_- e^{-\left(-a\chi_- \,+\, R^*_{2,0} \,+\, i\frac{2}{3}\chi_-\gamma B_0\right)t} \\ &+ C_0 e^{-R^*_{2,0}t} \end{aligned} \tag{3.2}$$

with C_+, C_-, C_0 indicating the concentrations of the corresponding components.

3.3 Solving for parameters of DECOMPOSE-QSM

3.3.1 Algorithm Design

To estimate the unknowns $(C_+, C_-, C_0, \chi_+, \chi_-, R^*_{2,0})$, we solve the following optimization problem,

$$\min_{C_+,C_-,C_0,\chi_+,\chi_-,R^*_{2,0}} f\left(S\left(C_+, C_-, C_0, \chi_+, \chi_-, R^*_{2,0}; t\right), y\left(t\right)\right) \tag{3.3}$$

where $y\left(t\right)$ is the measured multi-echo complex signal and $f\left(\cdot\right)$ is the objective function. We define $y\left(t\right)$ and $f\left(\cdot\right)$ as follows. The raw signal of a voxel contains phase contribution from sources outside the voxel while our signal model in Eq. 3.2 contains only sub-voxel contributions. To ensure that $y\left(t\right)$ is consistent with our model, rather than using the raw signal, we synthesize a local signal with magnitude $\mathrm{M}\left(t\right)$ as follows

$$y\left(t\right) = \mathrm{M}te^{-i\phi_{in}} = \mathrm{M}\left(t\right)e^{-i\frac{2}{3}\chi(t)\gamma B_0 t} \tag{3.4}$$

where $\mathrm{M}\left(t\right)$ is the magnitude of the raw signal. Note that the QSM of each echo, $\chi\left(t\right)$, is used instead of the average QSM across all echoes. The reason is that with the susceptibility sources being a mixture, the phase evolution is bound to be echo-time dependent [28, 109]. By using the QSM to synthesize the signal, we eliminate background phase contribution from outside the voxel.

The parameters to be estimated can be categorized into two classes: nonlinear parameters $(\chi_-, \chi_+, R^*_{2,0})$ and linear parameters (C_+, C_-, C_0). If only the linear parameters were to be estimated, the problem would have been perfectly convex, and a least square objective function would have sufficed. However, if the least square option is used as the objective function, the optimization will be largely dominated by the magnitude effect as tissue susceptibility induces a relatively small phase shift. On the other hand, if only nonlinear parameters were to be estimated, taking a logarithm of the modeled signal will linearize the model and ensure phase information weighs significantly in the objective function. The landscape in 3.2 shows the necessity of the logarithm modification and TE weighting for solving for $\chi_{+/-}$.

With these considerations, we divide the optimization problem of Eq. 3.3 into three sub-problems as follows,

$$\begin{aligned} &\min_{C_+,C_-,C_0} \|S\left(C_+, C_-, C_0; t, \chi_+, \chi_-, R^*_{2,0}\right) - y\left(t\right)\|_2 \\ &s.t.: \ C_+ + C_- + C_0 \ = \ 1 \\ &0 < C_{+,-,0} < 1 \end{aligned} \tag{3.5}$$

$$\begin{aligned} &\min_{R^*_{2,0}} \|\log\left(S\left(R^*_{2,0}; t, C_+, C_-, C_0, \ \chi_+, \chi_-\right)\right) - \log\left(yt\right)\|_2 \\ &s.t.: \ R^*_{2,0} > 0 \end{aligned} \tag{3.6}$$

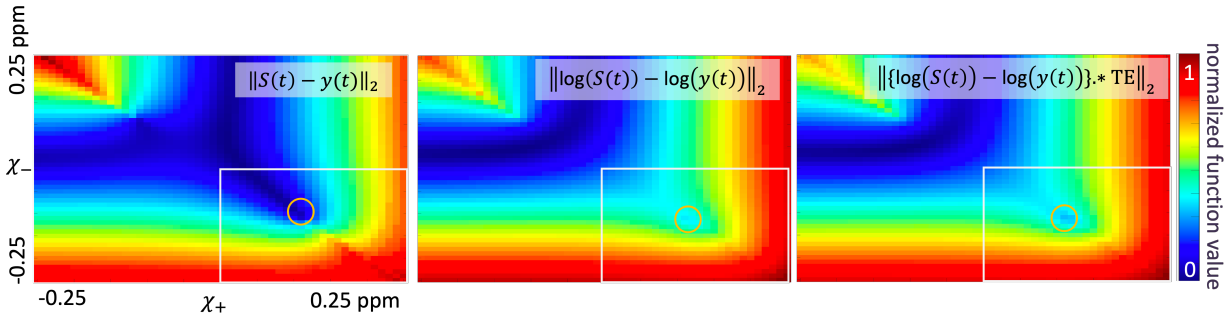

Figure 3.2: **Landscapes of different cost functions for the sub-problem of solving for $\chi_{+/-}$.** Signal and ground truth of one region of interest (ROI) from the phantom experiments(4) are used here for illustration. The white box indicates the feasible set, as χ_+ can only be positive and χ_- can only be negative. The orange circle indicates the region of the ground truth susceptibilities of the ROI with susceptibility mixture. Simple least square and does not give a good minimum cost for the ground truth. The log-modified cost function gives the minimum energy at the desired ground truth. With higher signal weighting of later TE, the desired ground truth shows a more significant local minimum within the feasible set.

$$\min_{\chi_+,\chi_-} \|\log\left(S\left(\chi_+,\chi_-,;t,C_+,C_-,C_0,R^*_{2,0}\right)\right) - \log\left(yt\right)\|_2$$
$$s.t.:\ 0.5 > |\chi_+|,|\chi_-| > 0 \tag{3.7}$$

The upper bound constraint of $|\chi_+|, |\chi_-|$ is roughly calculated using TE=25 ms and B_0=3T to ensure the phase does not exceed 2π. The estimation for $R^*_{2,0}$ has been singled out because this parameter is a linear parameter after taking the logarithm Eq. 3.6. The modification of taking the logarithm in Eq. 3.6 and Eq. 3.7 will not change the optimality since the logarithm is monotonically increasing for variables > 0. The logarithmic operation is not performed while solving for linear parameters (Eq. 3.5) to preserve the simplicity of the constrained linear program. We solve these three sub-problems in an alternating and iterative fashion (Figure 3.1B). With the computational cost in mind, we find that alternating 10 iterations among 3 steps is sufficient to achieve the optimality (Figure 3.3).

3.3.2 MATLAB Implementation

The algorithm and all the computing procedures are implemented in MATLAB 9.7 (The Math Works, Inc. MATLAB. Version 2019b) with Parallel Computing Toolbox and Optimization Toolbox. Particularly, Eq. 3.5 and Eq. 3.6 are solved by "interior-point" methods with "@lsqlin" function and Eq. 3.7 is solved through the "trust-region-reflective" method with "@lsqnonlin" using a manually calculated Jacobian sparse pattern to accelerate. The

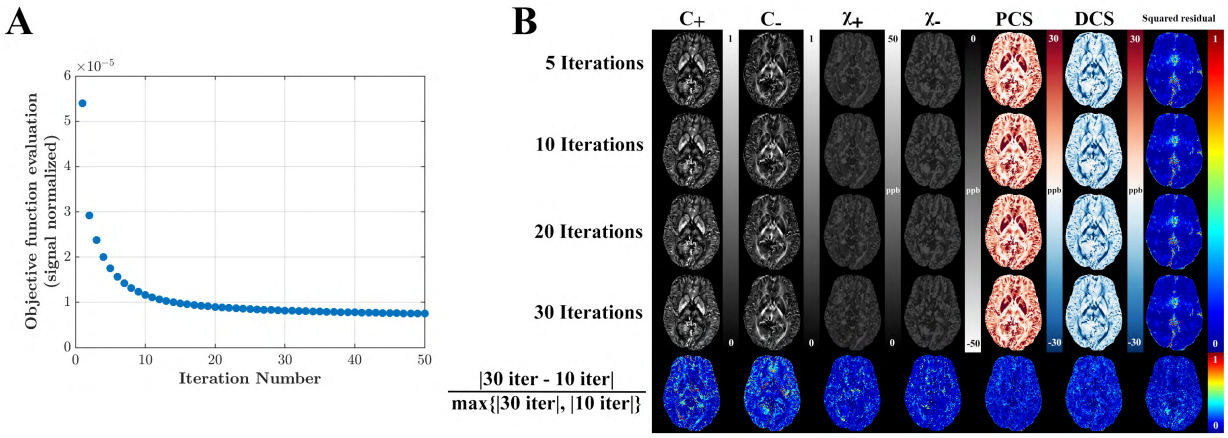

Figure 3.3: **Examination of the solver's convergence.** (A) Objective function value of a randomly chosen voxel normalized by signal intensity is dropping quickly within the first 10 iterations of alternating minimization. (B) Parameter maps and relative difference maps of *in vivo* experiments with 5, 10, 20, 30 iterations of alternating optimization procedure.

algorithm will be released under STI Suite (`https://people.eecs.berkeley.edu/~chunlei.liu/software.html`).

3.3.3 Paramagnetic Susceptibility Component (PCS) and Diamagnetic susceptibility Component (DCS)

The model yields six estimated parameters. While we can simply use $C_+\chi_+$ and $C_-\chi_-$ to quantify the sub-voxel paramagnetic susceptibility and diamagnetic susceptibility respectively, such an approach does not fully account for the complex tissue environment. Instead, we define a Paramagnetic Component Susceptibility (PCS) and a Diamagnetic Component Susceptibility (DCS) computed based on the signal model as follows,

$$\mathrm{PCS} = \frac{\sum_t \angle\left(C_+ e^{-\left(a\chi_+ + R^*_{2,0} + i\frac{2}{3}\chi_+\gamma B0\right)t} + \left(C_0 + C_-\right)e^{-R^*_{2,0}t}\right)}{\frac{2}{3}\gamma B_0 \sum t} \tag{3.8}$$

$$\mathrm{DCS} = \frac{\sum_t \angle\left(C_- e^{-\left(-a\chi_- + R^*_{2,0} + i\frac{2}{3}\chi_-\gamma B0\right)t} + \left(C_0 + C_+\right)e^{-R^*_{2,0}t}\right)}{\frac{2}{3}\gamma B_0 \sum t} \tag{3.9}$$

The PCS or DCS represents the situation of a voxel where only a paramagnetic or diamagnetic component exists along with a neutral medium. The quantity of each is nonlinear with respect to the bulk susceptibility.

Likewise, the composite susceptibility map is then defined as

$$\text{Composite susceptibility} = \frac{\sum_t \angle\left(\left(C_+ e^{-\left(a\chi_+ + i\frac{2}{3}\chi_+\gamma B0\right)t} + C_- e^{-\left(-a\chi_- + i\frac{2}{3}\chi_-\gamma B0\right)t} + C_0\right) e^{-R^*_{2,0}t}\right)}{\frac{2}{3}\gamma B_0 \sum t} \tag{3.10}$$

Since $\chi_\pm$ is defined as the volume susceptibilities of the sources, rather than bulk susceptibility, the herein-defined PCS or DCS can be viewed as the bulk susceptibility with only one susceptibility source and the reference susceptibility medium. PCS, DCS, and composite susceptibility are effective QSM and are comparable measures with conventional QSM. Later, we show that PCS and DCS can be reliably estimated and are less sensitive to the choice of "a" in Eq. 3.1.

3.4 Testing on *in vivo* brain MRI data

3.4.1 MRI Processing

Raw complex images of one healthy subject from a previous study [55] were used in this study. Imaging parameters for the multi-echo GRE sequence prescribed on the axial plane were as follows: TE1/spacing/TE16 = 2.7/2.9/46.2ms, TR = 59.3ms, B0 = 3T, bandwidth = 62.5 kHz, and a spatial resolution of $0.86 \times 0.86 \times 1.0\text{mm}^3$.

QSM reconstruction was performed with functions in STI Suite. The GRE magnitude images of the first echo were used to mask and extract the brain tissue using the brain extraction tool (BET) in FSL[108]. The raw phase was unwrapped using a Laplacian-based phase unwrapping method [67, 98]. The background phase was removed with the V-SHARP method[70, 130]. Lastly, STAR-QSM [123] was performed to compute the susceptibility maps for each echo. For the *in vivo* scans, susceptibility values were referenced to the mean susceptibility of the whole brain as it has previously been shown that no obvious systematic bias is observed between analysis with and without reference to CSF [69]. For the *ex vivo* scans, due to the lack of a common reference for QSM across the temperatures, the resulting *ex vivo* temperature-dependent QSM maps are re-referenced to the region where R_2^* value has lower than 2 Hz standard deviation over time.

3.4.2 Results

Figure 3.4 shows a representative case of the DECOMPOSE being applied to a healthy subject's brain. Additional illustrations of another healthy subject are shown in Figure 3.5. The calculation time of one axial slice is ∼250 seconds on a MacBook Pro with 2.8 GHz Intel core i7 processor and with 16 GB memory. For 16 echoes of the signal, parameter estimation converges at the majority region of brain tissue with a squared residual of less than 0.1. The fitted complex signals for four representative voxels illustrate the general goodness of fitting (Figure 3.6). The PCS and DCS show a good agreement with the known

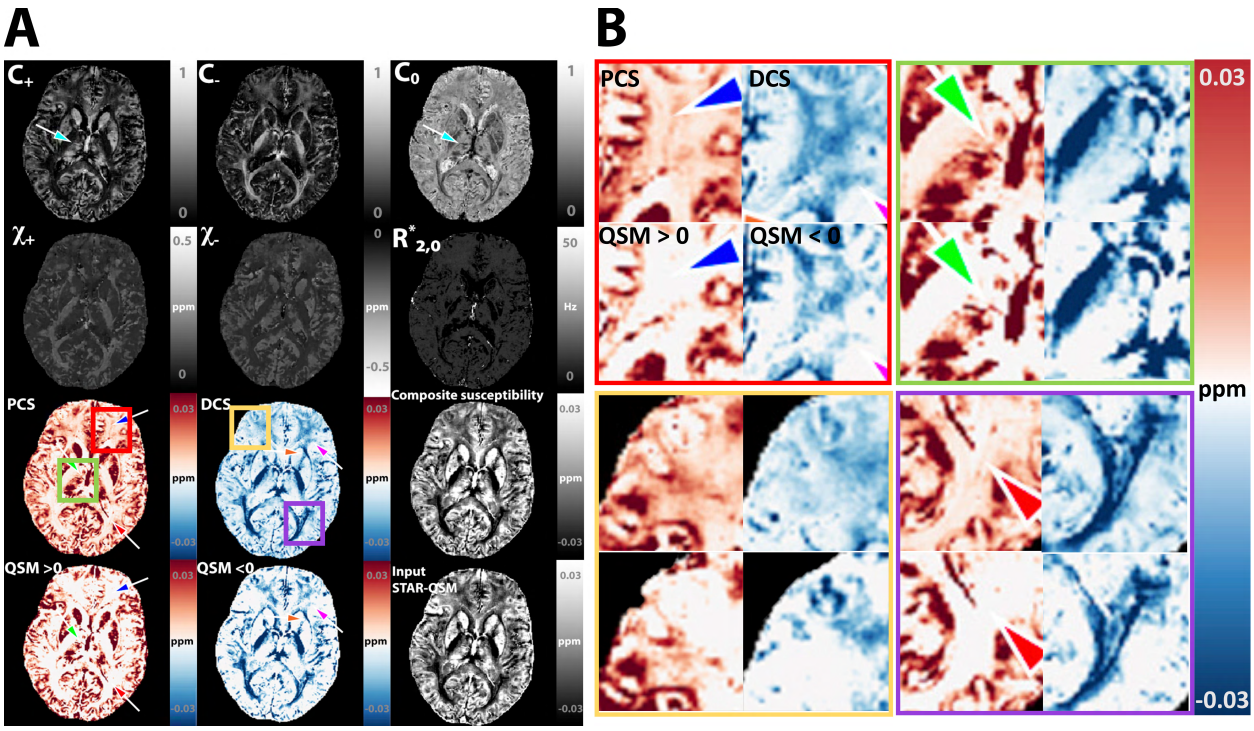

Figure 3.4: **DECOMPOSE-QSM of a healthy adult study participant.** (A) Individual parameter maps of DECOMPOSE results. First row: signal fraction maps show a high fraction of paramagnetic susceptibility in gray matter, a high fraction of diamagnetic susceptibility in white matter, and a high fraction of neutral component in the ventricles. The C0 map particularly reveals a clear delineation of the thalamic subnuclei (arrow). Third and fourth row: The paramagnetic component susceptibility (PCS) and diamagnetic component susceptibility (DCS) show the existence of a sub-voxel mixture of paramagnetic and diamagnetic components in both gray and white matter (arrows), which is not revealed in threshold QSM. The composite susceptibility is comparable to the input STAR-QSM. The subplots relate to the χ_- and DCS are displayed with inverted dynamic range to have better visual contrast. (B) zoom-in view of four regions

distribution of paramagnetic and diamagnetic species in the human cerebral region (Figure 3.4 and 3.5). The DCS shows more complete white matter regions than simply taking a threshold of QSM. The C_0 map showed the highest values at the atrium of the lateral ventricles and the anterior horns of the ventricles. These high values of C_0 correspond to the high concentration of cerebrospinal fluid (CSF) which has high free water fraction and low susceptibility in those regions. Interestingly, the C_+, C_-, C_0 map reveals distinctive structural boundaries between subfields of the thalamus, reflecting a variation of free water concentration among the various brain structures. The composite susceptibility shows a minimal difference from the input QSM. This confirms that DECOMPOSE-QSM preserves the total volume susceptibility value.

Further, we compare DECOMPOSE results at frontal cortex regions with the histology data reported in [114]. As shown in Figure 3.7, compared to the threshold QSM, PCS reveals the iron content in cortical white matter and the DCS map matches the pattern of the myelin content, visually more consistent with histology.

3.5 Conclusion

The proposed DECOMPOSE-QSM algorithm utilizes both the phase and magnitude information to separate susceptibility components within a voxel. The model consists of three pools of susceptibility sources that are spatially distributed: zero susceptibility (reference susceptibility), diamagnetic and paramagnetic susceptibility. We engineered a novel cost function and developed an effective optimization routine to solve the challenging nonlinear inverse problem. DECOMPOSE-QSM provides six parameters and composite susceptibility maps (PCS and DCS) to characterize the susceptibility compartments. More experiments are needed to further validate the method and individual maps with independent measures and test its applications.

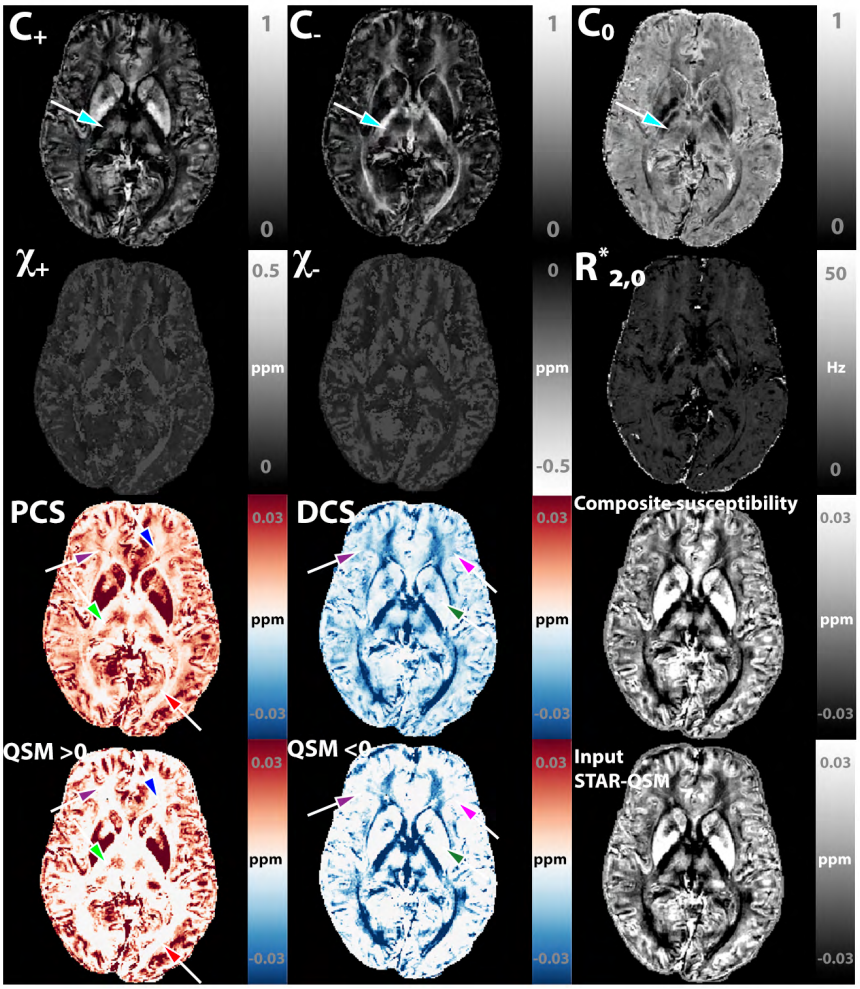

Figure 3.5: **An additional illustration of DECOMPOSE-QSM being applied to a healthy adult study participant.** Similar to Figure 3.4, the first row: signal fraction maps show a high fraction of paramagnetic susceptibility in gray matter, a high fraction of diamagnetic susceptibility in white matter, and a high fraction of neutral component in the ventricles. The C0 map particularly reveals a clear delineation of the subthalamic nuclei (arrow). Third and fourth row: The paramagnetic component susceptibility (PCS) and diamagnetic component susceptibility (DCS) show the existence of a sub-voxel mixture of paramagnetic and diamagnetic components in both gray and white matter (arrows), which is not revealed in threshold QSM. The composite susceptibility is comparable to the input STAR-QSM. The subplots relate to the χ_- and DCS are displayed with inverted dynamic range to have better visual contrast.

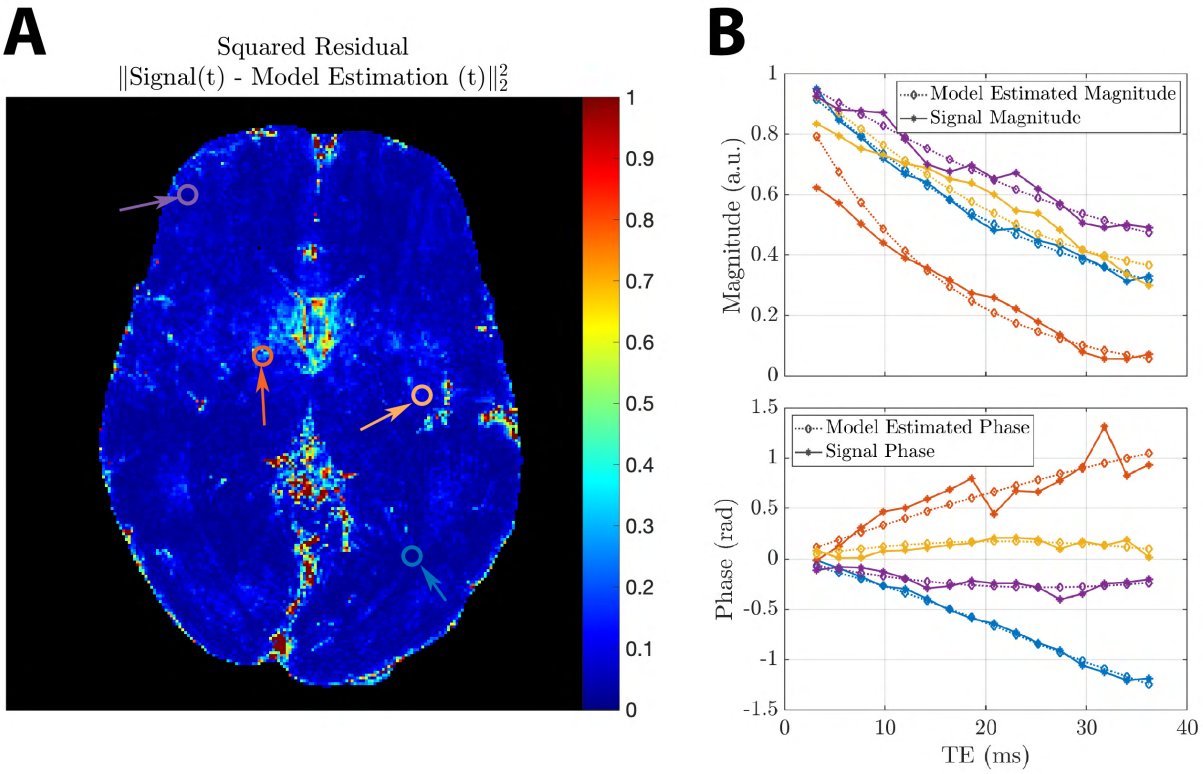

Figure 3.6: **Model fitting performance for an *in vivo* case.** (A) Squared residual errors of a representative *in vivo* brain slice resulting from DECOMPOSE model fitting. (B) Magnitude and phase of four representative voxels in the illustrative brain slices. Solid curves are the input signal, dotted curves are the fitted curves.

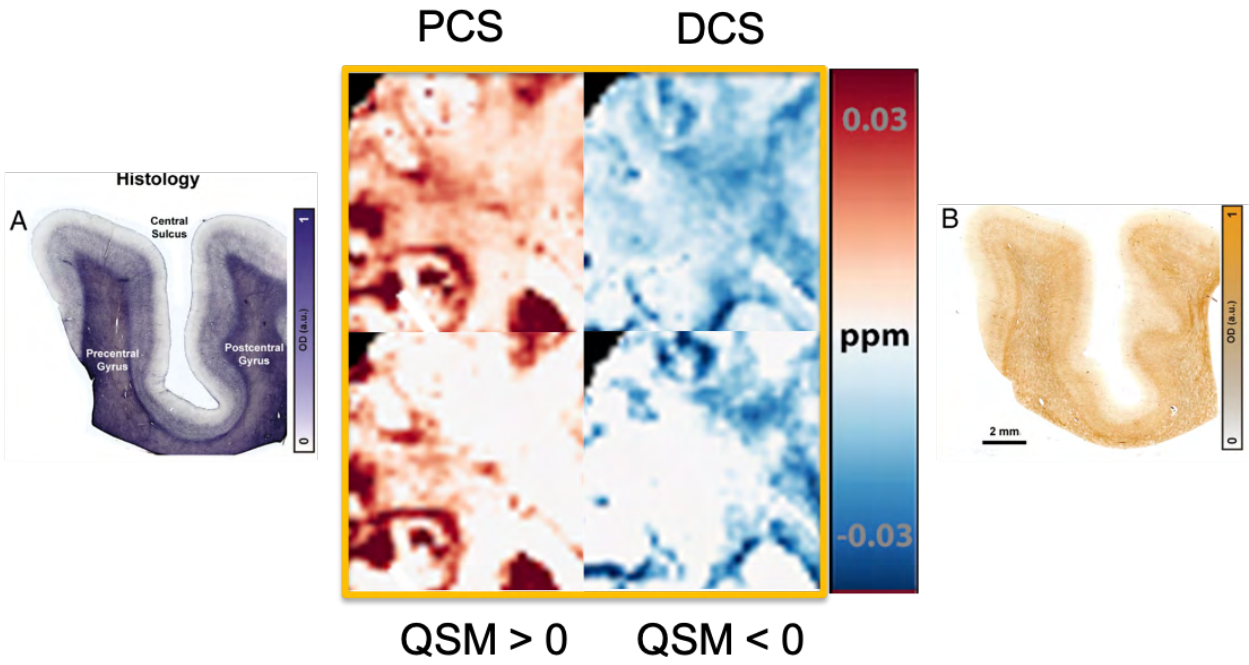

Figure 3.7: **Visual comparison of previously reported histology and DECOMPOSE results.** Photos A and B are histological staining of iron and myelin from Stüber et al.[114] respectively. The middle plot is the zoomed-in view of a cortical region of PCS and DCS (top) vs. threshold QSM (bottom). PCS matches the pattern of iron staining while DCS matches the myelin staining visually.

Chapter 4

Validating DECOMPOSE-QSM

4.1 Introduction

In the previous Chapter, the model of DECOMPOSE-QSM was introduced to resolve the sub-voxel magnetic susceptibility mixture situation. A MATLAB implementation has shown the model's potential of separating paramagnetic and diamagnetic susceptibilities. In this chapter, we validate the DECOMPOSE-QSM model and MATLAB solver using numerical forward field simulations, phantom experiments, and *ex vivo* temperature-dependent MRI scans.

4.2 Validation Experiments Methods

4.2.1 Numerical Simulation

The analytical forward field simulation was performed for 100 voxels independently with each of them consisting of 128^3 sub-voxels with TE1/spacing/TE16 = 2.5/2.5/40 ms, TR = 42ms, B0 = 3T. Simulations are running with MATLAB 9.7 (The Math Works, Inc. MATLAB. Version 2019b) on an Ubuntu 18.04.5 64-bit platform and 48 CPUs of Intel(R) Xeon(R) Silver 4116 CPU with 2.10 GHz, 512 GB memory. For each simulation (i.e., each of the 100 voxels), spheres with varying radius and pre-assigned susceptibility ($\chi = 0.01 \sim 0.15$ ppm) representing either diamagnetic or paramagnetic component are generated randomly within this 128^3 cubic (Figure 4.1A). The radius of these spheres was forced to be greater than 6 sub-voxels to reduce the numerical error of digitizing a sphere. Histology study of common pathological plaques with iron and protein aggregation are around the size of tens to hundreds of microns [2, 83, 117](; the randomized choices of susceptibility source's radius are to imitate such sub-voxel situations. Then a B0 field aligning with the z direction of the voxel is applied. Induced forward field perturbation was calculated in an analytical fashion for each sub-voxel using the superposition rule of the fields produced by the spheres. The GRE signal of each sub-voxel is generated by a single component exponential function with

its magnitude being an exponential decay ($R_2^* = 20$ Hz) and its phase is proportional to the corresponding field perturbation at that sub-voxel. The signals from each of the 128^3 sub-voxels are summed together assuming equal proton density to form the total complex signal of the simulated voxel.

4.2.2 Gel Phantom

Agarose (Fisher Scientific) was mixed with water at 1% w./w. (with T_2 is approximately 60 ms according to [136]) to achieve a typical T_2 of biological tissue. The agarose water mixture was heated up with a microwave oven until it is forming a homogeneous clear liquid. The agarose gel solution is poured into a 1L cylindrical Nalgene jar (112 mm diameter and 151 mm height) made from Polypropylene with seven cylindric placeholders. After the agarose solution solidified, 20 mL holes (17.5 mm diameter) were made with a smooth surface so that signal gaps and air bubbles can be avoided. These holes are then filled with agarose gel mixed with different concentrations of susceptibility sources to form direct contact with the outer embedding agarose gel. We use $CaCO_3$ (Sigma-Aldrich) as the diamagnetic species and Fe_2O_3 (Sigma-Aldrich) as the paramagnetic species. Two calibration phantoms were fabricated with gradient concentrations of Fe_2O_3 (or $CaCO_3$) to achieve estimated susceptibility ranging from $0 \sim 0.15$ ppm (or -0.1$\sim$ 0 ppm for $CaCO_3$) to mimic typical biologic tissue volume susceptibilities. One susceptibility mixture phantom was made to validate the proposed model and algorithm. The mixture ratio of each cylinder is indicated in Figure 4.2K The detailed parameters are listed in the supporting table (Table 4.14.2)

The phantoms were scanned on a GE MR750w 3T scanner (GE Healthcare, Milwaukee, WI, USA). Each phantom was placed in the scanner with its long cylindrical axis aligned with the B0 field of the scanner and was scanned axially with a three-dimensional multi-echo gradient echo (GRE) sequence of the following scan parameters: TE1/spacing/TE16 = 1.47/1.63/25.9 ms, TR = 30.1ms, bandwidth = 62.5kHz, matrix size = $192 \times 192 \times 128$, and a native spatial resolution of $1.0 \times 1.0 \times 1.0\text{mm}^3$. QSM is calculated using the same pipeline as described in 3.4.1.

4.2.3 Temperature Dependency of Paramagnetism

Following Curie's Law, over a certain range of temperature and field strength, paramagnetic susceptibility is approximately inversely proportional to temperature,

$$\chi\left(T \to \infty\right) = \frac{C}{T}\ , \tag{4.1}$$

where C is the material's specific Curie constant. We use this relationship to validate the resulting PCS. Specifically, the PCS is expected to be temperature dependent as paramagnetic susceptibility in brain tissue is predominately caused by iron while the DCS should remain stable as temperature changes. Such an effect is visible through QSM according to a previous study [16].

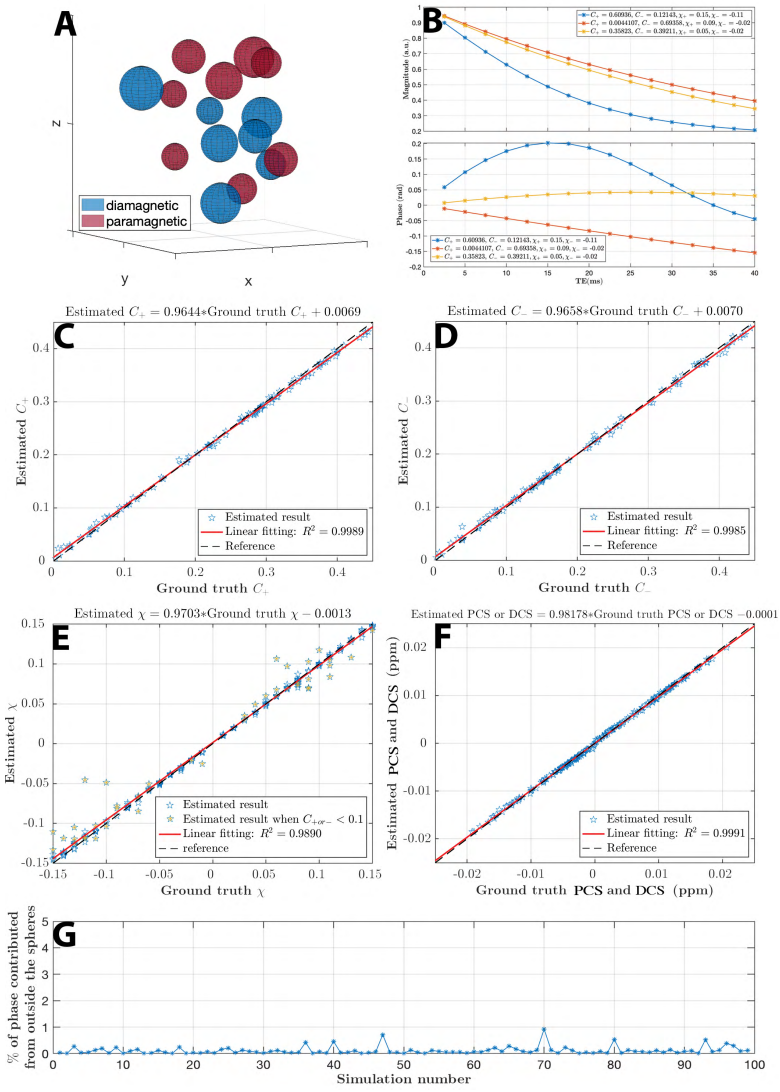

Figure 4.1: **Numerical simulation.** (A) Spheres assigned either positive or negative susceptibility with various radii are drawn randomly in a voxel space. (B) Illustration of magnitude and phase signal progression for 3 simulated voxels with different combinations of assigned parameters.(C E) Estimated parameters versus the ground truth are shown respectively. (E) The simulation results mostly are in good agreement with ground truths. Results of χ that deviate the most from the ground truth are the cases when the concentration is low ($C_{+or-} < 0.1$). (F) The composite paramagnetic component susceptibility (PCS) and diamagnetic component susceptibility (DCS) show good agreement with the ground truth. (G) The magnetic field perturbation outside the spheres has a negligible contribution to the total phase of the voxel as shown over 100 random simulations, which confirms the validity of the voxel field approximation.

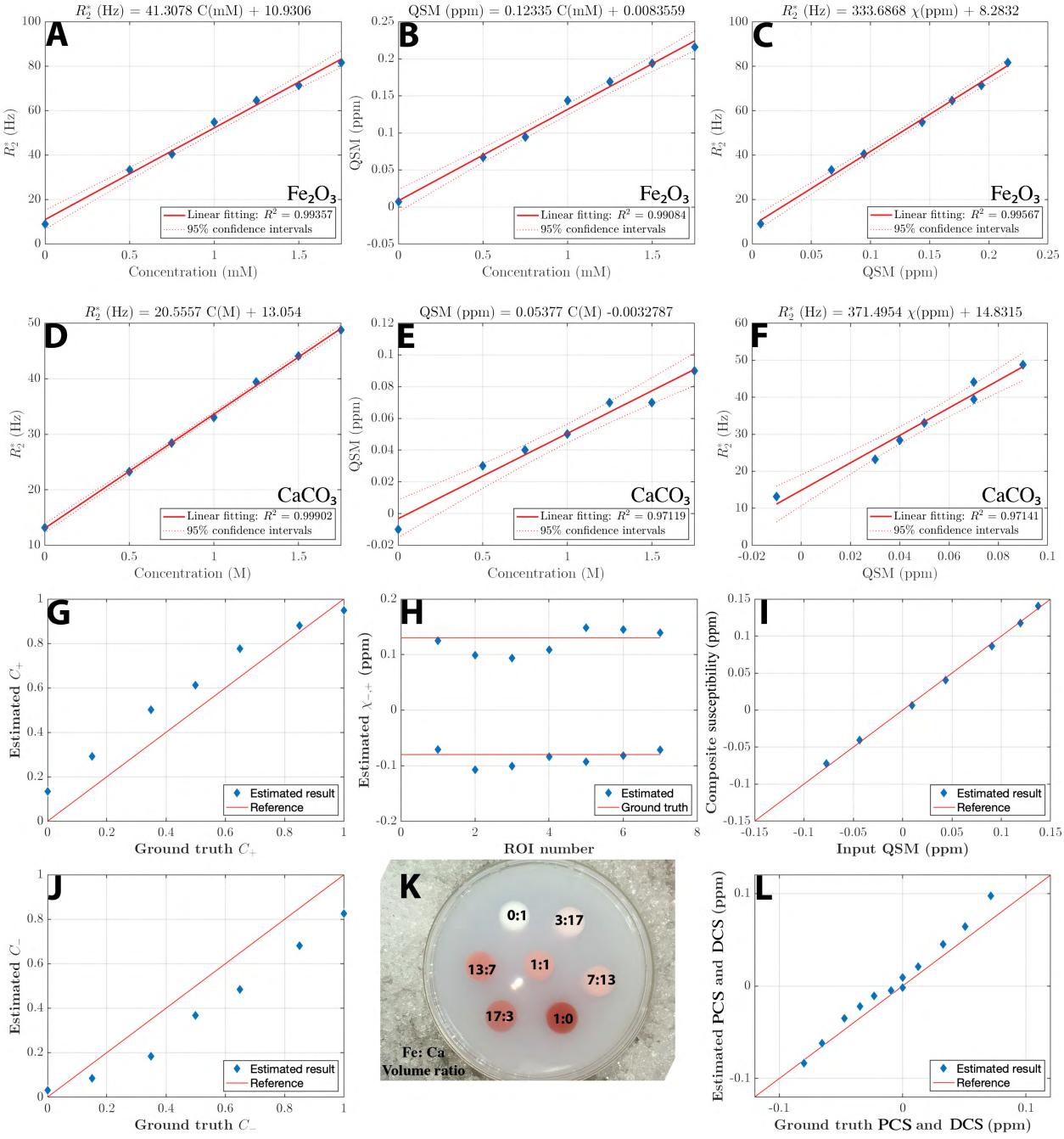

Figure 4.2: **Phantom experiments.** (A,B,D,E) Linear regression of R_2^* and QSM versus concentrations of each species from each calibration phantom. (C F) Linear regression of R_2^* versus QSM for each calibration phantom. The linear slopes match the derivation from static regime theory.

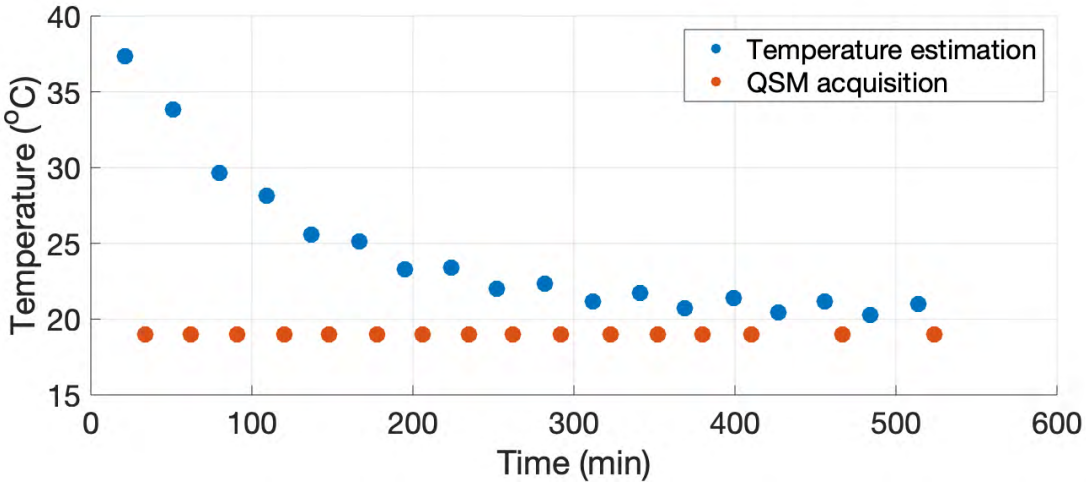

Figure 4.3: **Temperature variant experiment setup.** Temperature profile estimated from water proton spectrum before each QSM scan. The blue circle is the estimated temperature from calculating the chemical shift. The orange circles indicate the times of each QSM acquisition.

Two human brainstems were fixed in non-buffered 4% formalin for over 12 months, individually, washed out in distilled water, and placed into a proton-free fluid called Fomblin (a chemically inert perfluoropolyether fluorocarbon) prior to MRI scanning. Fomblin produces no MRI signal and has a similar magnetic susceptibility to tissue [103]. The sample tube was heated up using a hot water bath for 3 hours at 40°C just before the MRI scans. MRI acquisition was performed using a 7T Magnetom (SIEMENS, Erlangen, Germany) with a gradient amplitude of 70mT/m and a slew rate of 200 T/m/s, using an in-house built solenoid coil with 28 mm of inner diameter, 34 mm outer diameter, and 130 mm length. Just before placing the sample into the scanner, the temperature was measured using a digital infrared thermometer.

QSM acquisition was repeated within 11 hours, while the brainstem was allowed to cool down naturally until reaching thermal equilibrium at room temperature (20°C). One sample was scanned with five echoes of TE1/deltaTE/TE5 = 4/3/16 ms, TR = 32 ms, and the other with 16 echoes of TE1/deltaTE/TE16 = 4/3/49 ms, TR = 64 ms. The acquisition time for each QSM sequence was 17 min 20 sec and 11 min 33 sec, respectively. For the 16-echo acquisition, due to the low SNR of images at later echoes, only the first 12 echoes were adopted for further analysis.

Just before every new GRE sequence, a single-shot water-unsuppressed spectrum was acquired, using a semiLASER sequence [31, 96, 107], with TE/TM/TR=7/26/9000ms. The size of the voxel was $30\times20\times20\text{mm}^3$ including most of the brainstem. The acquired spectrum allowed for the measurement of water chemical shift as a function of time, which was used

to calibrate sample temperature (Figure 4.3). For the 16-echo data, due to a sequence error, the spectrum information was not properly saved. The initial temperature before placing the brainstem into the scanner was recorded to be 36°C and the end temperature was 21°C. Figure 4.4 and 4.5 were drawn assuming the temperature change during natural cool down is similar to that in the 5-echo data. QSM is calculated using the same pipeline as described in 3.4.1.

4.3 Validation Experiments Results

4.3.1 Numerical Simulation

The analytical forward simulation is performed to justify the assumed model as well as to measure the ability of the proposed solver for the noiseless case. The forward field and signal simulation requires ∼4 hours per voxel. With 24 CPUs of parallel computing, simulating 100 voxels can be completed in two days. Simulation shows that the magnitude profile of the mixture model remains largely exponential as a function of TE, while the phase develops a nonlinear TE dependency (Figure 4.1B), consistent with previous reports of TE-dependent QSM in the brain [28, 109]. These results demonstrate that 1) it is necessary to use TE-dependent QSM as the input, and 2) phase information needs to play a significant role in the objective function to alleviate the difficulty of separating the summation of exponentials.

Parameter estimation results versus ground truths are shown in Figure 4.1C-F. In general, estimations for linear parameters (C_+, C_-, C_0) show less deviation from ground truths than those of the nonlinear parameters (χ_+, χ_-). Nevertheless, the composite paramagnetic component susceptibility (PCS) and diamagnetic component susceptibility (DCS) agree with the ground truth. The forward field simulation also confirms that the assumption of "total field perturbation contributed from the outside sphere is nearly zero" is valid (Figure 4.1G).

4.3.2 Gel Phantom

Figure 4.6 illustrates the maps of each estimated parameter and the composite maps. The halo-looking artifact is the streaking artifact viewed in the axial slice from QSM inversion. The inversion algorithm, STAR-QSM, is optimized for *in vivo* susceptibility calculation, where the susceptibility map of bio-tissue should not have sharp edges. The existence of such artifacts is due to the sharp transition of susceptibility at the boundary of ROIs. The C_0 map successfully captured the region where the material is purely agarose gel without any susceptibility species (referenced to water). The PCS and DCS maps verify that DECOMPOSE-QSM is able to reveal the mixing situation of each cylinder while threshold QSM can not reveal such information. This is especially striking in cylinders where the paramagnetic and diamagnetic components' contributions cancel out leading to nearly zero value in the original QSM. The two calibration phantoms showed high linearity of R_2^* vs QSM (Figure 4.2A-F). The linear slope of $R^*_{2,+,-} \sim \chi_{+,-}$ is estimated to be 334 Hz/ppm for the

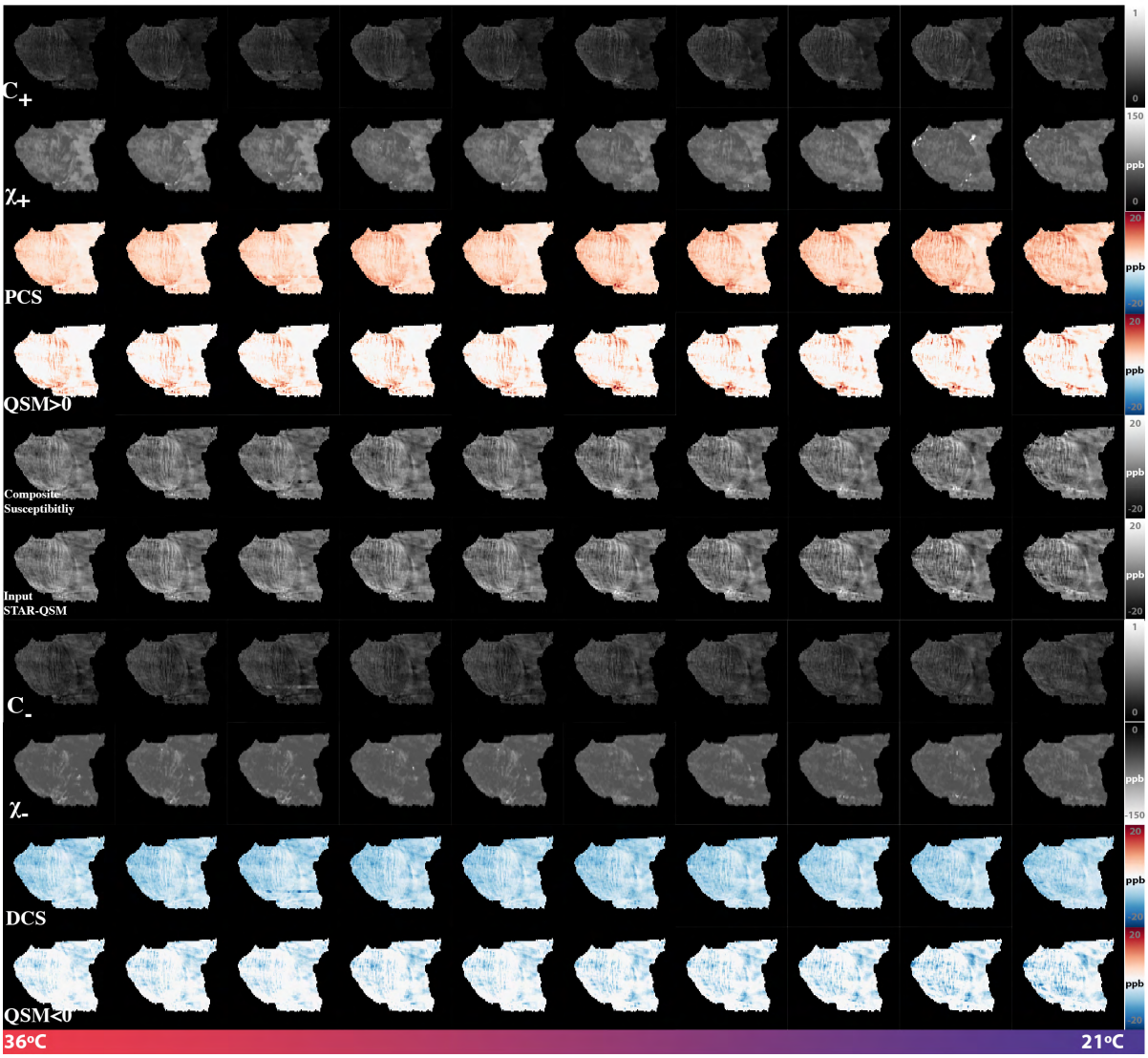

Figure 4.4: **DECOMPOSE-QSM parameter maps of a brain stem specimen as a function of temperature.** The increasing trend of PCS is visible, while the temperature-related change in DCS is minimal. The subplots relate to χ_- and DCS are displayed with an inverted dynamic range to have better visual contrast.

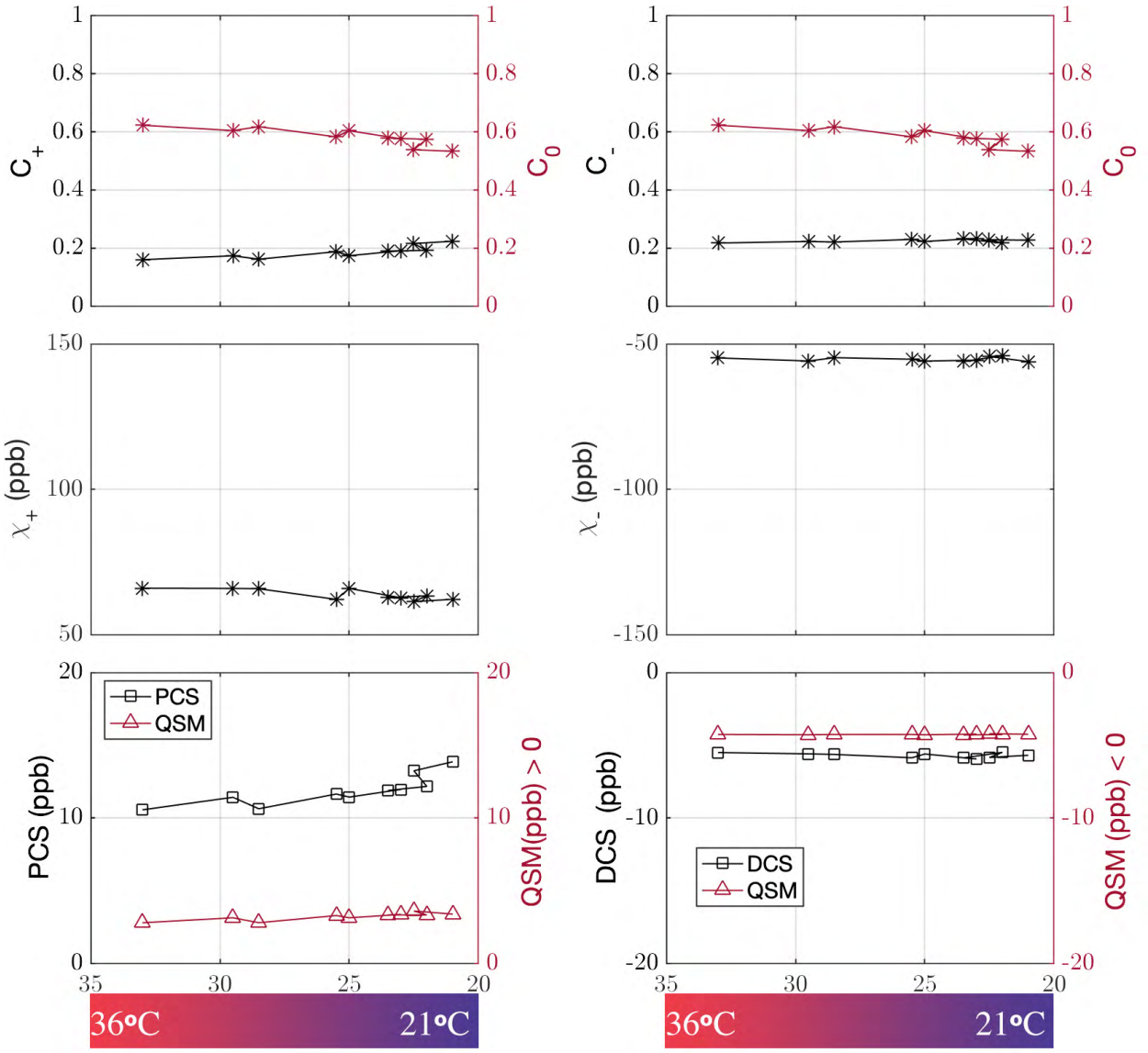

Figure 4.5: **DECOMPOSE-QSM results of another brain stem specimen as a function of temperature.** GRE data were acquired with twelve echoes. Temperatures range from 36 °C to 21 °C . The mean value is calculated from the non-zero mean of one representative slice. Note the paramagnetic component susceptibility is increasing with decreasing temperature as expected.

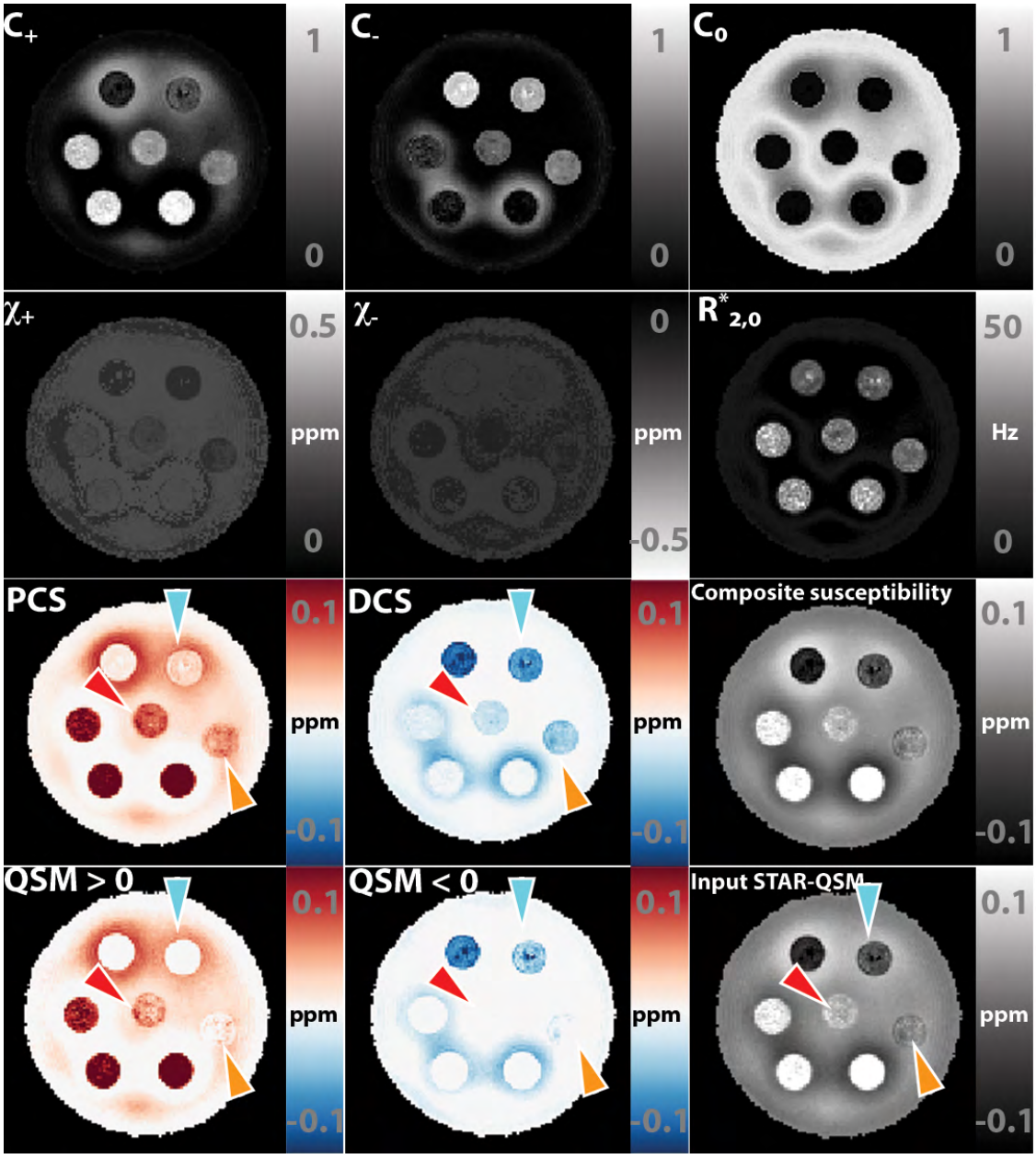

Figure 4.6: **DECOMPOSE-QSM results of a susceptibility-mixture phantom showing the parameters and composite susceptibility maps in comparison with thresholding original QSM.** Note that the subplots that relate to the diamagnetic component are displayed with an inverted dynamic range to have better visual contrast. The composition of each tube is shown in Figure 4.2K. Arrows point at the regions of interest that show visually significant improvement in the contrast of the mixture.

	Calibration Phantom 1			Calibration Phantom 2		
ROI	Fe_2O_3 Concentration(mM)	Volume (mL) of 2 mM Fe_2O_3 (per 20 mL)	Measured susceptibility (ppm)	$CaCO_3$ Concentration(M)	Mass (g) of $CaCO_3$ (per 20 mL)	Measured susceptibility (ppm)
1	0	0	0.002±0.006	0	0	-0.004±0.002
2	0.5	5	0.059±0.017	0.5	1.002	-0.032±0.011
3	0.75	7.5	0.089±0.016	0.75	1.502	-0.040±0.006
4	1	10	0.140±0.016	1	2.002	-0.055±0.019
5	1.25	12.5	0.162±0.018	1.25	2.502	-0.069±0.017
6	1.5	15	0.186±0.028	1.5	3.003	-0.073±0.018
7	1.75	17.5	0.209±0.031	1.75	3.503	-0.094±0.011

Table 4.1: **Composition of calibration phantoms.** The volume of each cylindrical ROI is 20 mL. Fe_2O_3 agarose solution for each ROI is prepared from diluting 2 mM concentrated Fe_2O_3 agarose solution with 1% agarose solution. $CaCO_3$ agarose solution for each ROI is prepared directly by the weight of $CaCO_3$ powder. The susceptibility is measured from STAR-QSM reconstruction. Two calibration phantoms were made to calibrate for the measurable ground truth volume susceptibility.

Fe_2O_3 phantom and 371 Hz/ppm for the $CaCO_3$ phantom. These values agree with the theoretical calculation of 323.5 Hz/ppm. As shown in Figure 4.2G-L, the DECOMPOSE-QSM calculation is able to separate the paramagnetic and diamagnetic components. Despite some inaccuracy, the estimated C_+, C_-, χ_+, χ_- values largely lie close to the reference red solid line that indicates where a perfect estimation would fall onto. On the other hand, the paramagnetic component susceptibility (PCS) and diamagnetic component susceptibility (DCS) estimations are highly accurate. The composite susceptibilities align with the input mean QSM (Figure 4.2I,). Detailed numbers are included in Table 4.1 and 4.2.

A Previous study has investigated the potential phase temporal artifact caused by Laplacian-based unwrapping and filtering [28]. To validate that the nonlinear phase evolution we observed is not a confounding result from Laplacian-based phase unwrapping [70, 130]), temporal-based phase unwrapping [80] was performed for each echo (Figure 4.7). Temporal unwrapping retained significant spatial phase wraps when the field inhomogeneity is too large for the echo spacing of this acquisition (ΔTE = 1.63 ms) or when SNR is low (Figure 4.7). Despite that, it is shown that at the earlier echoes, at regions when temporal-based phase unwrapping is successful, the nonlinearity of the phase progression was still observed and was similar to that of Laplacian-based unwrapping.

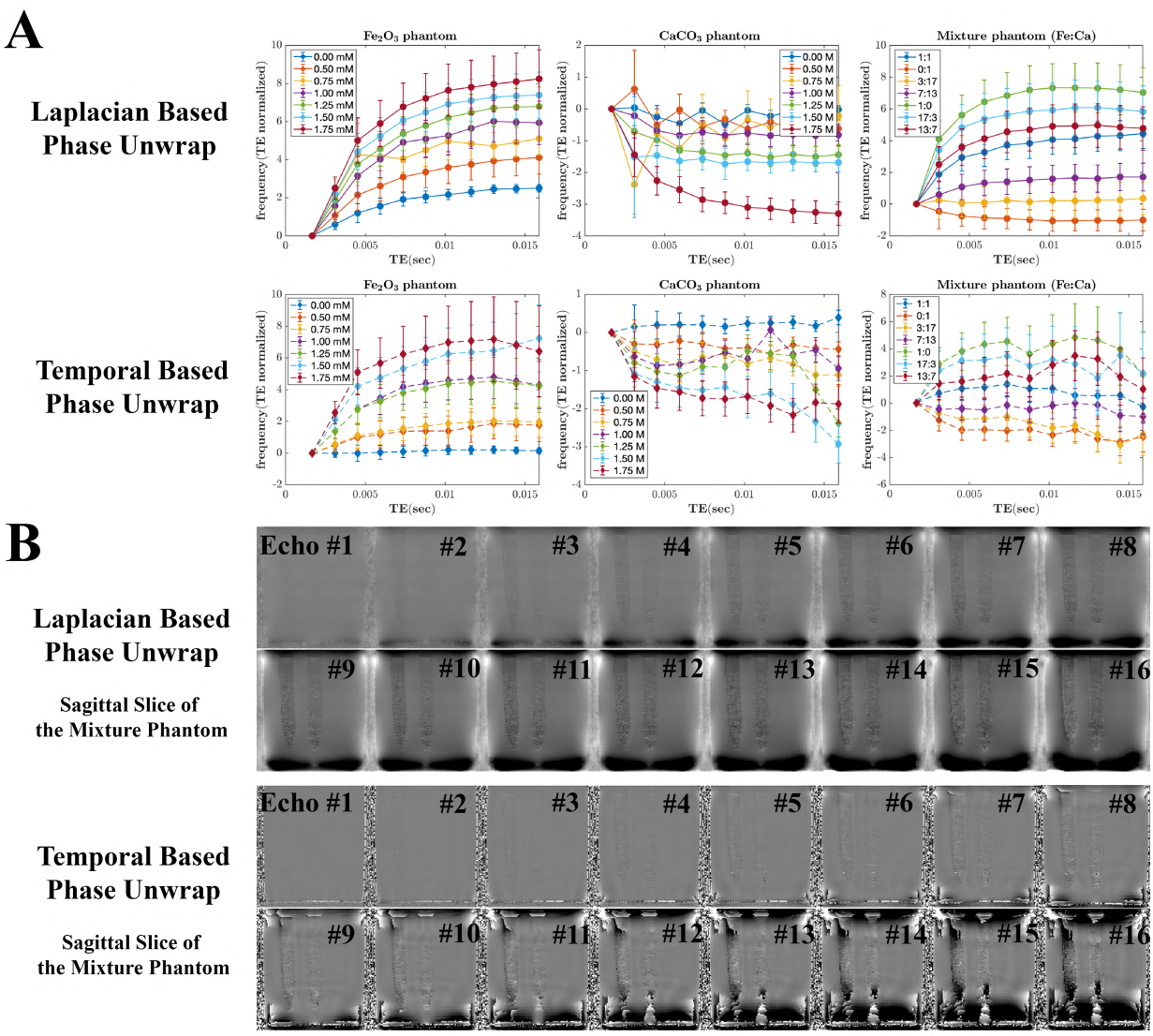

Figure 4.7: **Comparison of unwrapped phase based on Laplacian (V-SHARP) method and temporal unwrapping method.** (A) unwrapped phases relative to the first echo of each phantom over an ROI are plotted against the echo time from the first up to the eleventh echo. Echoes after the eleventh echo are discarded due to unreliable temporal-based phase unwrapping. (B) Unwrapped phase maps of one representative sagittal slice of the mixture phantom at each echo. Temporal-based unwrapping fails when field inhomogeneity is too large or when SNR is too low.

	Mixture Phantom					
ROI	Ratio of Fe_2O_3	Ratio of $CaCO_3$	Volume (mL) of 1.0 mM Fe_2O_3	Volume (mL) of 1.5 M $CaCO_3$	Measured susceptibility (ppm)	Predicted susceptibility (ppm)
1	0.5	0.5	10 mL	10 mL	0.044±0.013	0.034
2	0	1	0 mL	20 mL	-0.074±0.014	-0.073
3	0.15	0.85	3 mL	17 mL	-0.046±0.022	-0.041
4	0.35	0.65	7 mL	13 mL	0.008±0.012	-0.001
5	1	0	20 mL	0 mL	0.146±0.021	0.140
6	0.85	0.15	17 mL	3 mL	0.121±0.023	0.108
7	0.65	0.35	13 mL	7 mL	0.086±0.018	0.006

Table 4.2: **Composition of susceptibility mixture phantoms.** The volume of each cylinder ROI is 20 mL. 1.0 mM Fe_2O_3 agarose solution and 1.5 M $CaCO_3$ agarose solution are prepared and then mixed with different ratio. The susceptibility is measured from STAR-QSM reconstruction. The predicted susceptibilities are based on calibration phantom results.

4.3.3 Temperature Dependency of Paramagnetism

DECOMPOSE-QSM was also validated using the fact that paramagnetic susceptibility is temperature dependent. The temperature of the brainstem was estimated using water proton chemical shift (Figure 4.3). The DECOMPOSE results of each set of data are presented as line graphs and corresponding parameter maps. Detailed parameter maps of one sagittal slice of each specimen are shown in Figure 4.8 and Figure 4.4. The resulting PCS showed more visible increases than threshold QSM maps as the temperature decreases before reaching the thermal equilibrium of room temperature. The DCS showed minimal changes across the scans. With both 5 and 12 echoes, the increases in the resulting PCS are visually noticeable (the increase of red color from left to right in the row of PCS) in the maps as the temperature decreases. This trend is also shown as line plots in Figure 4.9 and 4.5. It appears that the 12-echo data result in more stable DCS maps across the temperatures. We further estimated the Curie constant for the brainstem tissue by linear fitting of PCS with the reciprocal of temperature (Figure 4.10). The Curie constant is estimated to be 21.84 ppm K with the 5-echo data. If the temperature change during natural cool down is similar for both experiments, we estimated the Curie constant from data with 12 echoes to be 19.26 ppm K. Curie constant of brain tissue was previously estimated at around 2 ppm emu K/g/Oe [16], which is 25 ppm K if the density of brain tissue is approximate 1 g/cm^3. Our estimation is therefore comparable with the reported value of brain tissue.

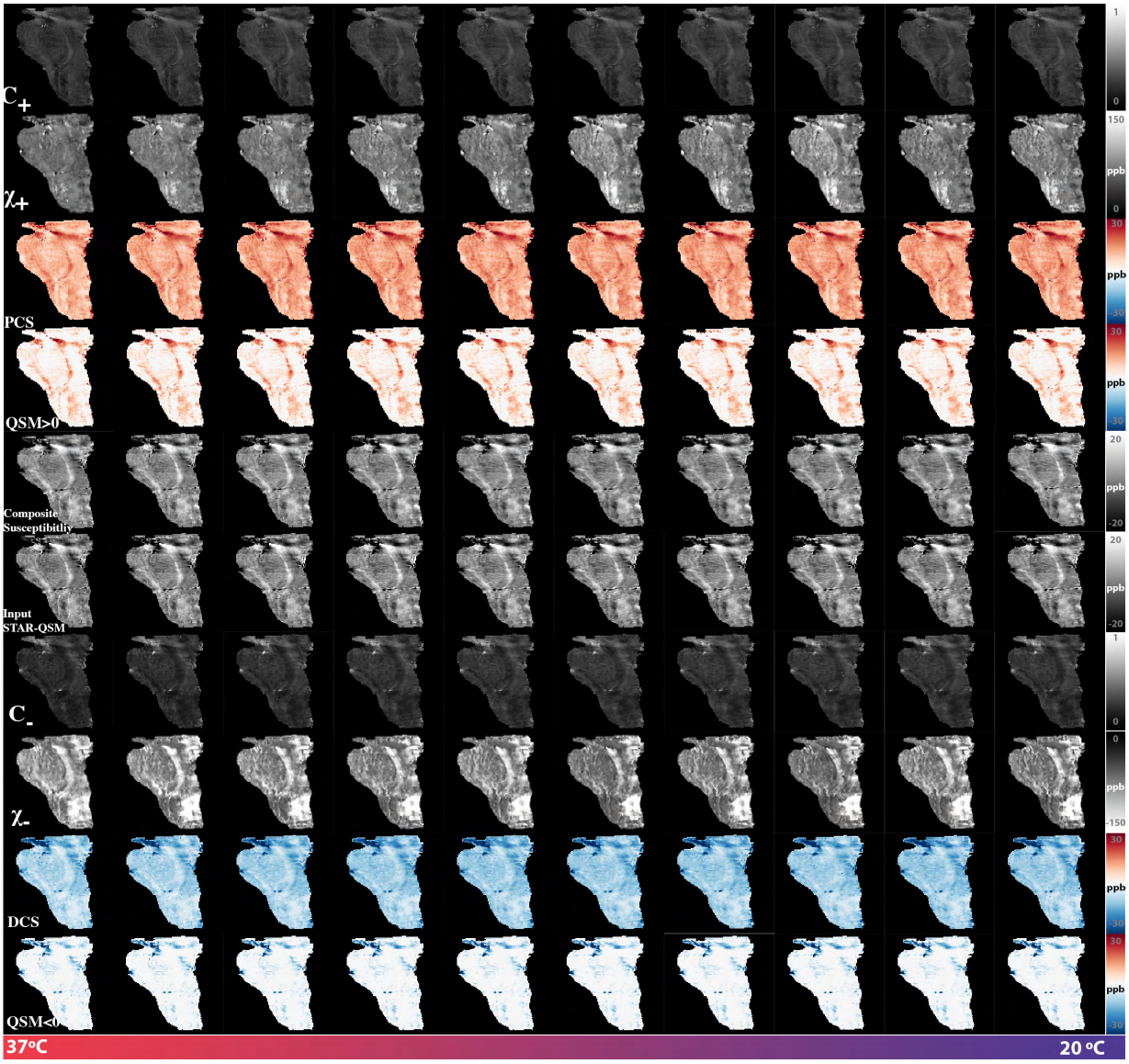

Figure 4.8: **DECOMPOSE-QSM parameter maps of a brain stem specimen as a function of temperature.** While DCS maps remain mostly stable, PCS maps show an increasing trend, especially for the first five scans where the temperature was changing the most drastically. The subplots relating to χ_- and DCS are displayed with an inverted dynamic range to have better visual contrast.

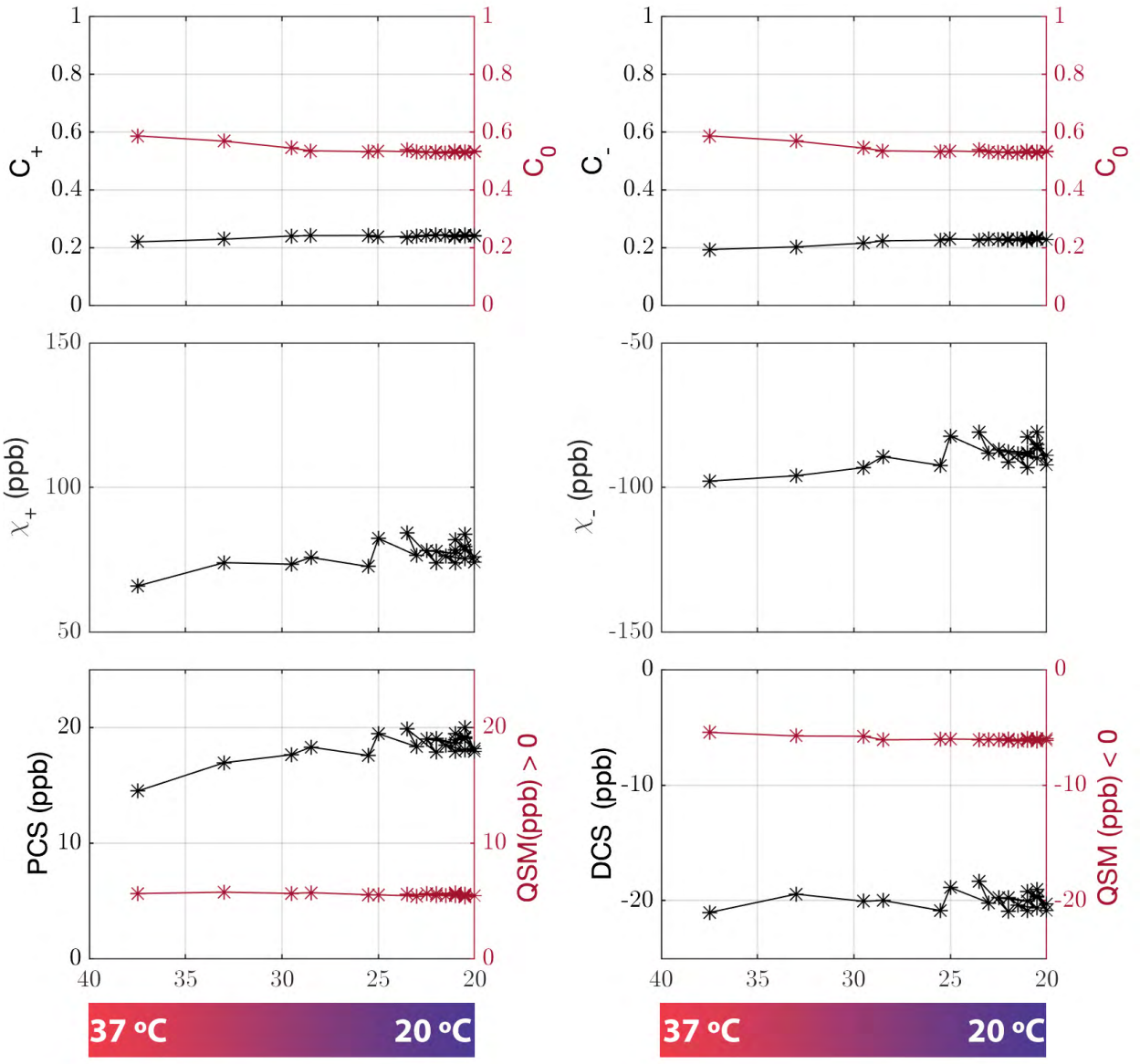

Figure 4.9: **DECOMPOSE-QSM results of a brain stem specimen as a function of temperature.** GRE data were acquired with five echoes. Temperature ranges from 37 °C to 20 °C. The mean value of each parameter of a representative slice is displayed vs. temperature changes. The paramagnetic component susceptibility (PCS) shows an increasing trend that's more prominent than the corresponding threshold QSM.

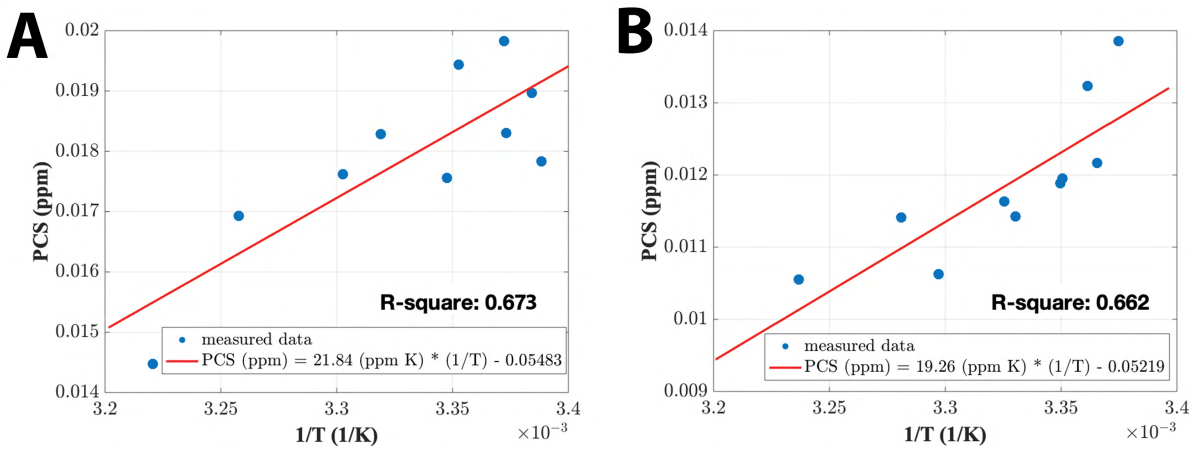

Figure 4.10: **Curie Constant.** Linear correlations of paramagnetic component susceptibility with the inverse of temperature from data with five-echo data (A) and twelve echoes (B). Each error bar is the standard deviation of PCS of the same sagittal slice of each temperature acquisition.

4.4 Discussion

4.4.1 The estimations of $C_+, C_-, C_0, \chi_+, \chi_-, R^*_{2,0}$

In general, the estimations of C_+, C_-, C_0 show a high accuracy (in the numerical simulation, Figure 2) and yield reasonable concentration maps (Figures 4.64.83.44.43.5). Particularly, the C_0 map in the phantom experiment (Figure 3) well captures the pure gel portion of the susceptibility mixture phantom. The C_0 map reveals a high reference medium concentration in the ventricle CSF (nearly 1 in value); it also shows anatomical meaningful subfields of the thalamus and putamen region (Figure 3.43.5 These results suggest that a high C_0 map may indicate a low level of cell density or high free water concentration. Further studies are needed to compare these results from similar parameters estimated with other MRI methods, such as diffusion-based NODDI [45, 134, 138].

The estimations of χ_+ and χ_- are similarly highly accurate when $C_{+\ or\ -} > 0.1$, however, the accuracy decreases when C_+ or C_- has relatively small values ($C_{+\ or\ -} < 0.1$) (Figure 4.1) For example, in the internal capsule (Figure 3.43.5), C_+ has a relatively lower value, and χ_+ is unexpectedly higher than that of the global pallidus region. Although one may speculate that this difference suggests a different paramagnetic molecular species in the internal capsule that is more paramagnetic than that of the global pallidus, it is more likely that this difference is an estimation inaccuracy. Another example can be found in the parameter maps of the phantom experiments (Figure 4.6). In the cylinders with high iron concentration, χ_+ is estimated accurately; while in cylinders with low iron concentrations, χ_+ is underestimated compared to the true value. Similar cases occur in the χ_- maps.

This inaccuracy can be explained as follows. When the concentration level, C, is low, a slight alternation in the value of χ will not lead to a significant change in the objective function evaluation due to the multiplicative relationship. The solver captures the nonlinear signal progression to estimate parameters rather than the linear superposition of positive and negative species. However, at low concentrations, the nonlinearity is less significant. Therefore, the inaccuracy of nonlinear parameters appears.

The above reasoning also explains that despite the slight inaccuracy of nonlinear parameters' estimations, the composite susceptibility maps, PCS and DCS are still highly accurate to reveal the sub-voxel susceptibility mixing situation (Figure 4.1F). PCS and DCS are considered to be effective QSM. For example, PCS is the estimated bulk susceptibility as if the negative susceptibility sources within the voxel are replaced with the reference susceptibility medium. While one can always use each of the estimated parameters for further analysis (Figure 4.11), obtaining accurate values of χ is fundamentally challenged due to the high nonlinearity of Eq. 3.2. On the other hand, the effective QSM, PCS, and DCS are not only insensitive to the estimation error of χ but also provide comparable values with QSM.

In our model, the $R^*_{2,0}$ parameter is the apparent transverse relaxation rate of the reference susceptibility component. $R^*_{2,0}$ includes contributions from R2 and R'_2 as the protons experience in the background medium (i.e., the "reference susceptibility" source). Both diamagnetic and paramagnetic susceptibility sources contribute to the R'_2 decay of the medium even though their phase contributions average to be zero within the medium (Figure 4.1G). Further, calcium and iron also affect water R2 [42, 97, 118].

4.4.2 Choices of echo times

The DECOMPOSE method is based on multi-echo 3D GRE data. Generally, the more echoes are available, the more beneficial it is to the algorithm as the model relies on the temporal behavior of the signal progression. Here we show that, in practice, with as few as five echoes, the algorithm is still able to separate paramagnetic and diamagnetic susceptibility. In general, the echo times should be well-spaced for a good balance between SNR and sufficient phase variation accumulation. While short TE offers better SNR, it captures very limited phase variation. On the other hand, at longer TE, the SNR is too poor to provide a useful signal. The range of TE should generally cover the corresponding T2* of the tissue [129](Wu et al., 2012).

4.4.3 Linear coefficient a of R^*_2 and single source susceptibility χ

The parameter a in the proposed DECOMPOSE method is the linear coefficient between R^*_2 and a single-source volume susceptibility χ. The theoretically calculated linear coefficient a is 107.8 Hz/ppm/T in the static dephasing regime. The linear slope of $R^*_{2,+,-} \sim \chi_{+,-}$ is estimated to be 334 Hz/ppm for the Fe_2O_3 phantom and 371 Hz/ppm for the $CaCO_3$ phantom (Figure 4.2 both are consistent with the theoretical value of 323.5 Hz/ppm at the static dephasing regime. However, this parameter a shall not be confused with the regression

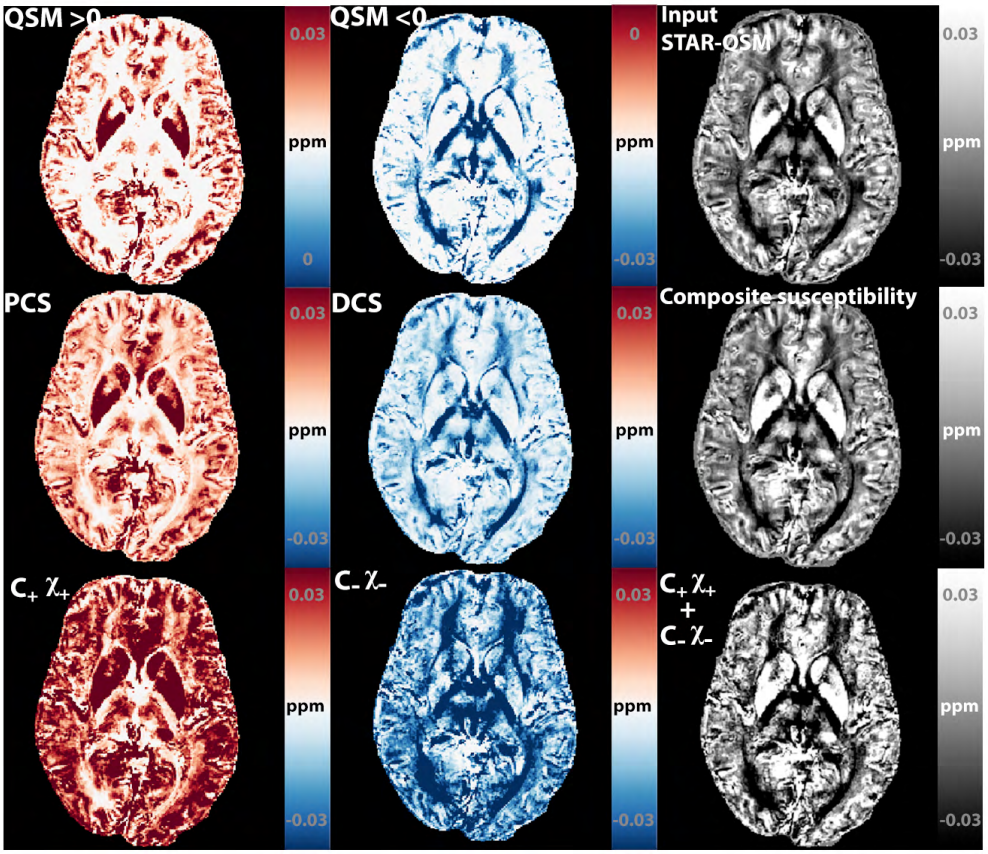

Figure 4.11: **DECOMPOSE-QSM result representations.** Different DECOMPOSE-QSM result representations are shown in row 2 and row 3 compared to threshold QSM results in row 1. Paramagnetic component susceptibility (PCS) is calculated using estimated paramagnetic component-related parameters (C_+, χ_+) and estimated parameters related to neutral component $(C_0, R^*_{2,0})$ according to equation Eq. 3.8. Diamagnetic component susceptibility (DCS) and composite susceptibility are calculated likewise according to equations Eq. 3.9 and Eq. 3.10. Plots in the last row are direct multiplications of concentration C_+(or C_-) and χ_+(or χ_-) and the superposition of both components' direct multiplications. The direct multiplication of each component reflects the true susceptibility without the neutral component being considered hence the brighter appearance.

coefficient between R_2^* and volume QSM where the voxel contains a mixture of various susceptibility sources or when the static dephasing regime no longer holds. For example, even though the static dephasing regime assumption still holds as in the calibration phantoms, in the mixture phantom, the linear coefficient between R_2^* and QSM values is only 117.9 Hz/ppm (Figure 5.1, significantly smaller than the theoretic value of 334 Hz/ppm, because the voxel contains a mixture of both Fe_2O_3 and $CaCO_3$. Further, in brain tissues *in vivo*, because the effect of water diffusion can longer be neglected, the static dephasing regime no longer holds. Combining the motion narrowing effect which reduces R_2^* [18] and the mixture of susceptibility sources in the brain, the coefficient between R_2^* vs QSM is expected to deviate from the static dephasing theory. For example, a previous study has reported the R_2^* vs QSM fitting result of 366 Hz/ppm at 7T [34] and 126.7 Hz/pp at 3T [69] both deviate from the static-dephasing-regime theoretic value of 754.8 Hz/pm and 323.5 Hz/ppm respectively.

As to the susceptibility source's geometry influence on the linear coefficient of $R_2^* v.s. \chi$, the value of 323.5 Hz/ppm is obtained for spherical susceptibility sources. At another extreme case, if parallel cylindrical susceptibility sources are considered, the coefficient becomes $a_{\parallel} = \frac{1}{2}\gamma B_0 sin^2\theta$, where θ is the angle between parallel cylinders' long axes and B_0 field direction [133]. The maximum value of the coefficient is then 401.3 Hz/ppm at 3T. Being spherical and cylindrical are two extreme geometries of susceptibility sources. The linear coefficient of other geometries should be in between these two extreme values. More generally, the effective parameter a can be written as $a_{eff} = a_{angle\ independent} + a_{angle\ dependent}(\theta)$ with the orientation correction term accounting for geometric effect and susceptibility anisotropy. According to orientation-dependent T2* studies [63, 89], the maximum variation of the R_2^* relaxation rate between $0 \sim \pi$ rotating angles is 8Hz in the corpus callosum region at 7T. The susceptibility magnitude of white matter lipid is larger than 0.1 ppm [71, 82, 125], therefore, the maximum angle correction to the parameter a is less than 80 Hz/ppm, or 12 Hz/ppm/T. As shown in Figure 4.12, within the range of $a = 323.5 \sim 401.3$ Hz/ppm, the resultant composite maps (PCS and DCS) are insensitive to different combinations of the linear coefficients a_+, and a_-. Numerically, the different combinations of coefficient result in a standard deviation of 0.7 ppb for PCS maps and 1.1 ppb for DCS maps which are negligibly small. Alternatively, one may adjust the parameter a for each voxel to account for the underlying geometries, however, this will either require prior knowledge or increase the number of unknowns. The current model and solver use solely multi-echo gradient echo data as conventional QSM scans.

As discussed in Section 4.4.1, even with a perfect choice of a, the estimation of χ can be erroneous sometimes when the concentration is below 0.1. This effect is due to the difficulty of fitting for highly nonlinear parameters that lack unique solutions. It is therefore more advantageous to use the effective QSM, PCS, and DCS, as they are robust against the estimation error of χ and the parameter choices of a.

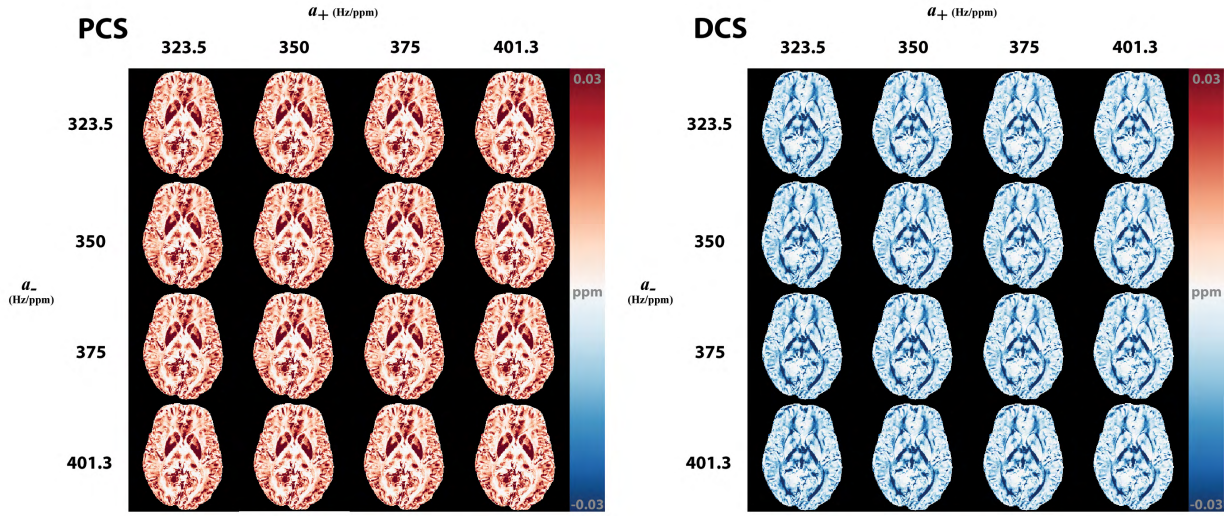

Figure 4.12: **DECOMPOSE-QSM performed with different combinations of choices of coefficient of linear relaxation relation with susceptibility.** The linear coefficient depends on the shape of the susceptibility source. If the susceptibility source is considered to be spherical, the coefficient is estimated to be 323.5 Hz/ppm, whereas if the susceptibility source is considered to be parallel cylinders, the maximum value of the coefficient is 401.3 Hz/ppm. The true susceptibility source situation should be in between these two extremes. The illustration shows that within the range, the standard deviation of the resulting PCS and DCS is 0.7 ppb and 1.1 ppb respectively; both are negligibly small compared to experimental precision.

4.5 Conclusion

QSM is an increasingly used MRI technique for quantifying tissue magnetic susceptibility. However, biological tissues are generally complex and MRI resolution is limited. As a result, QSM does not characterize the sub-voxel distribution of magnetic susceptibility. Here, we propose and develop DECOMPOSE-QSM to separate the diamagnetic and paramagnetic susceptibility components within a voxel. The method is theorized based on GRE signal behaviors in compartmentalized tissue microstructures and validated with numerical simulation, phantom experiments, *ex vivo* and *in vivo* brain imaging experiments.

Chapter 5

Clinical Application of DECOMPOSE-QSM

So far, a complete framework of DECOMPOSE-QSM has been introduced, validated, and tested. In this chapter, we explore the benefit of DECOMPOSE-QSM being used in clinical settings.

5.1 Parkinson's Disease Biomarker

Parkinson's disease (PD) is a neurodegenerative disorder that affects the dopamine-producing neurons in the brain. As these neurons degenerate, it can lead to a decrease in dopamine levels, causing symptoms such as tremors, rigidity, and difficulty with movement. Studies have shown that patients with Parkinson's disease have higher levels of iron in the substantia nigra compared to healthy individuals[46, 11]. This increased iron content has been suggested to play a role in the neurodegeneration seen in Parkinson's disease, as iron can cause oxidative stress and damage to cells.

QSM has been shown to be a useful tool in the diagnosis and monitoring of Parkinson's disease[54, 48, 47, 61, 1]. Here we show that separating the magnetic susceptibility sources can increase the sensitivity of detecting the iron overload and potentially detect demyelination in PD cases.

Raw complex images of ten PD patients and ten healthy subjects from a previous study [55] were used here. Imaging parameters for the multi-echo GRE sequence prescribed on the axial plane were as follows: TE1/spacing/TE16 = 2.7/2.9/46.2 ms, TR = 59.3ms, bandwidth = 62.5 kHz and a spatial resolution of $0.86 \times 0.86 \times 1.0\text{mm}^3$. QSM is calculated using the same pipeline as described in Chapter 3.4.1.

One-tailed two-sample t-test shows that DECOMPOSE-QSM can detect known susceptibility differences between PD patients and healthy controls in various brain regions. Nuclei in basal ganglia and substantia nigra are known to be involved in PD progression [35, 88]. Iron alternations in regions of caudate nucleus (CN), red nucleus (RN), substantia nigra (SN),

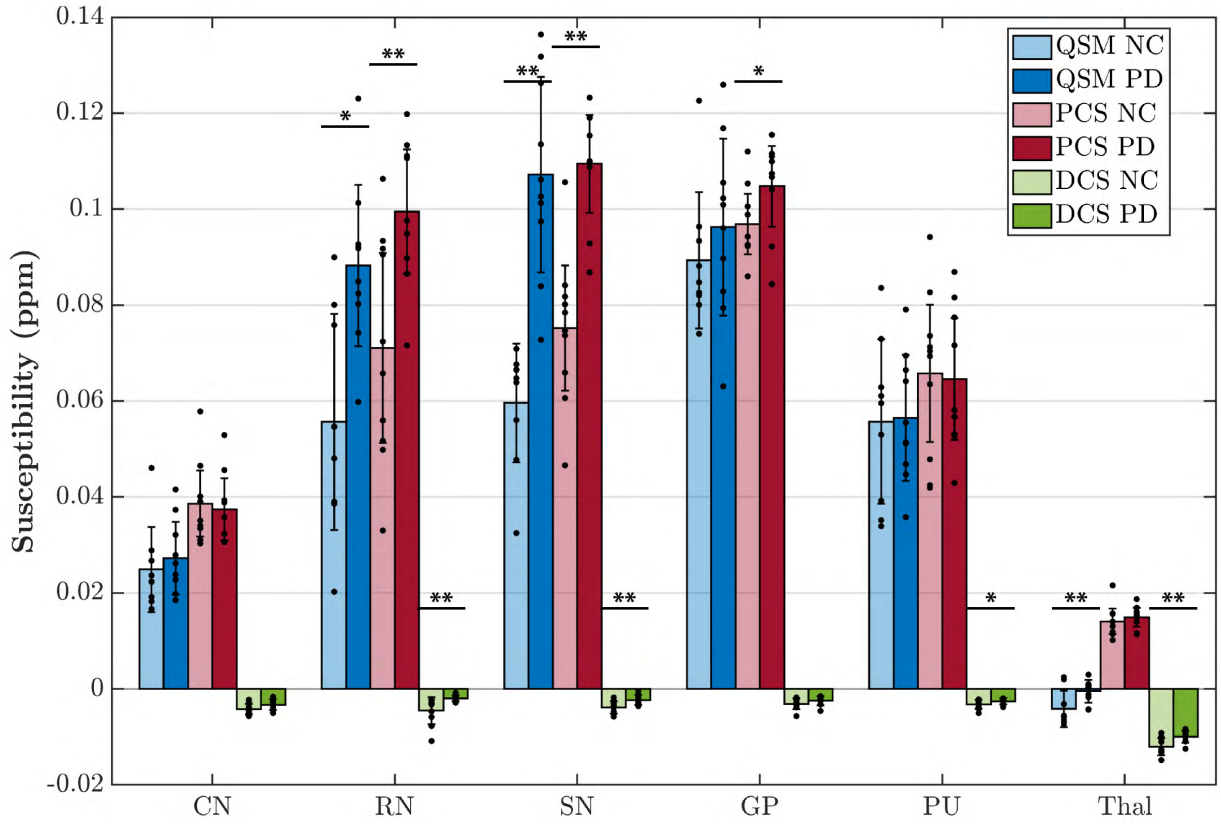

Figure 5.1: **Region-of-interest (ROI) analysis of PD patients vs. controls (n = 10)** for QSM, paramagnetic component susceptibility (PCS), and diamagnetic component susceptibility (DCS). Susceptibility values of each contrast and each ROI are shown as bars with standard deviation presented as error bar. Data points of each ROI from each subject are shown as black dots overlayed on the bar graph. Symbols of "*" indicate significant difference: $*p < 0.05$, $**p < 0.01$. CN: caudate nucleus; RN: red nucleus; SN: substantia nigra; GP: global pallidus; PU: putamen; Thal: thalamus.

global pallidus (GP), putamen (PU), and Thalamus (Thal) are often being investigated to improve the understanding of PD pathology [9, 48, 55, 61]. The regions with statistically significant differences between PD patients and controls in QSM also show a significant difference in PCS (or DCS for thalamus, Figure 5.1 In the thalamus region, the mean QSM of the region has a negative value. After decomposing, the DCS showed significant a difference, but PCS did not. Interestingly, the DCS of RN, SN, and PU also showed significant differences. The detailed values are displayed in Table 5.1.

Maps	Regions	Normal Controls	PD patients	p-value
QSM	CN	0.022(0.012)	0.023((0.014)	0.48
	RN	0.056(0.023)	0.080(0.033)	0.033*
	SN	0.060(0.012)	0.097(0.040)	0.005**
	GP	0.089(0.014)	0.096(0.018)	0.18
	PU	0.056(0.017)	0.051(0.022)	0.31
	Thal	-0.004(0.0004)	0.0005(0.002)	0.009**
PCS	CN	0.035(0.012)	0.031(0.016)	0.24
	RN	0.071(0.020)	0.099(0.013)	0.001**
	SN	0.075(0.013)	0.109(0.010)	0.000002**
	GP	0.097(0.006)	0.105(0.008)	0.014*
	PU	0.066(0.014)	0.058(0.022)	0.185
	Thal	0.014(0.003)	0.015(0.002)	0.2
DCS	CN	-0.004(0.002)	-0.003(0.002)	0.082
	RN	-0.005(0.003)	-0.002(0.001)	0.007**
	SN	-0.004(0.001)	-0.002(0.001)	0.004**
	GP	-0.003(0.001)	-0.002(0.001)	0.085
	PU	-0.003(0.001)	-0.002(0.001)	0.033*
	Thal	-0.012(0.002)	-0.010(0.001)	0.004**

Table 5.1: **ROI analysis of PD vs controls for QSM, PCS, and DCS.** Susceptibility values are in ppm with standard deviation presented in the parentheses. P values from one-tailed two-sample t-tests are displayed in the last column. Symbols of "*" indicate significant difference: $*p < 0.05$, $**p < 0.01$. CN: caudate nucleus; RN: red nucleus; SN: substantia nigra; GP: global pallidus; PU: putamen; Thal: thalamus.

5.2 Other clinical applications

There has been quite a lot of attempts to identify biomarkers for degenerative diseases such as Alzheimer's Disease (AD) [59, 27], Multiple sclerosis (MS) [26, 120, 128, 139] using QSM. However, in both cases, the pathology involves both paramagnetic iron (such as iron rim in MS [3], and iron core of protein plaques in AD [116]) and diamagnetic protein aggregation or myelination changes[10, 12, 44, 37]. The coexistence situation of susceptibility sources makes QSM less sensitive to the underlying molecular composition alterations due to the disease progression. DECOMPOSE-QSM could be a good candidate to provide additional information on the contribution of paramagnetic and diamagnetic changes individually.

Chapter 6

Application of DECOMPOSE-QSM for Susceptibility Tensor Imaging (STI)

6.1 Introduction

Biological tissue's bulk magnetic susceptibility can be measured non-invasively through an MRI technique called quantitative susceptibility mapping (QSM). The tissue microstructure of an imaging voxel is very complex. In many brain regions, the measured susceptibility depends on the angle between the underlying structure and the B_0 field direction [71, 126, 125]. Similar to the description of diffusivity anisotropy, susceptibility anisotropy can be described by a second-order tensor. Using susceptibility measurements at multiple B_0 orientations, the second-order susceptibility information can be characterized using the susceptibility tensor model, namely the method of susceptibility tensor imaging (STI) [74]. It has been shown that the major contribution to susceptibility anisotropy is from the radially arranged myelin lipids concentrically wrapping around the axon. Therefore, STI is able to reflect the orientations of white matter (WM) fiber tracts [71, 75, 124].

The coexistence of paramagnetic and diamagnetic (with respect to the reference species) susceptibility sources within a voxel affects susceptibility tensor quantification. It is conventionally believed that the susceptibility anisotropy is from the radially arranged myelin lipids. Therefore, most of the STI studies are focused on revealing the white matter fibrous structures, and the effect of paramagnetic tissue on the susceptibility anisotropy is ignored. The co-existing isotropic paramagnetic susceptibility could dilute the effect of the diamagnetic anisotropy. It is also possible that the paramagnetic species can construct susceptibility anisotropy on its own.

There have been several efforts put into modeling and resolving the mixed susceptibility sources with different data scheme [25, 37, 100, 101, 105]. Among those, the chi-separation method used a linear model to differentiate the contribution of paramagnetic and diamagnetic

susceptibility sources to the R_2' relaxation rate and bulk susceptibility, which requires both T_2 and T_2^* measurement sequences [105]. Another method that only uses gradient-recalled echo (GRE) signal namely DECOMPOSE-QSM [25] was proposed to resolve the mixture situation using a complex multi-exponential nonlinear signal model.

Here, we apply the DECOMPOSE-QSM methodology on a multi-orientation dataset of postmortem chimpanzee brain [43] in order to investigate, for the first time, the anisotropic properties of diamagnetic and paramagnetic components and identify a potential connection between the microstructural spatial organization of myelin and glial cells. Further, we hypothesize that STI can be benefited from the separation of these properties, in depicting the primary axonal directions of WM.

6.2 Methods

6.2.1 Sample Preparation

The brain sample used in this experiment originates from an adult male chimpanzee, who died from natural causes. The whole brain was extracted within an acceptable post-mortem interval and preserved in 4% paraformaldehyde (PFA). After six months of fixation, prior to imaging, the PFA was washed out in phosphate-buffered saline (PBS) at pH 7.4 for 24 days. During imaging, the brain is submerged in non-proton solution (Fomblin®; Solvay Solexis, Bollate, Italy). Sample is enclosed in a custom designed 3D-printed container that supports re-orientations within the scanner head coil. The dataset is previously used and reported, along with all the relevant details of extraction, preservation and quality of the tissue and the measurements [43]

6.2.2 MRI acquisition

The inverse problem of the STI model is intrinsically ill-posed when the range of angles is limited. In this study, since a postmortem sample was used, images are acquired at a large number of angles.

MRI datasets were acquired on a 3T MAGNETOM Skyra Connectome MRI scanner (Siemens Healthineers, Erlangen, Germany) with a maximum gradient strength of 300 mT/m. To record the susceptibility anisotropy, 61 unique directions of 3D Multi-Echo Gradient Echo (ME-GRE) volumetric images were acquired with the following parameters TE1/TE2/dTE/TE12 = 3.54/6.98/3.75/44.48 ms, TR = 50 ms, and 1 mm isotropic native resolution. Additionally, DTI dataset was acquired for the same specimen with the same scanner. Sixty gradient directions and six b0 images of diffusion-weighted (DW) 3D-Seg-EPI [38] were acquired with 1mm isotropic resolutions, TR = 10.4 s, b = 5000 s/mm2. The dataset is previously used and reported [43]

6.2.3 Data processing and susceptibility tensor calculation

The data processing pipeline is illustrated in Figure 6.1 The complex-valued ME-GRE images from 32 individual coils were combined and processed using STISuite (`https://people.eecs.berkeley.edu/~chunlei.liu/software.html`)for each direction. Briefly, the phase of each coil is firstly unwrapped using Laplacian based method [70]. Then the 3D image volume is recovered by the weighted sum of the magnitude and phase respectively. The unwrapped phase is filtered by V-SHARP [67] with spherical mean value filter radius of 12 mm. QSM of each echo was calculated using the STAR-QSM algorithm [123] with 12 mm padding. The echo-dependent QSM and magnitude volumetric images of each direction were input into DECOMPOSE-QSM [25] to produce PCS and DCS maps (Figure 6.2). The multi-direction volumes were registered to a reference volume (the first direction) using rigid-body 6-parameter model transformation in FSL [57]. The effective B_0 field orientation of each direction is calculated using the rotation component of the transformation matrix. The transformation matrix was applied to QSM, PCS, and DCS respectively. QSM averaged along the echo dimension is used for STI reconstruction in the lab frame [74]. Similarly, PCS and DCS were used to calculate PCS and DCS tensors in the lab frame.

Eigen decomposition was performed on the calculated tensors. The three principal susceptibility χ_1, χ_2, χ_3 are numbered in descending order. Susceptibility anisotropy defined as $SA = \chi_1 - (\chi_2 + \chi_3)/2$ was calculated using the eigenvalues of the tensors (the first eigenvalue χ_1 is the biggest eigenvalue). The eigenvector corresponding to the largest eigenvalue χ_1 indicates the primary susceptibility (or susceptibility component) direction. Similar to the color-coding of diffusion MRI, RGB colors are used to color code the direction of the primary eigenvector as follows: left-right is coded as red, anterior-posterior is coded as green, and superior-inferior is coded as blue.

Each volume of diffusion-weighted images are registered to the ME-GRE space using affine transformation with ITK-SNAP (Version 3.8.0) [137]. The diffusion-encoding gradient orientations are transformed using the rotation component of the transformation matrix. The diffusion tensor of the volume is calculated in the ME-GRE space. DTI fractional anisotropy (FA) was used to weigh the RGB color-coded primary eigenvector map for diffusion tensors and susceptibility tensors. The mean magnetic susceptibility (MMS) defined as the trace of the QSM-STI tensor $MMS = (\chi_1+\chi_2+\chi_3)/3$ was calculated and used to provide anatomical guidance for the color-coded primary eigenvectors of the QSM, PCS, and DCS susceptibility tensors.

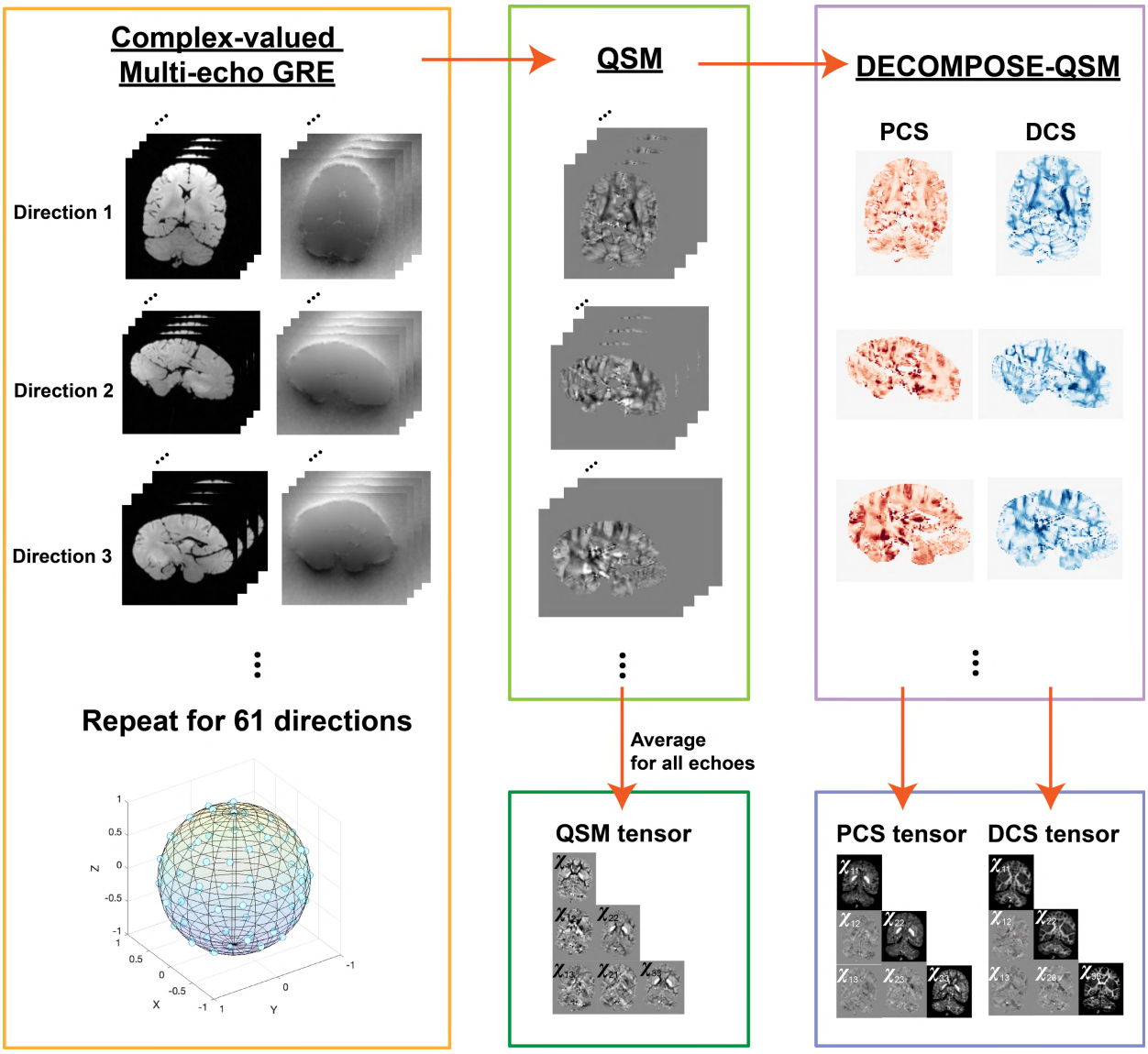

Figure 6.1: **Schematic processing pipeline of susceptibility tensor.** Complex-value Multi-echo GRE data of each direction is used to reconstruct QSM echo by echo. Then the echo dependent QSM with the original multi-echo magnitude images are used for DECOMPOSE-QSM producing PCS and DCS maps of each orientation. 61 directions of the echo averaged QSM, PCS and DCS are then used to calculate susceptibility tensor, respectively. The B_0 field orientation is calculated through the rotation component of the rigid body transformation from each volume to the reference (the first direction) volume.

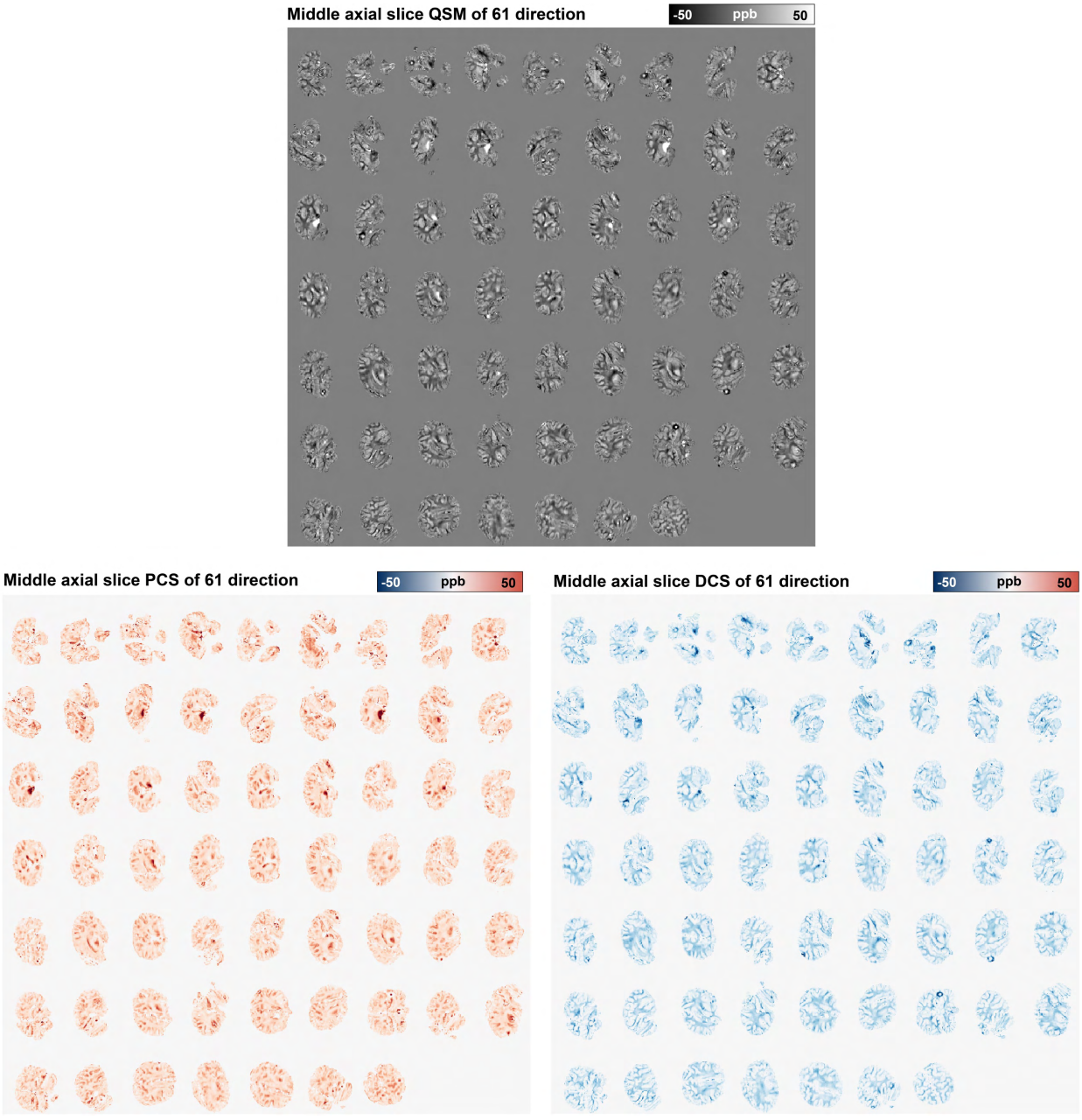

Figure 6.2: **QSM, PCS and DCS of all 61 orientations.** Middle axial slices are shown for illustration.

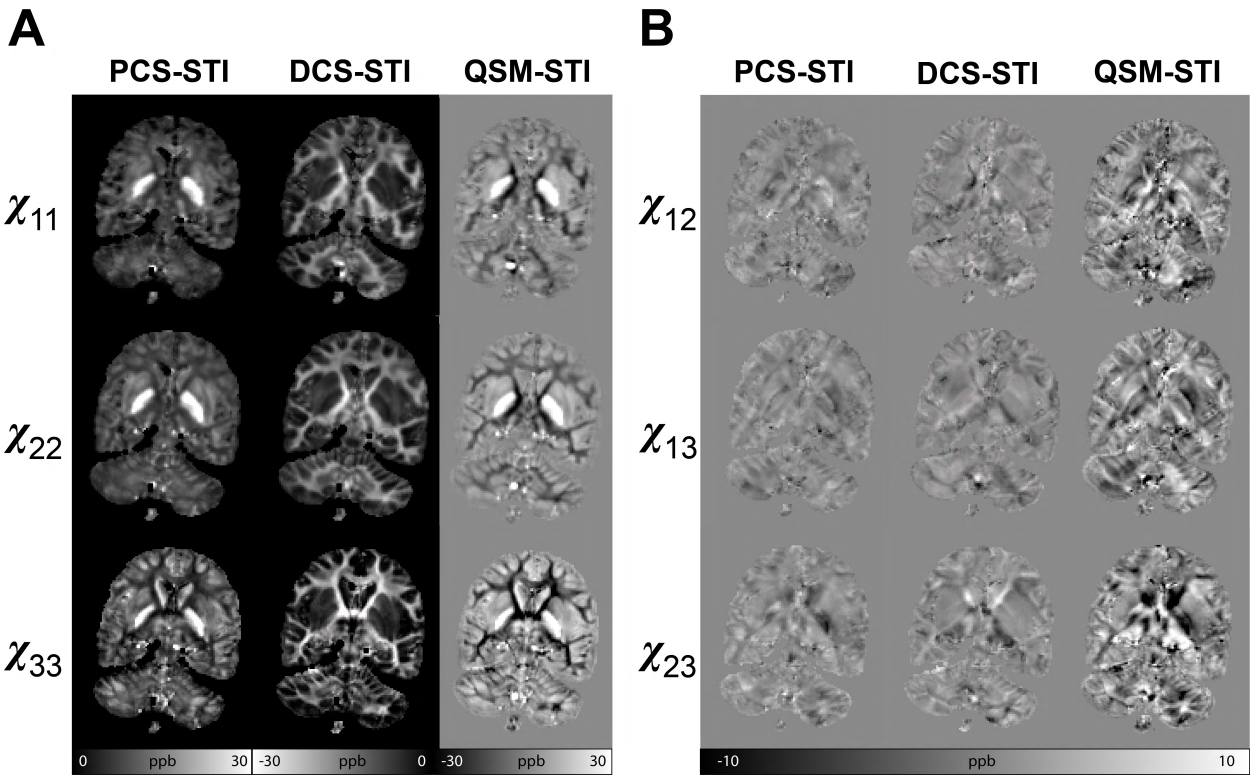

Figure 6.3: **Tensor element maps for PCS, DCS, and QSM based STI tensor.** A) The 3 diagonal elements of the susceptibility tensors from different methods. The PCS-based tensor has only positive values corresponding to paramagnetic susceptibility, while the DCS-based tensor has only negative values (shown in inverse contrast for better visualization) corresponding to diamagnetic susceptibility. The conventional QSM based STI tensors have both positive and negative values, with the positive value reflecting paramagnetism and the negative value reflecting diamagnetism. The DECOMPOSE-based method showed continuous tissue susceptibility changes. B) The off-diagonal elements of susceptibility tensors. The STI tensor's off-diagonal elements contains more prominent streaking artifacts. The DCS tensor elements are shown in inverse contrast for a better visualization.

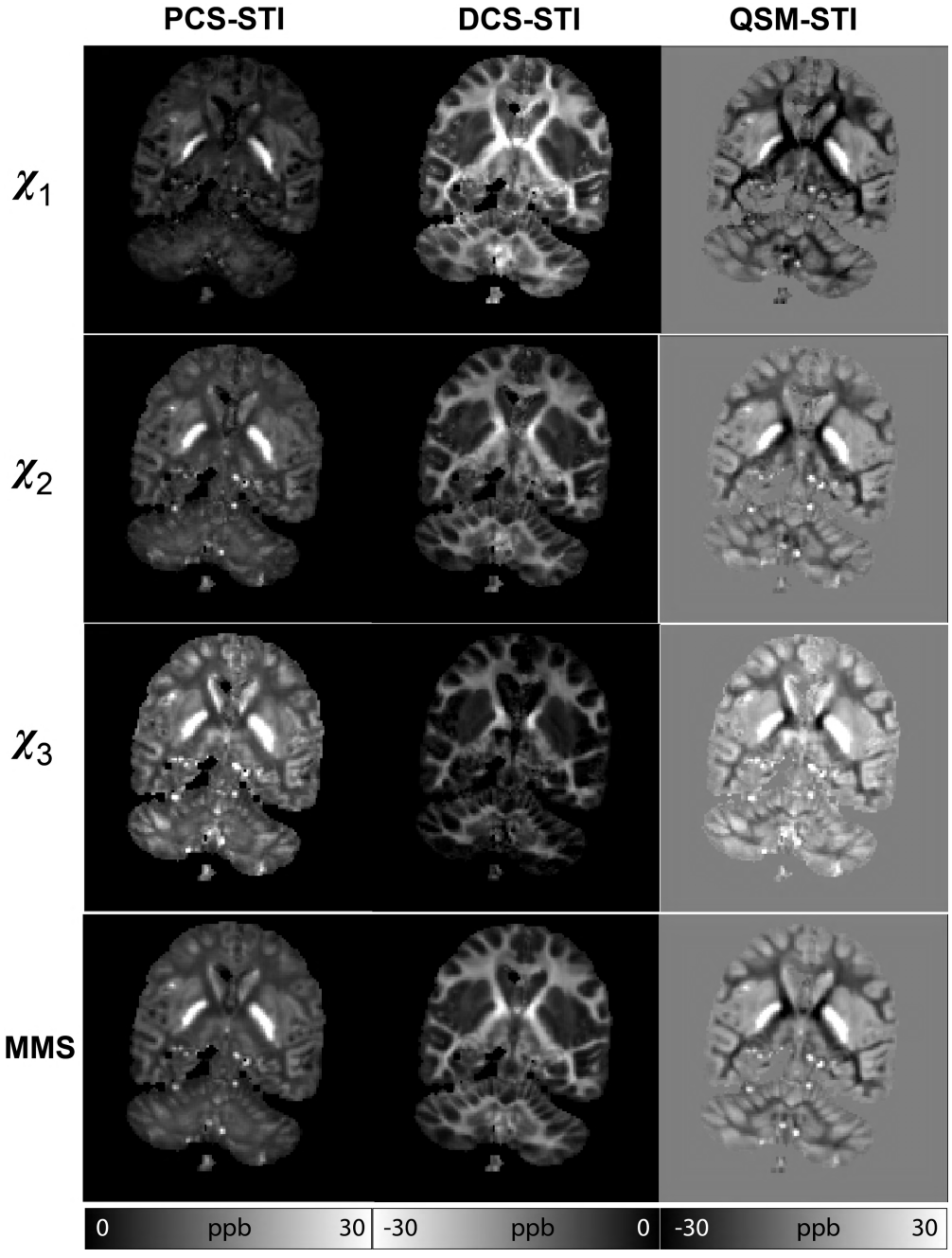

Figure 6.4: **Eigenvalues and the mathematical mean susceptibility (MMS)** of PCS, DCS and QSM based susceptibility tensors.

6.3 Results

6.3.1 DECOMPOSE-STI improves spatial coherence of tensor element maps

Susceptibility tensors are calculated using multi-direction measurements of PCS, DCS and QSM, referred to as PCS-STI, DCS-STI, and QSM-STI respectively. For a representative axial slice, Figure 6.3A shows the diagonal elements of each tensor, and Figure 6.3B shows the off-diagonal tensor elements. The three principal eigenvalue maps of the corresponding slices are shown in Figure 6.4. Overall, PCS-STI aligns with the paramagnetic (bright) region in conventional QSM based susceptibility tensor, while DCS-STI aligns with the diamagnetic (dark) region in conventional QSM-STI. QSM-STI contrast shows the dominant susceptibility at each voxel, therefore, little diamagnetic anisotropy is revealed in deep gray matter and limited paramagnetic anisotropy is revealed in white matter. Tensor element maps from DECOMPOSE-STI, both PCS and DCS based, show spatially continuous and significant tissue susceptibility variations. For example, in the Basal Ganglia region, paramagnetic value is dominant in conventional QSM-STI, while DCS-STI shows non-zero diamagnetic susceptibility contribution. In the off-diagonal element maps, QSM-STI contains more prominent streaking artifacts compared to the off-diagonal elements of PCS-STI and DCS-STI.

6.3.2 DTI fractional anisotropy (FA) and susceptibility anisotropy (SA)

Figure 6.5A shows the DTI FA map and SA map calculated using PCS-STI, DCS-STI and QSM-STI. DCS-STI-based SA is the most similar to the FA map from DTI and both maps delineate the major white matter structures (e.g. the corpus callosum, the internal capsule, the anterior corona radiata). SA maps of the QSM-STI appear to be a composite of SA maps from PCS-STI and DCS-STI. Due to the composition appearance, QSM-STI based SA map does not delineate the structure as well as the separated SA maps from PCS-STI or DCS-STI. Figure 6.5B shows the distribution of PCS-STI and DCS-STI SA values for different regions of interest (ROI). The volumetric ROI mask is generated by thresholding the FA at various levels. A representative slice of the mask is shown at the top row (Figure 6.5B). As the FA threshold level increases, the mask concentrates at the major white matter tracts where the orientation of the tract is known to be more cohesive. The center of the DCS-STI SA distribution shifts towards higher values as the FA threshold increases while the center of the PCS-STI SA distribution remains at around 0.003 ppm.

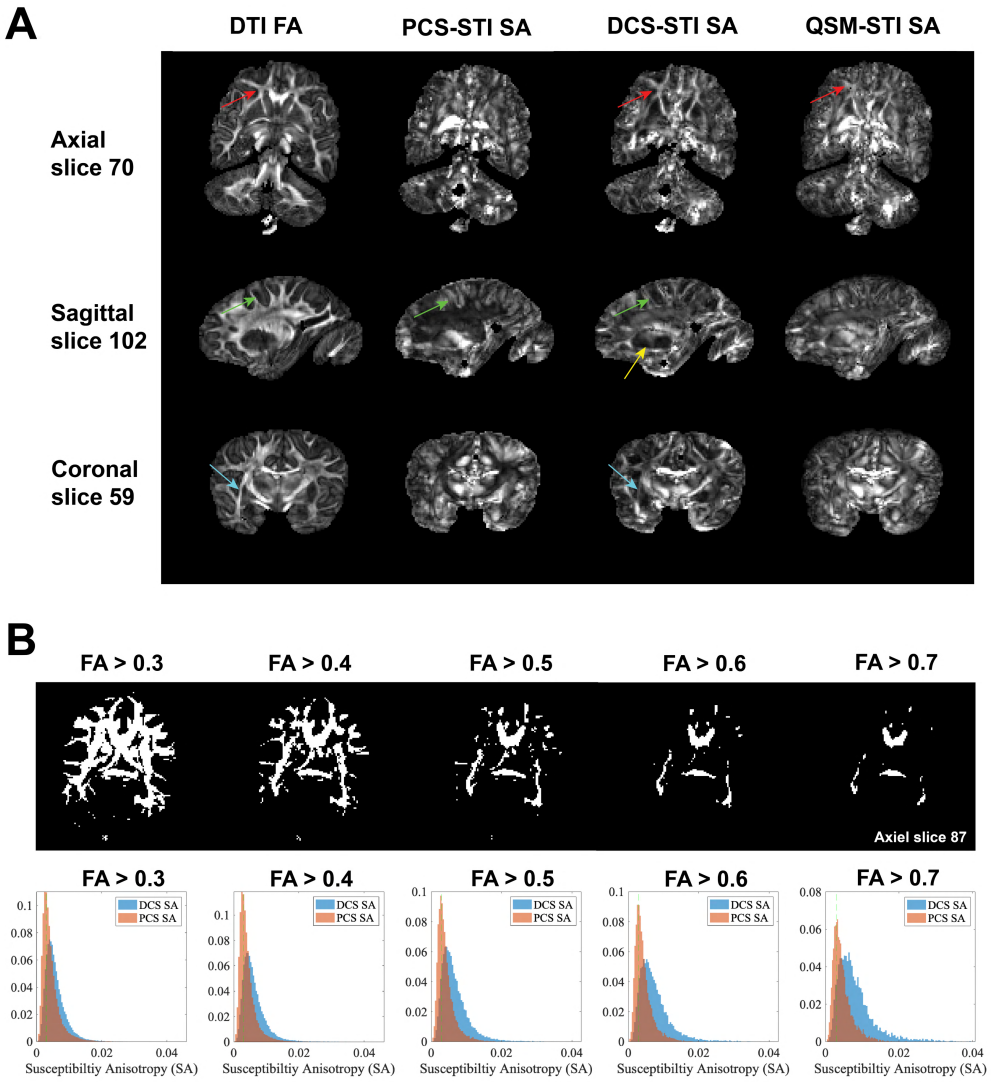

Figure 6.5: **Diffusion based fractional anisotropy (FA) and susceptibility anisotropy (SA) comparison.** A) DTI FA and PCS, DCS and QSM based susceptibility anisotropy of 3 representative slices are compared. The DCS based SA map looks the most similar to the DTI based FA map. The major white matter tracts are bright indicating high structural and susceptibility anisotropy. The PCS highlights the susceptibility anisotropy in deep gray matter indicating the existence of underlying anisotropic susceptibility arrangements. QSM based anisotropy overall seems to be the composite of PCS and DCS based anisotropy with less prominent delineation of structures. Regions that show strong differences are highlighted by color-coded arrows. B) SA distribution for a different threshold level of FA values. With a higher FA threshold, the mask picks out region with more coherent white matter bundles. The DCS based SA distribution shift towards higher values while PCS based SA remains, as FA threshold gets higher. The vertical green dash line indicates SA value at 0.003 ppm.

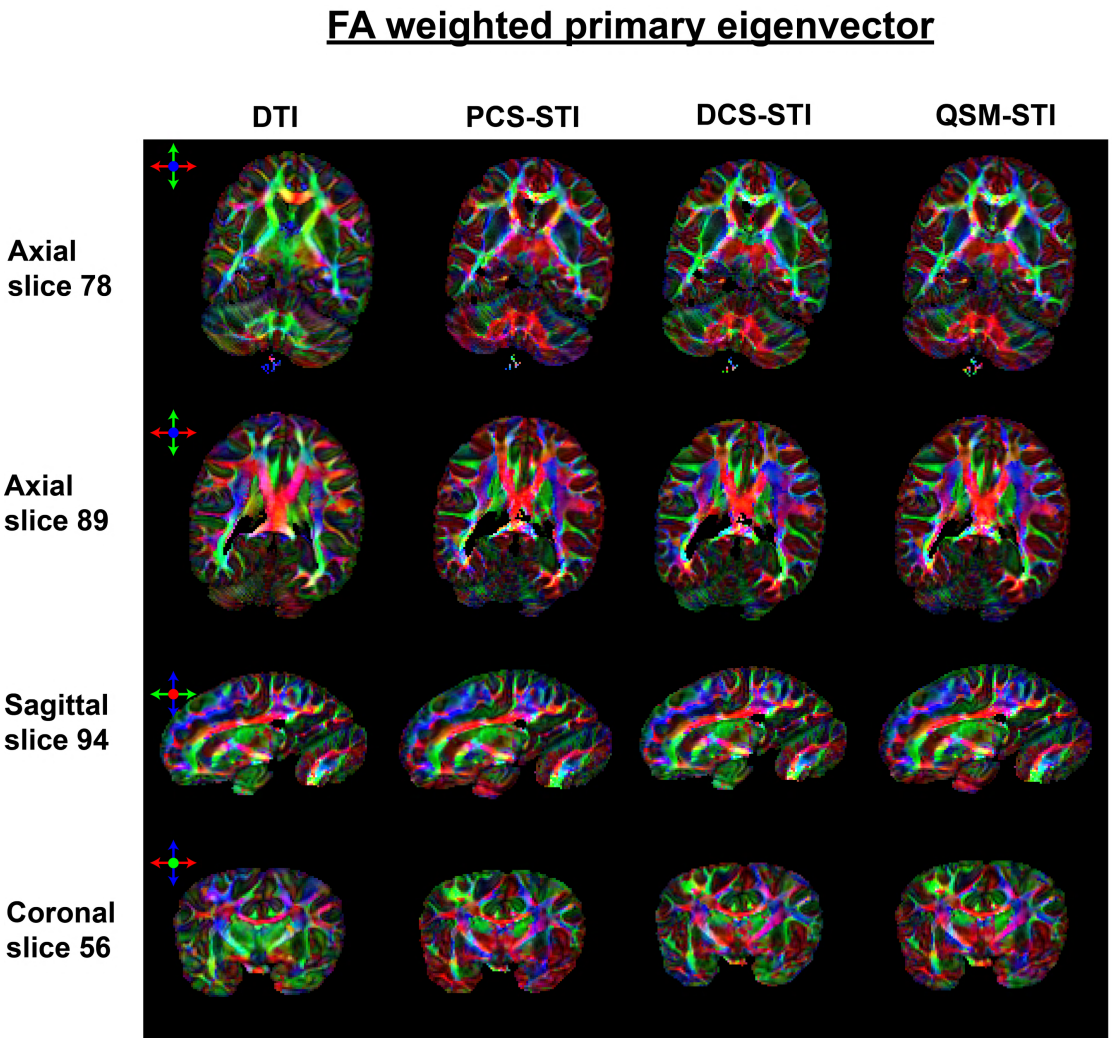

Figure 6.6: **RGB Color-coded FA weighted primary eigenvector map of DTI, PCS-STI, DCS-STI, QSM-STI.** Red: left-right. Green: anterior-posterior. Blue: superior-inferior. Overall, vectors at major white matter tracts (e.g., corpus callosum, cerebrospinal tract, etc.) are showing alignments for all four types of tensors. The external capsule in the DCS based susceptibility eigenvector appears to be closest to the DTI-based eigenvector.

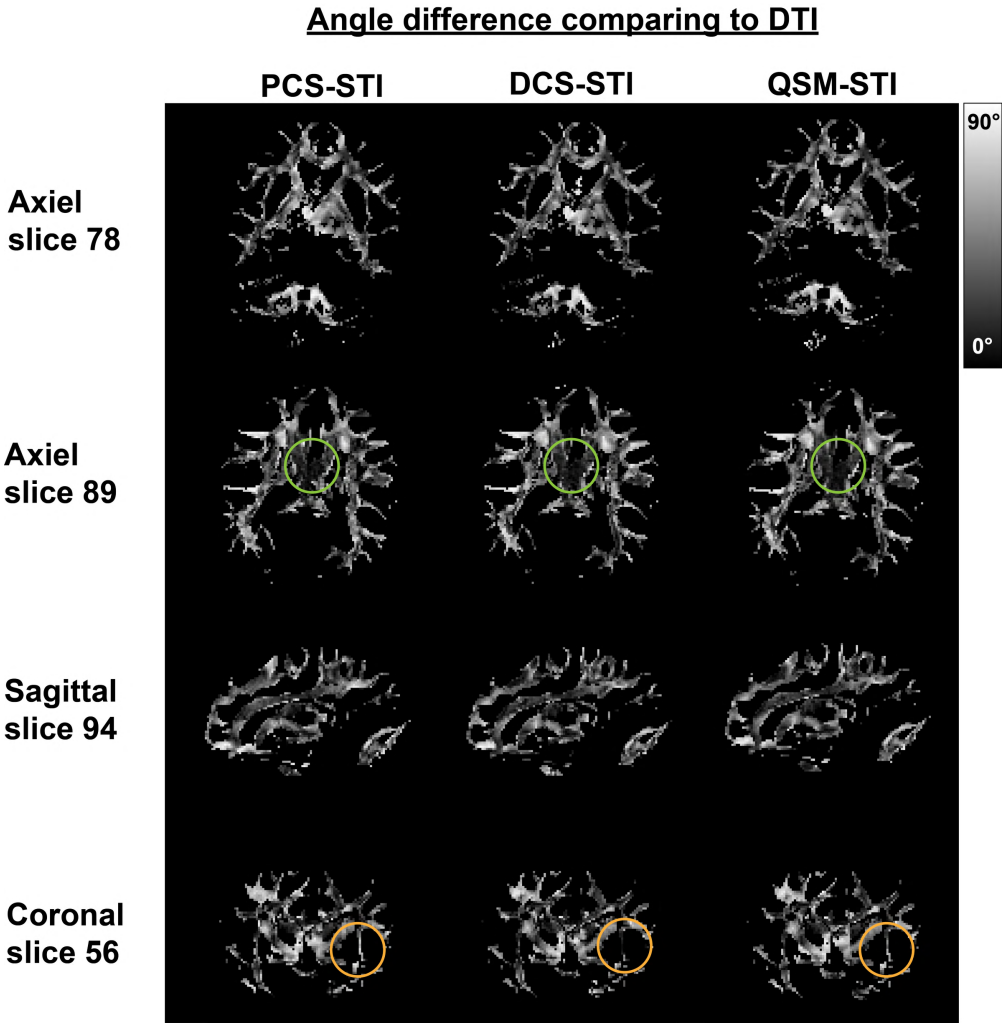

Figure 6.7: **Angle difference of primary eigenvectors between diffusion tensors and susceptibility tensors.** A mask of FA > 0.3 is used to highlight the white matter area. Angle 0° means the susceptibility tensor based primary eigenvectors align exactly with the diffusion tensor based primary eigenvector. Angle 90° means the susceptibility tensor based primary eigenvectors are perpendicular to the diffusion tensor based primary eigenvector. Green circle is at the body part of the corpus callosum. All types of susceptibility tensor eigenvector align with diffusion tensor eigenvector. The orange circle is at the external capsule. Comparing to the other two types of susceptibility tensors, DCS based susceptibility tensor recovers a more similar direction as the diffusion tensor.

6.3.3 FA-weighted primary eigenvector map of diffusion tensors and susceptibility tensors

RGB color-coding is used to visualize the primary eigenvector of diffusion tensors and susceptibility tensors (Figure 6.6). Diffusion-based FA map is used to weigh the RGB map such that the major white matter tracts are focused. Overall, primary eigenvectors of all tensors align well in major white matter fibers, for example, the dominant red color from the body section of the corpus callosum, the purple/blue color of the cerebrospinal tracts, the green color of the superior longitudinal fasciculus and inferior longitudinal fasciculus. The angle differences comparing STI to DTI eigenvectors are shown in Figure 6.7. Similar to the observation of the SA map, the QSM-STI primary eigenvector seems to be the mixture of the primary eigenvector of the PCS-STI and DCS-STI. At the external capsule, DCS-STI is the only susceptibility-based tensor to recover a similar fiber direction as the DTI suggests.

6.3.4 Deep gray matter structures

The non-weighted and RGB color-coded primary eigenvector maps with zoom-in views of deep gray matter regions are shown in Figure 6.8. The corresponding SA maps are shown in Figure 6.9. Overall, susceptibility tensors reveal more details orientation information in deep gray matter, while diffusion tensor shows subtle contrast in terms of revealing structure orientations. Figure 6.8A shows a zoom-in view of the substantial nigra (SN). While DTI is unable to resolve the structure, susceptibility tensor primary eigenvectors show various fibrous substructure orientations. The PCS-STI based primary eigenvector estimation shows the most coherent directions within the SN region, comparing to DCS-STI and QSM-STI based eigenvector estimations. A zoom-in over the basal ganglia region is shown in Figure 6.8B. PCS-STI based eigenvector shows distinct sub-regional orientations within the putamen area and the globus pallidus. The eigenvector from DCS-STI shows a similar trend but the contrast is not as prominent and continuous as it is in the PCS-STI eigenvector map. Figure 6.8C shows a zoom-in view of the thalamus region. STI based eigenvector and SA map show groups of coherent structures that resemble the nuclei within the thalamus, while DTI eigenvector maps exhibit uniform patches within the thalamus.

6.3.5 White matter structures

Figure 6.10 shows a few examples of zoom-in views of white matter structures. The corresponding SA maps are shown in Figure 6.11. Figure 6.10A zooms in on the basal ganglia. The red color structure (highlighted by the hand-drawn yellow curve) in between putamen and globus pallidus stands out in PCS-STI, DCS-STI, and QSM-STI eigenvector maps, coinciding with the lateral medullary lamina. In comparison, DTI only shows a hint of red in the according area. The corpus callosum in Figure 6.10B is revealed clearly through all methods. Figure 6.10B zooms in on an area that contains fibers of various orientations. Specifically, the external capsule (to the left of the yellow line), stands out in the DCS-STI

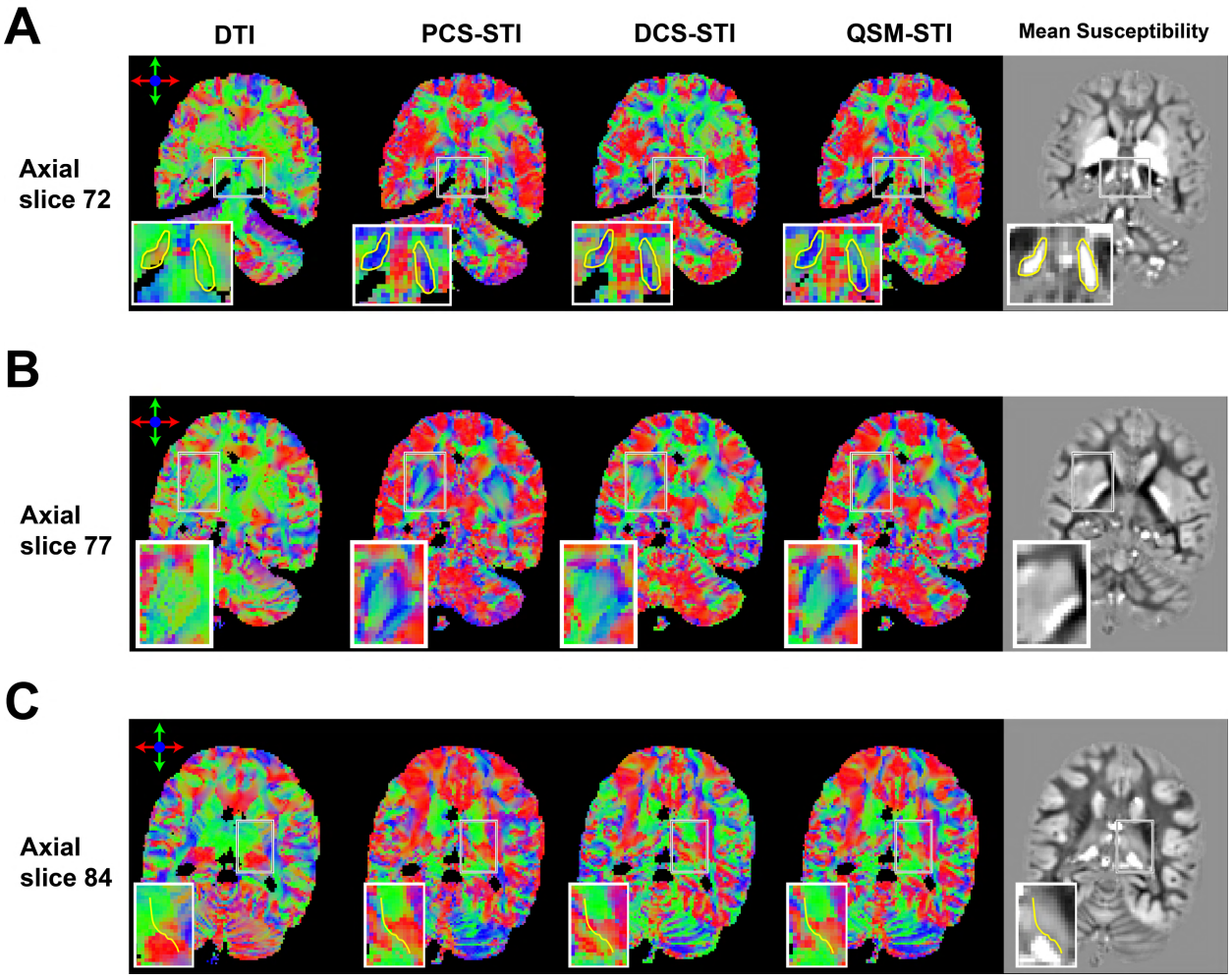

Figure 6.8: **Color-coded primary eigenvector map of DTI, QSM-STI, PCS-STI, DCS-STI with zoomed-in view of three deep gray matter regions.** A) Zoom in on substantia nigra (SN) with highlighted SN boundary. Within the SN boundary, PCS-STI shows the most coherent eigenvector direction. B) Zoom in on basal ganglia. PCS-STI shows continuous eigenvector direction distribution in putamen and globus pallidum. C) Zoom in on thalamus with the highlight at the internal medullary lamina.

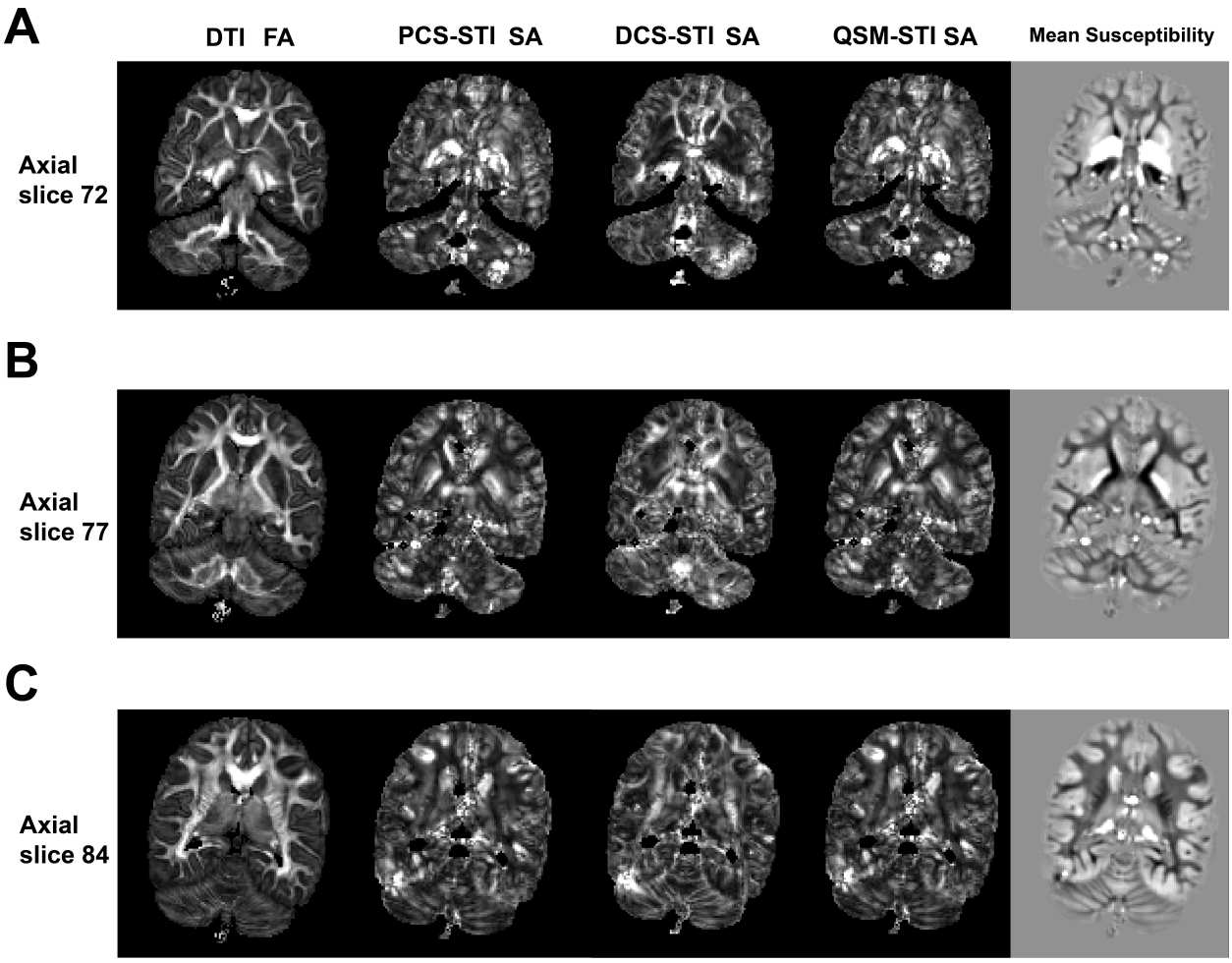

Figure 6.9: **FA and SA map of corresponding slice for Figure 6.8.** Bright region means high fractional or susceptibility anisotropy.

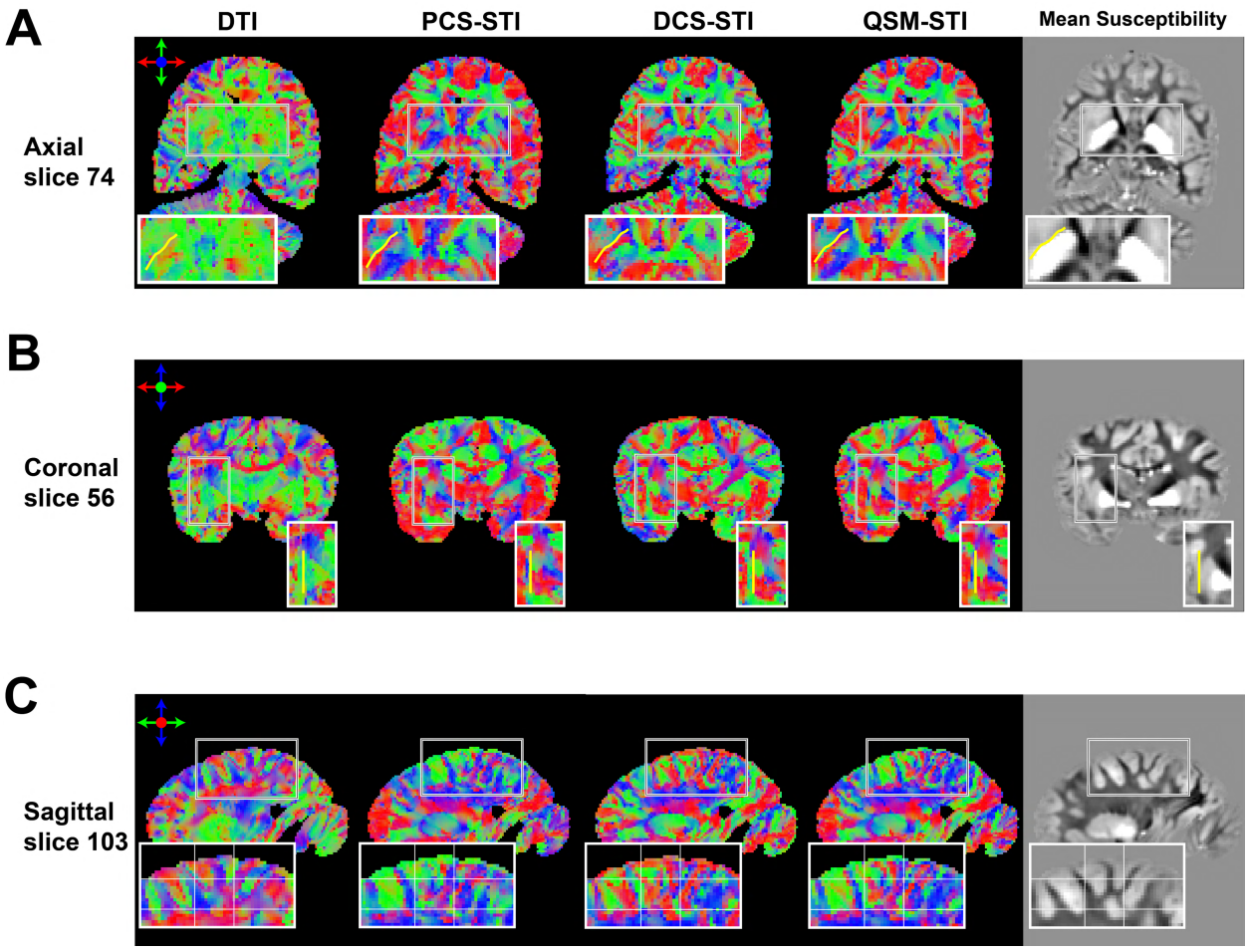

Figure 6.10: **Color-coded primary eigenvector map of DTI, QSM-STI, PCS-STI, DCS-STI with zoomed-in view of three white matter regions.** A) Zoom in with the highlight of lateral medullary lamina. B) Zoom in with highlight at external capsule. C) Zoom in on cortical area. The white grid is for visual comparison guidance.

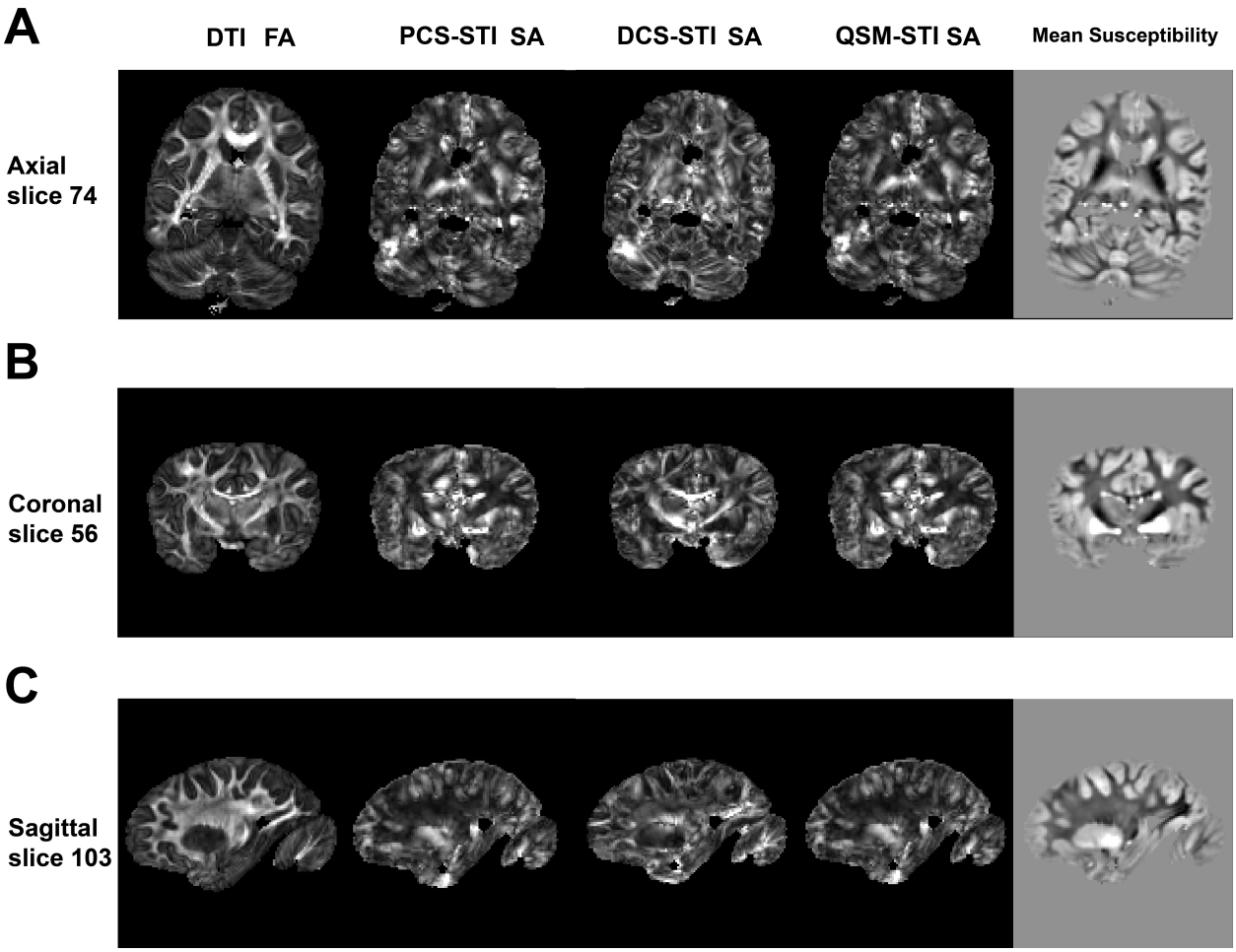

Figure 6.11: **FA and SA map of the corresponding slice for Figure 6.10.** Bright region means high fractional or susceptibility anisotropy.

eigenvector maps, matching the appearance in the DTI eigenvectors. However, the PCS-STI and QSM-STI are not able to depict this thin structure of the external capsule with the native 1mm isotropic resolution. The eigenvector map from STI shows a complex structure in deep gray matter and the crossing of the cerebrospinal tract and corpus callosum. The zoom-in view of Figure 6.10C looks at the cortical region. The DCS-STI shows curving structures following the gyrus. However, STI and DTI in this region do not seem to have high alignments in terms of the eigenvectors.

6.4 Discussion

6.4.1 Paramagnetic susceptibility anisotropy is observed

Diamagnetic susceptibility anisotropy in the brain white matter is observed in many previous studies [8, 63, 71, 72, 74, 75]. The radially aligned multi-sheath double-layered myelin lipid molecules are the main sources of the macroscopic susceptibility anisotropy in the brain. According to the radially arranged lipid shell model, considering the diamagnetic nature of the myelin lipid, the observed susceptibility is the highest in signed value when the B_0 is parallel with the axon long axis. Therefore, the primary eigenvector of the signed-value susceptibility tensor reveals the axon fiber orientation. This model is largely correct when the underlying microstructure is mostly well aligned fully myelinated major white matter fiber bundles. However, in this study, we have observed that the paramagnetic component susceptibility also exhibits anisotropy in both white matter and gray matter, but more prominently in the gray matter.

Though the source of the magnetic susceptibility anisotropy is considered to be occurring from the radial arrangement of the diamagnetic myelin lipid around axons [71], certain geometric arrangements of structures will also introduce anisotropy of the magnetization. In the previous study on the hollow cylinder model of myelin sheath [126, 125], both isotropic-only and anisotropic-only susceptibility configurations will produce angle dependent frequency map. However, in the white matter, considering the diamagnetic nature of the myelin lipid, susceptibility configuration containing the anisotropic component will give a closer fit to the *in vivo* measurements. While for the isotropic-only susceptibility configuration, B_0 will be parallel with the long axis only if the underlying molecules are paramagnetic. We hypothesize that the observed PCS anisotropy originates from anisotropically arranged paramagnetic sources such as iron in oligodendrocytes, astrocytes and microglial.

A quick simulation (Figure 6.12A) shows that when paramagnetic particles distribute around the axon in a cylindrical fashion, under various B_0 orientations, the measured susceptibility will change, and shows the highest value when B_0 is aligned with the long axis of the cylinder. This suggests that susceptibility caused by radially arranged myelin lipids and from anisotropically distributed iron both show the highest signed value when B_0 is aligned with the long axis of the axon. In other words, the primary eigenvector from PCS-STI and DCS-STI should be parallel. In Figure 6.6, 6.8, and 6.10, major white matter fiber bundles such as corpus callosum and cerebrospinal tracts show a high agreement of the primary eigenvectors which supports this hypothesis.

Histology images [52] shows the spread of iron at white matter(Figure 6.12B), and electron microscopy images [84] shows that the nonheme iron distributes around the nerve axons (Figure 6.12C) through oligodendrocyte, astrocyte, and microglia. Recently, a glia-based mechanism is used to reveal the white matter fiber structures in the brain [99]. Nissl staining in multiple human brain sample slices were used to reconstruct the structure tensor and glial row orientation density function (gODF) based exactly on the glial organization within myelinated axons. The orientation map derived from the Nissl-based structure tensor aligns

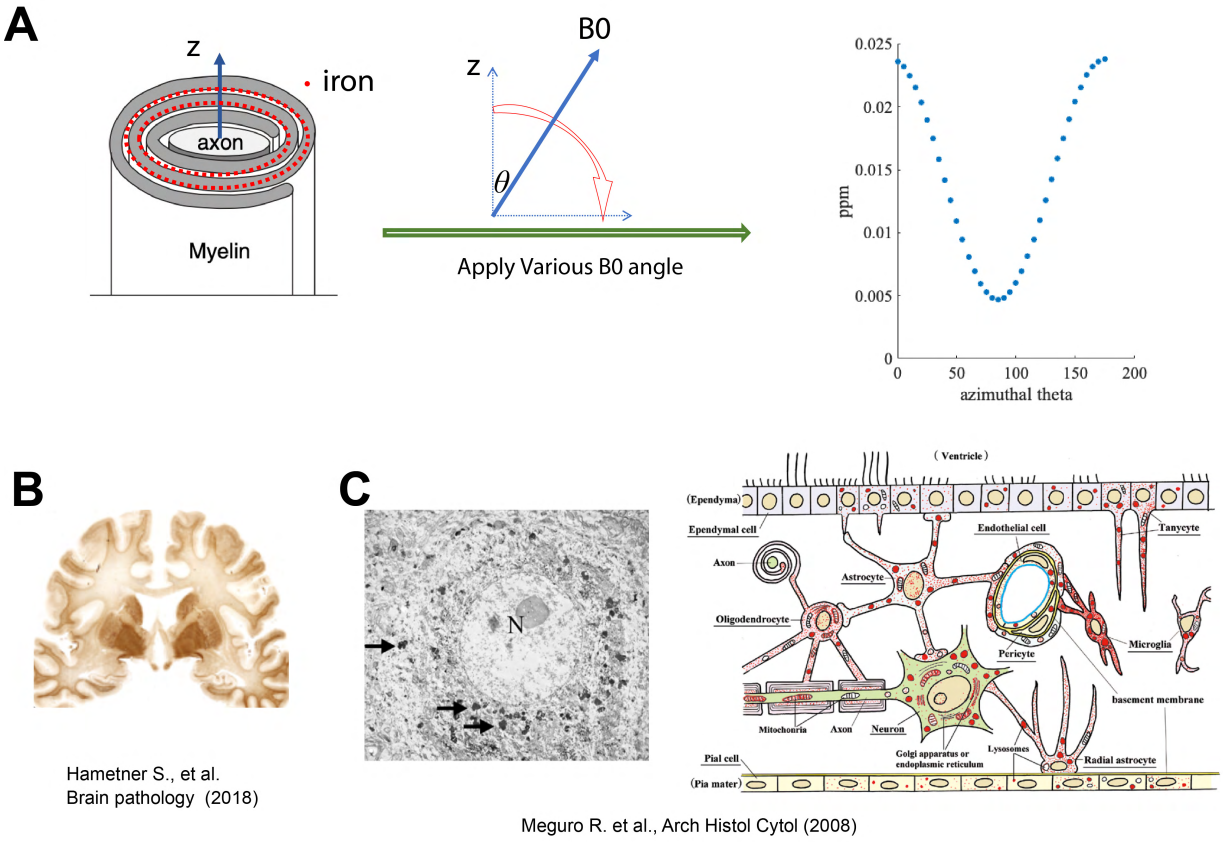

Figure 6.12: **The hypothesis on the origin of PCS anisotropy.** A) Simulation scheme for PCS-STI anisotropy. A voxel contains particles of iron distributes along myelin sheath was used. Various B_0 directions was applied onto the aforementioned voxel, and the total bulk susceptibility measurements are plot with respect to the angle between B_0 and the axon. B) A slice of healthy human brain tissue stained for nonheme iron (Figure 1C from Hametner et al., 2018[52]). C) Electron microscopy image of iron distribution around neuron. Cartoon illustration of subcellular iron distribution in rat brain. (Figure 3C and Figure 9 from Meguro et al., 2008[84])

very well with previously published fiber orientation maps based on postmortem polarized light imaging (PLI). This once again supports the existence of the anisotropy contribution from iron-bearing cell types. It is worth noting that iron distribution is still relatively less cohesive than the myelin structure. Therefore, in the white matter, The SA from DCS-STI is higher than the SA from PCS-STI (Figure 6.5).

6.4.2 Paramagnetic and diamagnetic susceptibility anisotropy coexist

Evidence shows that both paramagnetic iron-rich molecules and diamagnetic myelin lipids contribute to magnetic susceptibility anisotropy. From Figures 6.5, 6.8, and 6.10, QSM-based STI appears to show the summation effect of the DCS-STI and PCS-STI. At regions with high paramagnetic susceptibility, the SA and the primary eigenvector direction of QSM-STI is close to that in PCS-STI (e.g., deep gray matter). At regions with high diamagnetic susceptibility, the SA and the primary eigenvector direction of QSM-STI are close to that in DCS-STI (e.g., white matter tracts). The conventional QSM-STI image interpretation can be tricky when the susceptibility mixture happens since iron and myelin could both cause frequency shifts. STI based on separated susceptibility components could provide additional information on the independent contribution of paramagnetic susceptibility anisotropy and diamagnetic susceptibility anisotropy. In this dataset, for the external capsule, superior longitudinal fasciculus and inferior longitudinal fasciculus regions DCS-STI is the only contrast that shows cleaner directions and is close to DTI results comparing to QSM-STI and PCS-STI. This is because ,in those regions, the QSM value can be subtle, after the separation, PCS-STI serves almost like a denoiser to the DCS-STI by removing the non-diamagnetic susceptibility anisotropy resulting in more coherent eigenvector estimation. Similarly, in the basal ganglia where the dominant tissue type is iron rich, PCS-STI would give more reliable information of the underlying tissue arrangement and microstructures.

6.4.3 DCS anisotropy is similar to diffusion anisotropy in white matter

Overall, DCS-STI based SA appears the most similar to the diffusion FA compared to PCS-STI and QSM-STI SA in the white matter (Figure 6.5, 6.11, 6.12). The FA-weighted RGB color-coded primary eigenvector maps from DCS-STI also resemble the diffusion MRI based primary eigenvector maps the most (Figure 6.6 In white matter major fiber bundles, SA is mostly due to the radially arranged myelin lipids wrapping around the axon, therefore the SA from DCS and FA shows high agreement. However, the fundamental principles of diffusion FA and SA are different. The diffusion FA reflects the anisotropic hindrance of water diffusion while SA describes the magnetization differences while applying B_0 in different directions. In addition to DTI, susceptibility anisotropy could give information about the tissue microstructures. For example, in previous research on the kidney STI

([132]), renal tubule can be revealed in both the inner medulla and outer medulla using STI while DTI only shows clear fibrous structures within the inner medulla of the kidney.

6.4.4 PCS and DCS anisotropy in deep gray matter

In white matter, the major contribution to susceptibility anisotropy is myelin sheath and it aligns well with the diffusion based structural anisotropy eigenvector estimation. In deep gray matter, when the tissue physical structures become complex, and the neuron density gets higher, the diffusion tensor model may not perform as well in terms of providing information of the tissue fibrous microstructures. Susceptibility tensor imaging probes tissue's magnetic biochemical property and tissue microstructural arrangement. In Figure 6.8A, the STI calculated fiber directions at substantia nigra are primarily along superior-inferior, this agrees with the previous human brain high resolution STI measured at 7T [8]. In Figure 6.10A, the red line structure in between putamen and globus pallidus is clearly visible in all susceptibility-based eigenvector maps. This structure corresponds to the thin white matter lateral medullary lamina connecting the putamen and globus pallidus. Separating the susceptibility sources, diamagnetic white matter contribution to the anisotropy will be purer comparing to using only QSM-STI. Therefore, the lateral medullary lamina sandwiched in between two very paramagnetic nuclei are the most clear and clean in DCS-STI based eigenvector map. In Figure 6.8B, the complex tissue directional information at putamen and globus pallidus is recovered using STI. However, since the basal ganglia is iron rich hence it is paramagnetic, and the SA is higher for PCS-STI. The eigenvector map is cleaner using PCS-STI comparing to DCS-STI.

6.5 Conclusion

In summary, DECOMPOSE-STI, a DECOMPOSE-QSM preprocessed susceptibility tensor reconstruction is introduced in this study. The initial demonstration shows that the susceptibility source separation for susceptibility tensors could provide extra tissue property information in addition to the original STI and diffusion MRI. We have observed the existence of paramagnetic susceptibility anisotropy in a postmortem brain sample without dissection of the brain and we hypothesize that this occurs due to the arrangement of paramagnetic iron-bearing molecules (such as glia cells) along the myelinated axons. Further, we show that susceptibility separated tensors could help investigate the tissue type contribution to the susceptibility anisotropy and the separated tensor maps could provide a more coherent and reliable estimation of the underlying anisotropy.

Chapter 7

Further Considerations for DECOMPOSE-QSM

7.1 Accelerating DECOMPOSE-QSM using Multi-layer Perceptron Network

The DECOMPOSE-QSM model solves a nonlinear complex signal model to calculate paramagnetic component susceptibility (PCS) and diamagnetic component susceptibility (DCS). The DECOMPOSE-QSM model is validated with phantom and *ex vivo* temperature-dependent experiments. As the model is highly nonlinear, the long runtime of the optimization-based solver hinders it from being tested in large datasets.

We developed a multi-layer perceptron (MLP) method trained with synthetic data to estimate the parameters of the DECOMPOSE-QSM model. We show that by training purely on simulated data points [30] with temporal additive noise, the deep learning-based solver (DeepDECOMPOSE) is able to achieve the decomposition of QSM and improve robustness to noise.

7.1.1 DeepDECOMPOSE Training strategy and Network Architecture

The goal is to perform fast parameter fitting for the DECOMPOSE-QSM model, which is a summation of three complex exponentials.

To start, we generate random values for $C_0, C_+, C_-, R^*_{2,0}, \chi_+$, and χ_- (with constraints taken into account) that serve as ground truth parameters of the model. The voxel signals are generated using the DECOMPOSE forward model with specific echo time (TE) arrangements with various levels of noise. The training data is generated on the fly during training and validation steps. Since the ground truth parameters are random, the over-fitting issue is not a concern in this study. MLP Solver1(S1) with fixed TE is then built to train point-wise on the parameter maps and noisy signal pairs.

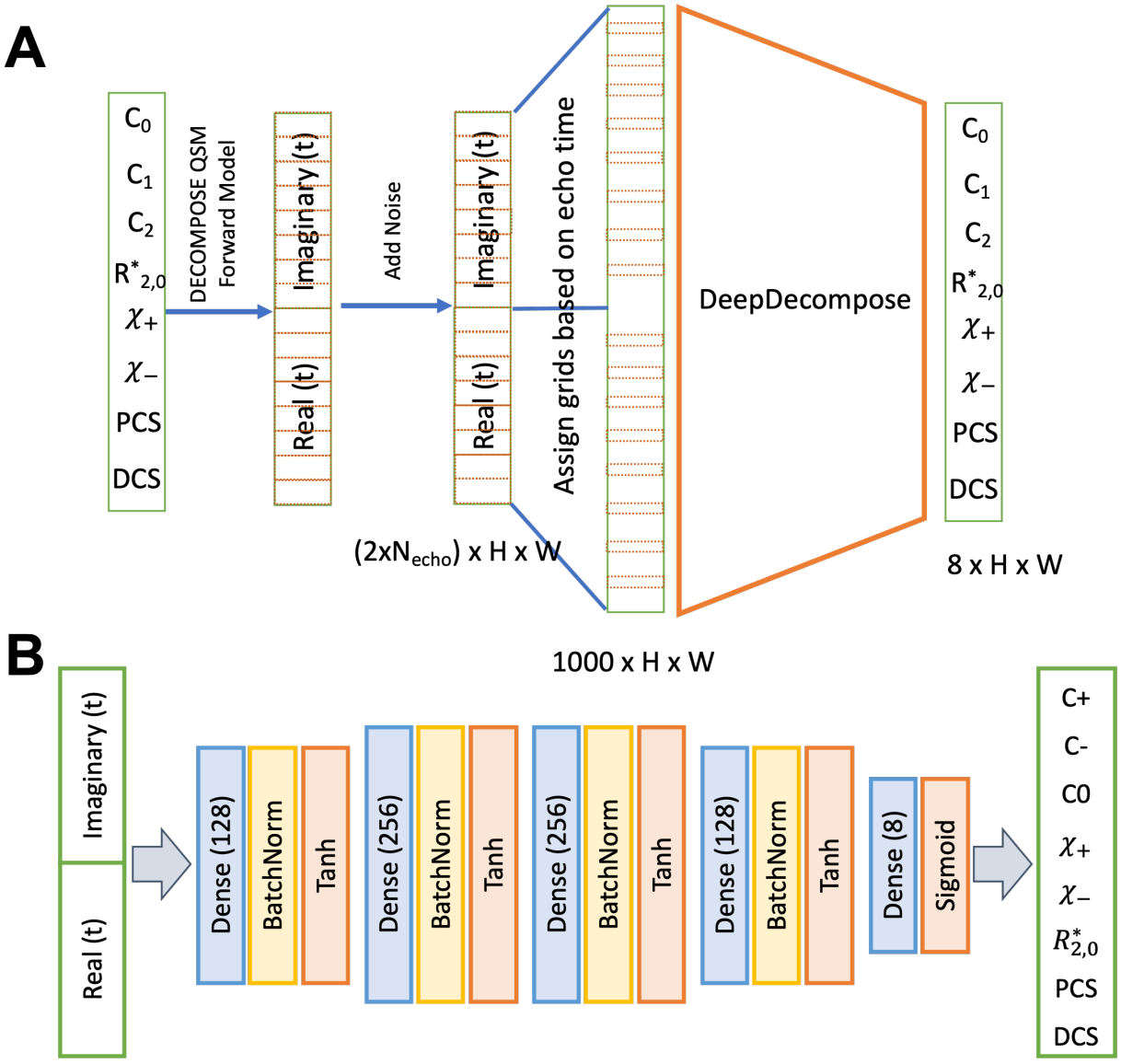

Figure 7.1: **The outline of training strategy (A) and network architecture (B).** Ground truths are randomly drawn within the feasible set of the optimization problem to generate complex signals. Various levels of noise are added to the signal. For fixed echo solver S1, the input is the signal at the fixed echo times. For adaptive echo solver S2, the signal of each time point is assigned to grids of 1-51 ms with 0.1 ms intervals. The model is trained with the summation of the MSE loss of complex signals and the MSE loss of the parameter maps.

Next, to generalize our approach for various numbers of echoes ($5 \sim 24$ are considered), we generate a time grid (0.1ms interval) to fill in the signals based on the TEs. We consider TEs between 1-51ms. We simulate acquired TEs by zeroing out the grid points we do not have, a similar idea to using dropout in a neural network[111]. The inputs are normalized such that they have the same energy with respect to the number of TEs for consistent training and convergence. We refer to this implementation as adaptive echo Solver 2 (S2).

The network structure is shown in Figure 7.1 with five fully connected layers, batch normalization, and hyperbolic tangent as the activation function. The network is implemented using Pytorch[91] as a fully convolutional neural network (CNN) with 1x1 convolutions to accelerate inference on full images.

7.1.2 Stress Test, Validation and Discussion

Figure 7.2A shows simulated signals with various echo times added with various noise levels. The model-predicted curves fit the original clean curve well. In Figure 7.2B, the estimated PCS and DCS from all solvers align well with the ground truth PCS and DCS. The DeepDECOMPOSE solvers show less deviation from the ground truth.

Figure 7.3 shows the simulation results for two different noise levels and corresponding error maps. At around SNR=20, all solvers can resolve the underlying mixture to a certain extent. The DeepDECOMPOSE solvers have similar performances, and both show robust performance with noisy input. With very low SNR (≈ 10) S1 and S2 still can resolve the susceptibility mixture with less error compared to the original solver (S0). However, all solvers show difficulty when dealing with high susceptibility values.

With the same data from Chapter 3, figure 7.4 demonstrates the solvers' performance for the phantom data within 7 ROIs; the difference between S1, S2, and the original solver is minimal. However, the S1 results seem to have shallower contrasts. The *in vivo* tests (Figure 7.5) show that S1 and S2 achieve similar results to the original solver, with most differences occurring around the lateral ventricles. The inference time for a 256×256 image slice takes $<$1s on CPUs (Intel Xeon Silver 4116) and < 20 ms on a GPU (Nvidia Titan Xp).

The training process assumes uniform distributions of the parameters in order to cover as many variations of training samples as possible. However, for *in vivo* case, extreme values can be very rare to occur and some parameter combinations might not exist (but they could exist in a dedicated designed phantom). The discrepancy of the prior distributions could affect the inference quality. The generalization of the trained model to various *in vivo* datasets needs further investigation.

The DECOMPOSE-QSM model is highly simplified with valid assumptions in order to reduce the number of unknowns and improve the feasibility of the optimization problem. Ideally, many more relaxation contrasts (e.g. through multi-parametric MRI scans) and effects can be incorporated in the signal model such as diffusion effects, susceptibility sources geometry, etc. The deep learning framework provides a potential path to solve a more complicated subvoxel susceptibility sources separation model.

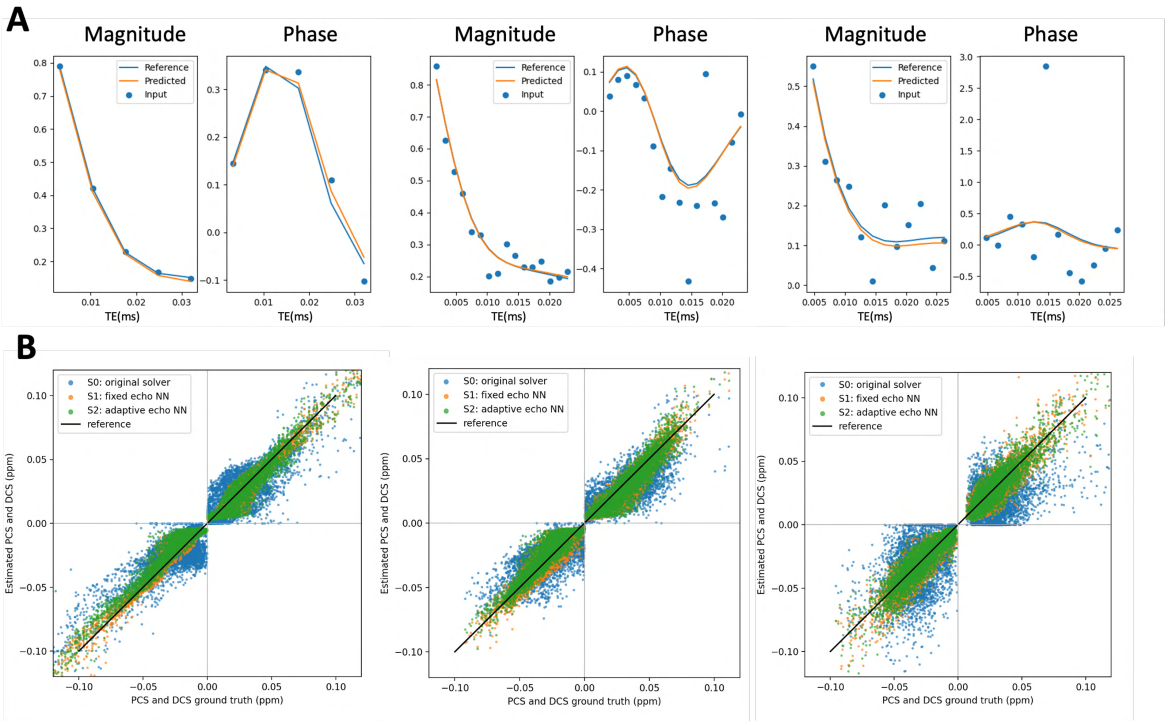

Figure 7.2: **Curve fitting performance with low, middle, and high noise levels and a various number of echoes.** (A) The blue curve is the clean reference. Blue scatters are the signal added with random noise, which is the input of the MLP network. The orange curve is the signal recovered from the estimated parameters outputting from the MLP network. (B) The estimated PCS and DCS from 3 solvers with low, middle, and high noise levels, are compared to the ground truth. S1 and S2 solvers result in tighter distribution around the ground truth.

7.1.3 Conclusion

We evaluate a deep learning approach for estimating DECOMPOSE QSM. With a simple MLP implementation trained on randomly generated data, the solvers with either fixed TE (S1) or adaptive TE (S2) show the ability to perform parameter fitting for the summation of complex exponential models, specifically DECOMPOSE QSM. We show that the spatial continuity is not compromised when training and inference in a pointwise fashion. The deep learning-based solvers are more than two orders of magnitude faster on the CPU (four orders on GPU) than the original optimization implementation and are more robust to measurement noise, in contrast to the original solver.

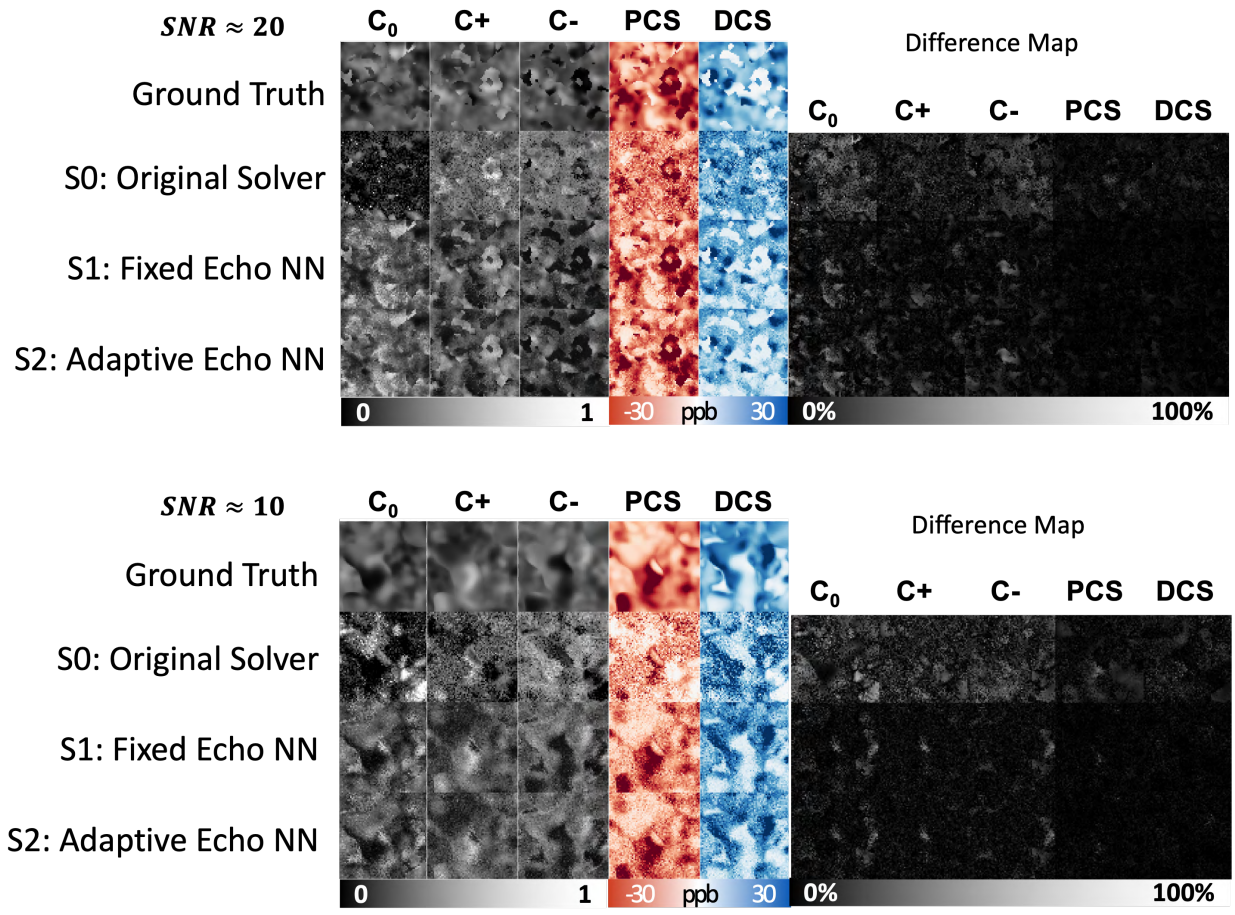

Figure 7.3: **Performances of three solvers with different SNR on ground truth random noise-like parameter maps.** The difference map is calculated as the absolute difference between the results from each solver (S0, S1, S2) and the noiseless ground truth.

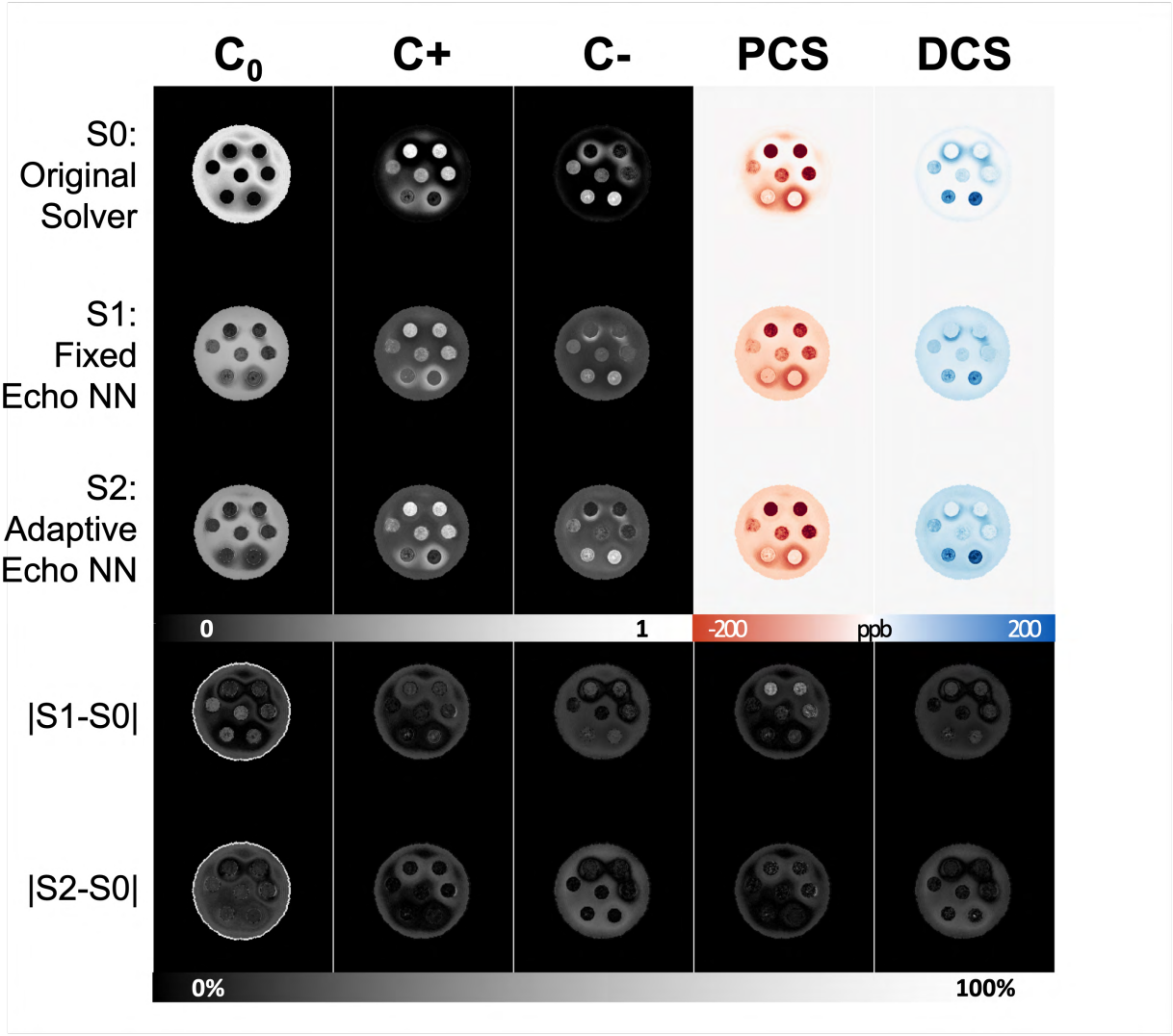

Figure 7.4: **Results of parameter maps from the deep learning solvers compared to the original solver for the susceptibility mixture phantom scan.** The difference map is calculated as the absolute difference of each corresponding map from S1 (or S2) to S0.

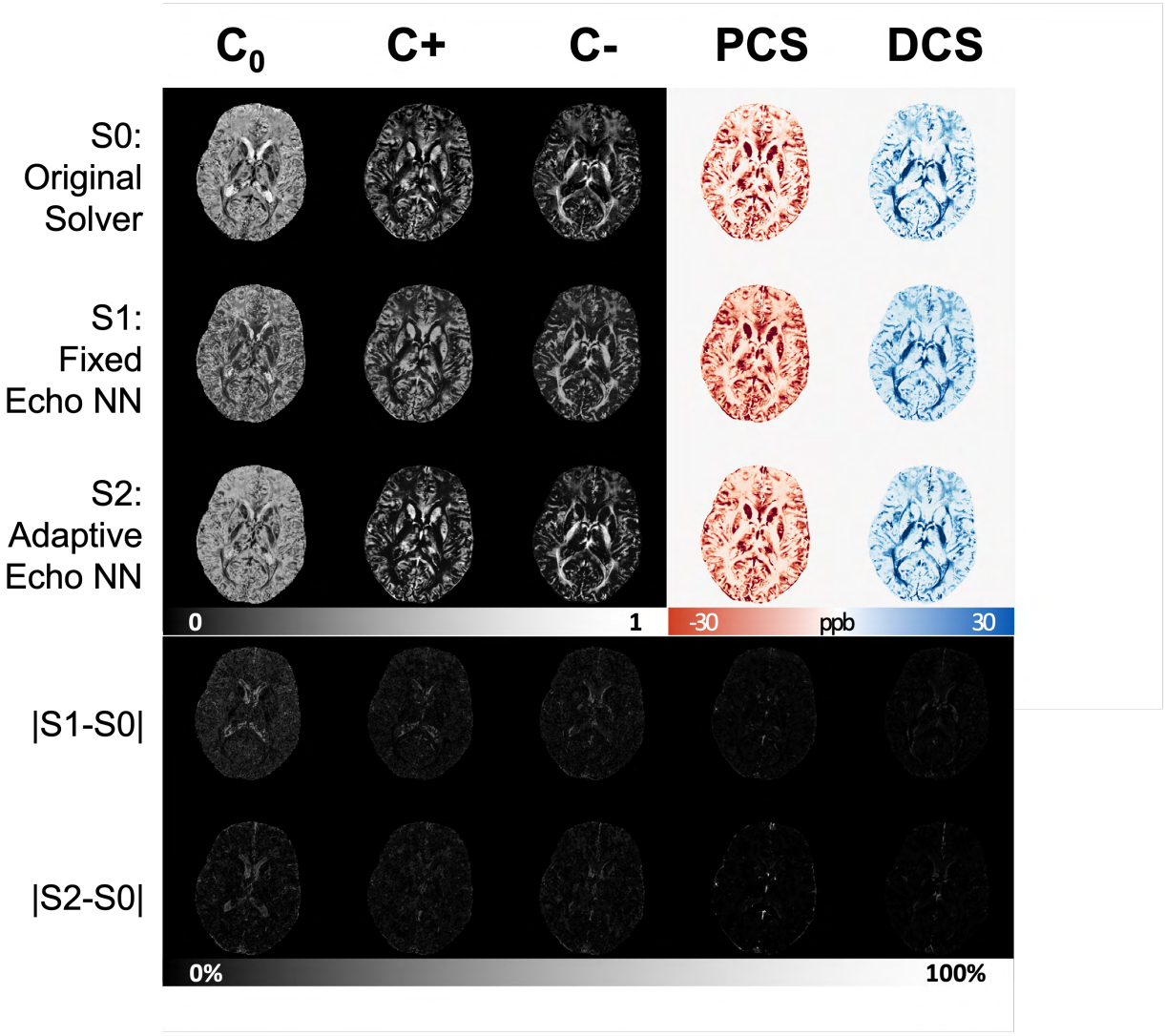

Figure 7.5: **Results of parameter maps from the deep learning solvers compared to the original solver for a healthy subject brain scan.** The difference map is calculated as the absolute difference of each corresponding map from S1 (or S2) to S0.

7.2 Phase Filtering Methods Impact Susceptibility Estimation

Phase filtering is a very important step in obtaining a good susceptibility and susceptibility tensor estimation. The background filtering step is shared by both QSM and STI reconstructions. As an illustration, We compare and show the effects of different phase processing methods on the quality of susceptibility tensor reconstruction with different numbers of orientations.

7.2.1 Introduction

STI reconstruction generally follows the pipeline shown in Figure 7.6: phase of the GRE signal is unwrapped and filtered to remove the background field, followed by aligning measurements from all angles to one reference orientation. Several background phase removal algorithms exist and they have a significant impact on the accuracy of QSM maps[93, 41]. Since STI measures susceptibility variations across different orientations, variations due to phase processing will introduce errors in the tensor estimation. Here, we compare six commonly used methods of phase filtering in two tensor reconstruction methods to investigate the effects of background phase removal methods on the quality of STI.

7.2.2 Methods

GRE data of a postmortem mouse brain were collected at 19 orientations[75]. Briefly, the imaging parameters were: B0 = 7T, TE/TR = 8.0/50 ms, voxelsize =0.08 mm isotropic.

The phase was unwrapped with the Laplacian-based phase unwrapping method[67]. Afterward, six major phase filtering methods were included in the test. Sources of MATLAB scripts are as follows: Sophisticated Harmonic Artifact Reduction for Phase[102] (SHARP), Laplacian Boundary Value[141] (LBV) and Regularization-enabled SHARP[115] (RESHARP) ware obtained from online resources (`QSMGitHubRepo;https://github.com/sunhongfu/QSM`), Projection onto dipole fields[79] (PDF) was obtained from MEDI toolbox[79](`http://pre.weill.cornell.edu/mri/pages/qsm.html`), improved HARmonic (background) PhasE REmovaL using the Laplacian operator[66] (iHARPERELLA) and Variable-radius SHARP [130] (VSHARP) were obtained from STISuite(`https://people.eecs.berkeley.edu/~chunlei.liu/software.html`). All methods were used with masks with potential boundary erosion size considered, ensuring the output tissue phase is in the same shape and size. Parameters used for each method are iHARPERELLA: padsize=12; RESHARP: kernel size=3, tolerance=0.001; LBV: tolerance=0.01; SHARP: kernel size=3; tolerance=0.05; V-SHARP: smvsize=12.

Registration was performed using ITKsnap[137] on each orientation's magnitude image. After manual alignment with the reference volume, a mutual information metric was used to obtain affine transformations, which were then applied to the filtered phase. Regular

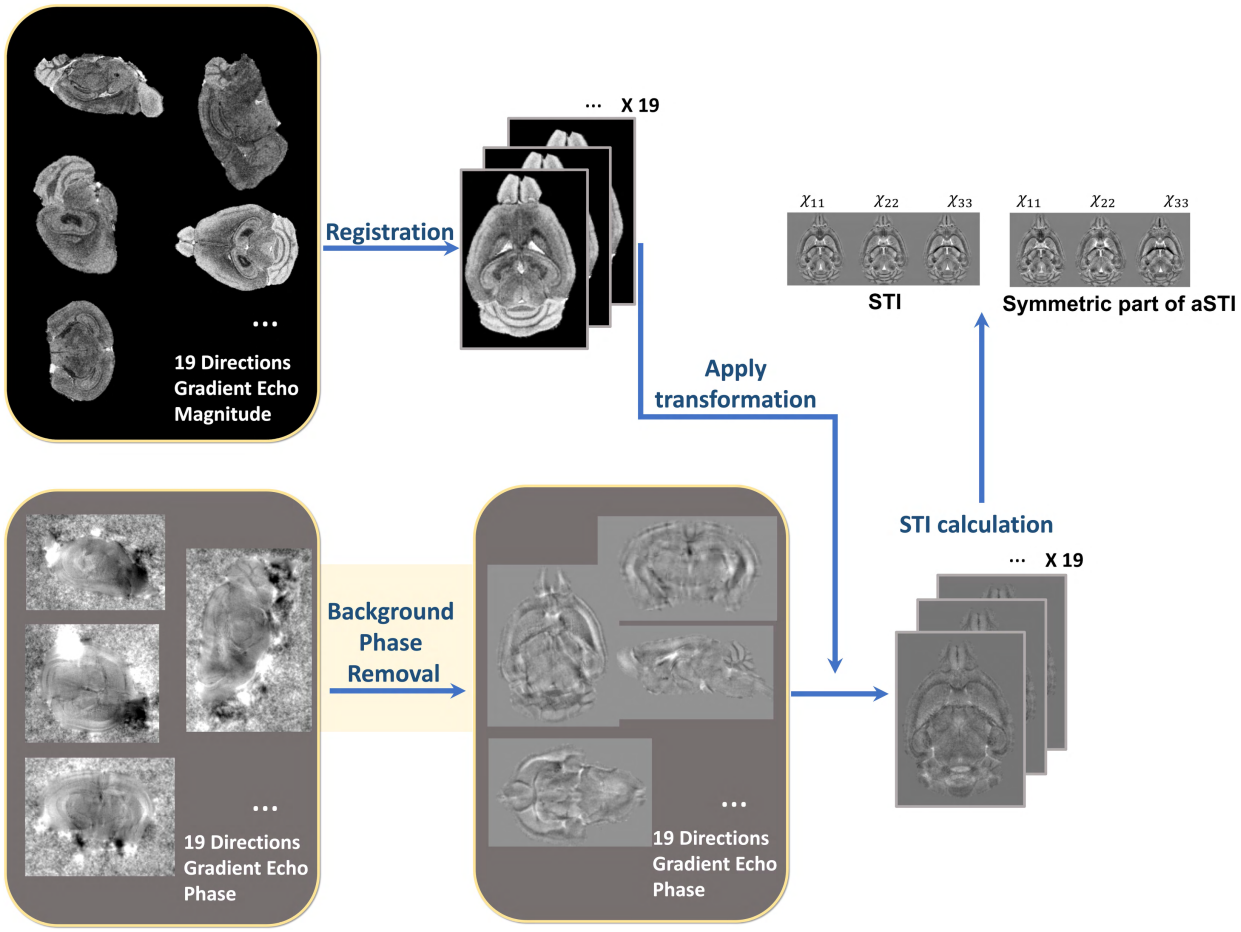

Figure 7.6: **General pipeline of susceptibility tensor reconstruction.** The background phase removal step is a key step. Many algorithms are developed to achieve accurate local tissue phase estimation. The key part of this study is to investigate how different phase filtering methods affect the final tensor results.

symmetric STI[74] reconstruction and the recently introduced asymmetric STI[24] (aSTI) were used to reconstruct the tensor. Susceptibility anisotropy defined as $SA = eigVal(1) - (eigVal(2) + eigVal(3))/2$ was calculated from eigen decomposition of the tensor (the first eigenvalue is the largest). This SA quantity was used to weigh the primary eigenvector in color-coded maps.

7.2.3 Results

The iHARPERELLA, PDF, and LBV methods result in tensor maps with significant variations that appear artificial as seen from the "dark" patches (Figure 7.7). On the other hand, the SHARP, RESHARP, and V-SHARP methods produce relatively consistent tensor maps that are free of such large "dark" patches (Figure 7.7). Interestingly, regardless of the phase processing method, the artifacts seen in Figure 7.7 are significantly reduced by using aSTI reconstruction (Figure 7.8). The corresponding SA-weighted primary eigenvector RGB map also shows similar results: variations of SHARP give vector maps that are more spatially coherent and aSTI is more robust to phase artifacts (Figure 7.9). All methods, regardless of the reconstruction algorithm used, have increased noise with decreasing orientation number and fail to produce meaningful results at 6 measurement orientations (Figure 7.10).

7.2.4 Discussion

It was previously reported[41] that LBV and PDF are more accurate for noiseless data in simulations, however, for *in vivo* cases, where there exist large frequency shifts caused by air-water boundaries (e.g. sinus), SHARP-based methods outperform LBV and PDF. We have observed similar effects. The artifacts from large air bubbles on the boundary of the *ex vivo* sample were successfully filtered by RESHARP, SHARP, and V-SHARP (Figures 7.7 and 7.8). More importantly, the phase filtering errors associated with iHARPERELLA, PDF, and LBV vary significantly between orientations, resulting in significant errors in the tensor estimation and subsequently in the eigenvectors and eigenvalues. While these errors are prominent in the original symmetric STI reconstruction, aSTI is known[24] to be more robust by absorbing artifacts into the antisymmetric part of the tensor. With both STI and aSTI, it's consistently observed that variations of the SHARP (SHARP, RESHARP, V-SHARP) methods and iHARPERELLA return more coherent eigenvectors.

As expected, tensors computed from all filtering methods become noisier with fewer directions. All methods failed when only 6 orientations of measurements were used, which suggests the minimum number of orientations needed for STI is 6 due to the lack of precise a priori control of the orientations.

Note that every method included here contains some level of flexibility in parameters tuning, while PDF requires pre-estimated noise level maps for better performance. The parameters used in this study were chosen to achieve reasonable results through visual inspections. The proper parameter choice may vary depending on the quality of the raw unwrapped phase, which requires further systematic investigation.

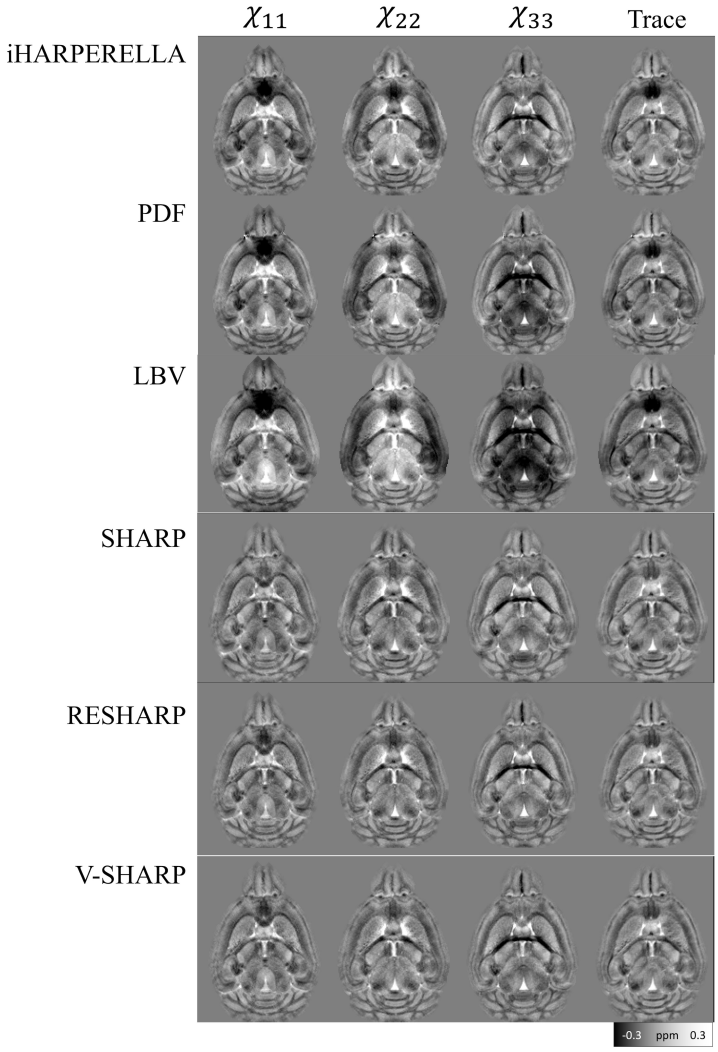

Figure 7.7: **STI elements from different filtering methods.** Original STI: Tensor reconstructed with the symmetry constraint using 6 different phase filtering methods. SHARP, RESHARP, and V-SHARP show the least artifacts in the diagonal tensor elements. In terms of the most artifacts, LBV particularly shows the most prominent artificial features.

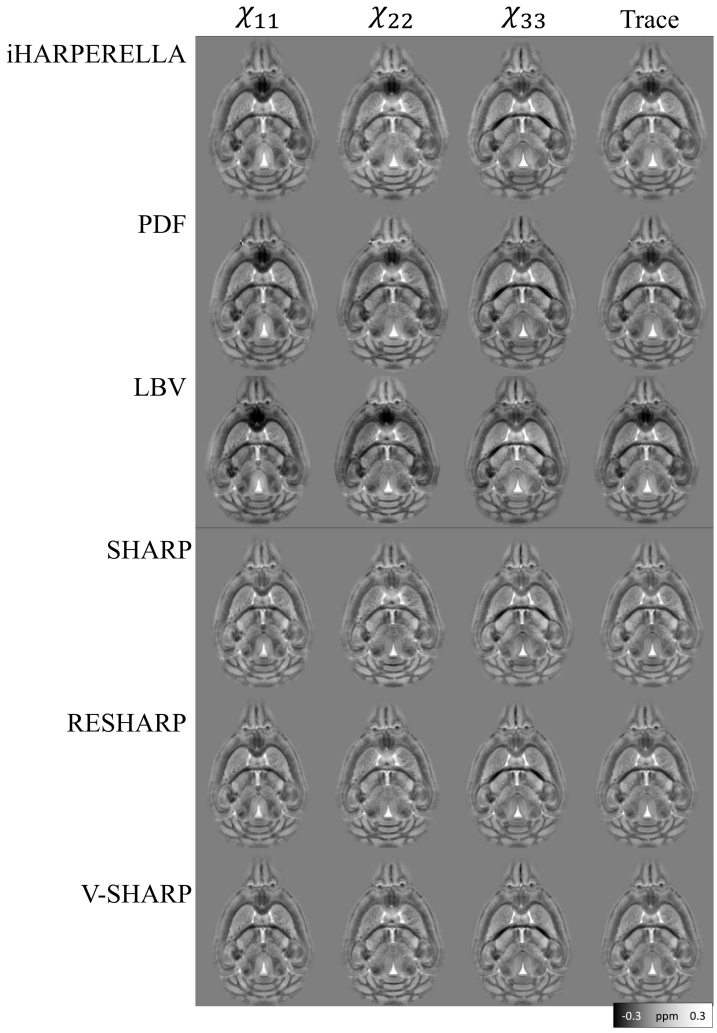

Figure 7.8: **aSTI elements from different filtering methods.** Asymmetric STI: Tensor reconstructed without the symmetry constraint using 6 different phase filtering methods. The diagonal elements shown here are from the symmetric part of the asymmetric susceptibility tensor. Tensor elements show reduced artifacts compared to Figure 7.7. Overall, SHARP, RESHARP, and V-SHARP show the least artifacts in the tensor elements.

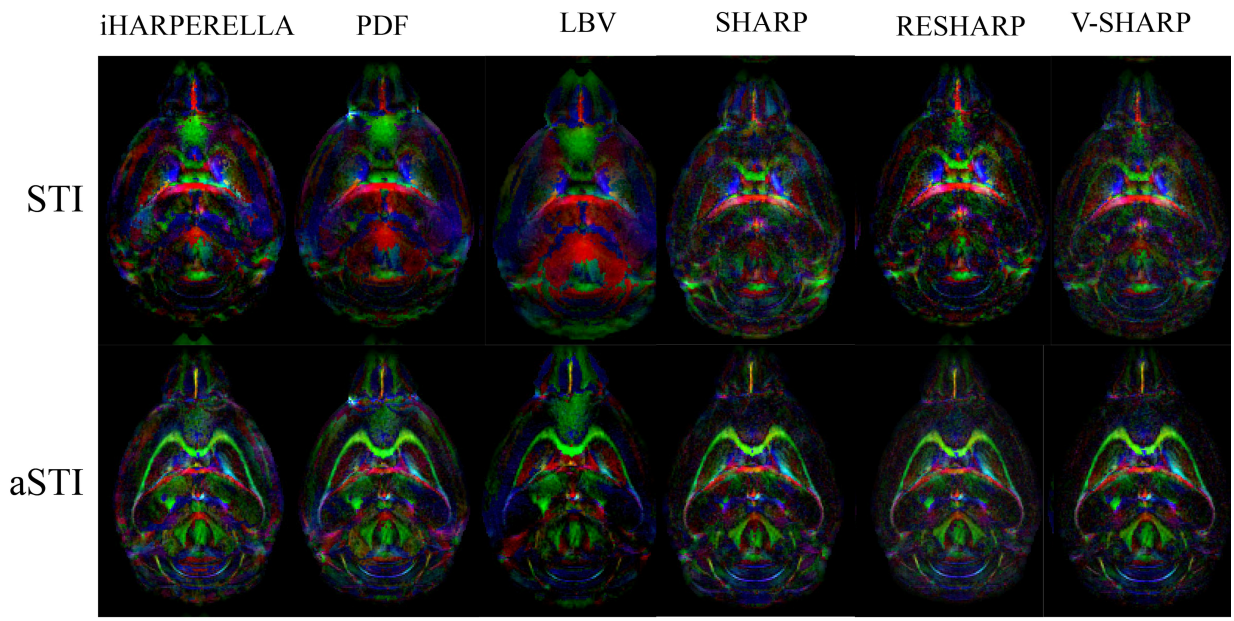

Figure 7.9: **The susceptibility anisotropy (SA) weighted primary eigenvector RGB map.** SHARP, V-SHARP and RESHARP show the most spatially coherent eigenvectors. aSTI reconstruction appears to be more robust in revealing susceptibility anisotropy even with phase artifacts. Green:L-R, Red: A-P; Blue: S-I.

7.2.5 Conclusion

V-SHARP, RESHARP, and SHARP showed the most robustness towards large field perturbations, resulting in the most consistent tensor estimations. The aSTI method outperforms the conventional STI method in reducing phase filtering artifacts. With the same phase data, different phase filtering methods (or parameter choices) may yield informative or nearly useless susceptibility anisotropy information. It is therefore critical to ensure that the background phase removal process was done properly and consistently across different orientations.

7.3 QSM scaling affects DECOMPOSE-QSM results

One of the inputs for DECOMPOSE-QSM is the QSM of each echo. Many methods have been published to calculate QSM as described in Chapter 2.5. Due to the various assumptions each algorithm makes, recovered QSM of the same raw data with different methods can be different. With combinations of different phase unwrapping, filtering, and dipole inversion methods, resulting QSM can be underestimated, overestimated, or contains artifacts.

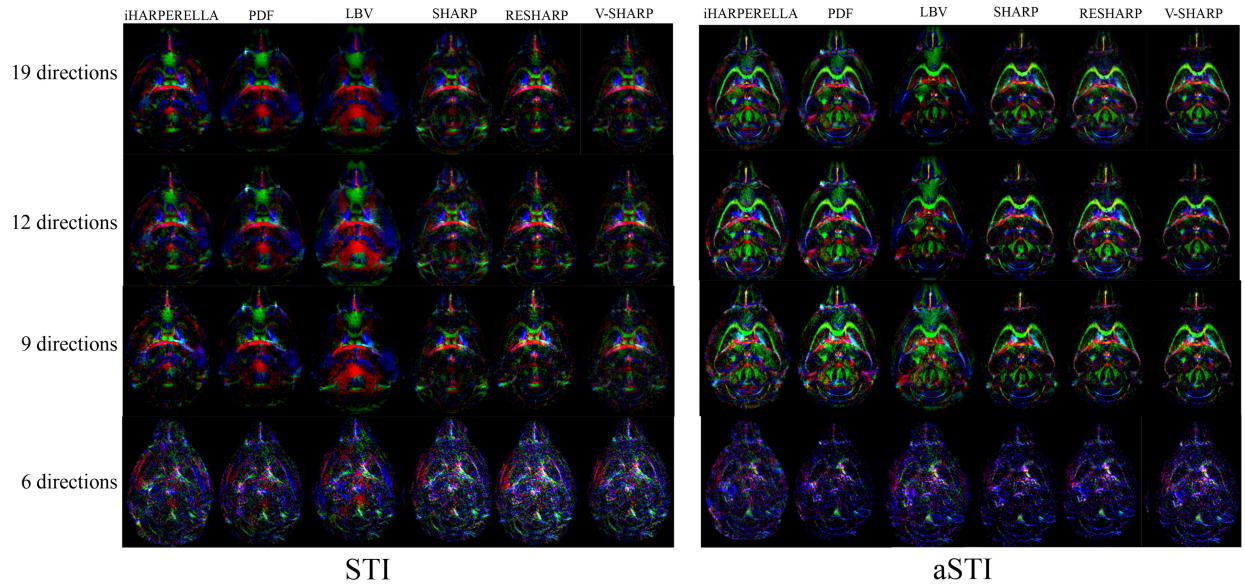

Figure 7.10: **Number of orientations for STI reconstruction.** The susceptibility anisotropy (SA) weighted primary eigenvector RGB map for 19, 12, 9, and 6 different directions of measurements. All methods crash when only 6 orientations are available. RESHARP and V-SHARP return the most reliable susceptibility tensor. At 9 orientations, the external capsule still stands out in REAHRP and V-SHARP filtered phase with conventional STI reconstruction. Green:L-R, Red: A-P; Blue: S-I.

The DECOMPOSE-QSM model relied on the relation between R_2^* and the underlying susceptibility, and if the initial input QSM is inaccurate or being scaled, the relationship that DECOMPOSE-QSM relies on theoretically will be violated. Here we explore the sensitivity of DECOMPOSE-QSM results to the scaling of QSM input.

7.3.1 Methods

Image data of one healthy subject was used for the experiments. Data was previously used in Chapter 3 where the processing details can be found. Briefly, the multi-echo GRE scan was performed on the axial plane with the following parameters: TE1/spacing/TE16 = 2.7/2.9/46.2 ms, TR = 59.3 ms, B0 = 3 T, and a spatial resolution of $0.86 \times 0.86 \times 1.0\,\text{mm}^3$. The raw phase was unwrapped using a Laplacian-based phase unwrapping method, followed by V-SHARP background field removal and STAR-QSM calculation.

The calculated QSM is scaled manually by various factors: 0.4, 0.6, 0.8, 1.2, 1.4, 1.6, and 1.8 before sending it into the DECOMPOSE-QSM solver. The magnitude images remain unchanged. According to the definition and analysis in Chapter 3, if the algorithm performs

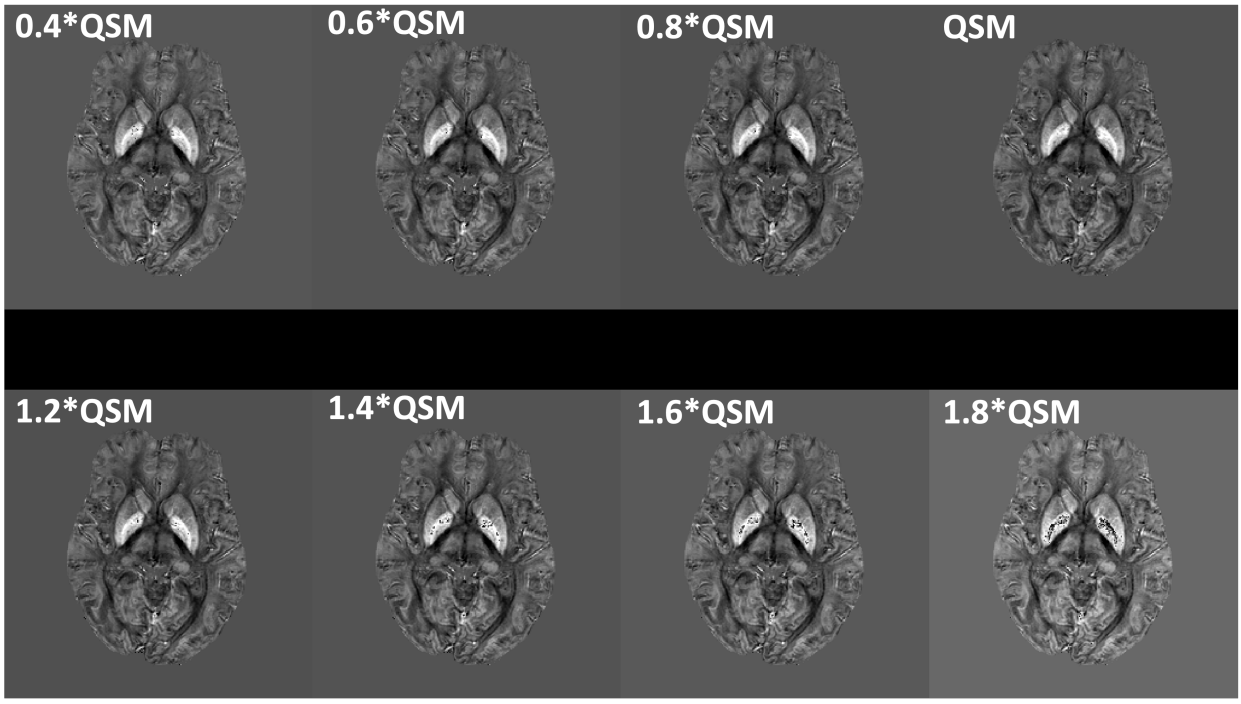

Figure 7.11: **Composite susceptibility from DECOMPOSE-QSM of QSM input with various scaling factors.** The artifacts in the deep gray matter are seen for both underestimated and overestimated QSM. The overestimation cases show stronger artifacts than the underestimation cases.

successfully, the composite susceptibility(Eq. 7.1) calculated using the DECOMPOSE-QSM model should match the average QSM from the input.

$$\text{Composite susceptibility} = \frac{\sum_t \angle\left(\left(C_+ e^{-\left(a\chi_+ + i\frac{2}{3}\chi_+\gamma B0\right)t} + C_- e^{-\left(-a\chi_- + i\frac{2}{3}\chi_-\gamma B0\right)t} + C_0\right) e^{-R^*_{2,0}t}\right)}{\frac{2}{3}\gamma B_0 \sum t} \tag{7.1}$$

In the case that the DECOMPOSE-QSM calculation fails, the composite susceptibility will not match the echo-averaged input QSM and show artifacts.

7.3.2 Results

The scaling of QSM can exist during either the phase filtering process or the QSM dipole inversion process. Here, simulations by manually scaling the input QSM values show that either underestimation or overestimation of QSM will give the mismatch of the composite susceptibility and the input mean QSM indicating the failure of the DECOMPOSE-QSM calculation. Specifically, in Figure 7.11, the globus pallidus region shows the most artifact.

It seems that the underestimation of the QSM value will give fewer artifacts than the case of QSM overestimation. The results indicate that the current DECOMPOSE-QSM cost function is sensitive to the QSM value variations and it is now optimized based on the STAR-QSM results as described in Chapter 3. Further investigation is needed to find a proper QSM normalization mechanism before the calculation of DECOMPOSE-QSM. It is worth noting that this simulation only concerns the case of linear scaling, it does not consider other types of artifacts such as over-smoothing, streaking artifacts, noise amplification, etc.

Chapter 8

Summary

8.1 Contribution

This dissertation presents DECOMPOSE-QSM, an MR signal modeling approach to resolve the paramagnetic and diamagnetic susceptibility's mixture situation in quantitative susceptibility mapping. The voxel signal model and the optimization-based solver are validated by imaging susceptibility phantoms and observing Curie's Law with the temperature variant experiment. With the DECOMPOSE-QSM approach, a multi-orientation dataset of a postmortem chimpanzee brain and susceptibility second-order tensor model, paramagnetic susceptibility anisotropy was observed for the first time using an MRI-based mechanism.

8.2 Potential applications of DECOMPOSE-QSM

The signal model and the proposed solver of DECOMPOSE-QSM may be applied to many scientific and clinical topics:

1. **Brain structures:** PCS maps in Figure 3.4, 3.5, 3.7 showed clear traces of veins and small paramagnetic clusters which are disguised by diamagnetic components in conventional QSM. The DCS maps on healthy subjects' images showed more complete white matter tracks than threshold QSM. The C_0 maps corresponding to the low susceptibility fluid reveal clear delineation of the subthalamic nuclei [34, 65, 140]. These parameter maps could provide a new tool to study brain structures and to understand brain development with a longitudinal dataset.

2. **Neurodegenerative diseases:** Chapter 5 briefly explored one application of DECOMPOSE-QSM being used to increase the sensitivity of the iron overload biomarker of Parkinson's Disease. In Figure 5.1, the statistical significance of PCS in different regions of the brain are in good agreement with QSM reported in previous studies. Iron has been reported to be involved in neurodegenerative diseases [9, 20, 56, 87]. In the case of AD, iron overload is known to facilitate the aggregation of

tau-protein and beta-amyloid aggregation. Although a previous study reported iron oxidation state dependency of QSM and R_2^* [17]. Specifically, according to their report, R2* decreased by about 2 Hz in both white matter and the cortex when ferric iron is reduced to ferrous iron. For the current setting of the DECOMPOSE QSM model, such subtle variations from oxidation state dependency are unlikely to be resolved. With the proposed DECOMPOSE-QSM, it is worth investigating if iron deposition and protein aggregation can be separated to assist in the characterization of the underlying pathology.

3. **Demyelination diseases:** The ability of DECOMPOSE-QSM to separate sub-voxel paramagnetic and diamagnetic susceptibility may be useful for imaging demyelination diseases such as multiple sclerosis (MS). Demyelination and iron accumulation can both occur in MS lesions which cannot be differentiated by QSM [51, 85, 128]. This issue may be addressed with DECOMPOSE-QSM.

4. **Susceptibility anisotropy:** The DECOMPOSE-QSM model is compatible with susceptibility anisotropy in white matter [72, 126]. While DCS is expected to be anisotropic in white matter, PCS is expected to be isotropic. By separating out the anisotropic component, DCS may be beneficial to improve the estimation of susceptibility tensor. However, in the previous Chapter 6, using 61-orientation measurements of a postmortem chimpanzee brain and DECOMPOSE-STI, we discovered susceptibility anisotropy for PCS. More work can be done to investigate the origin of PCS anisotropy. By separating susceptibility contribution, DECOMPOSE-STI may be more beneficial in revealing tissue microstructures than the conventional STI model.

8.3 Future directions

Some future directions can be taken to investigate the limitations of this dissertation:

1. **Model update for DECOMPOSE-QSM:** The proposed 3-pool model signal equation is highly simplified with the assumptions of the susceptibility source being spherical and relaxation following a theory at the static dephasing regime. Further improvement of the method may incorporate the variations of susceptibility source geometries and the effect of diffusion.

2. **Model update for DECOMPOSE-STI:** STI and DECOMPOSE-STI show promising results and potential in revealing tissue microstructure in addition to the DTI. However, sometimes STI results do not align and are even perpendicular to the DTI, especially in the cortical region (Figure 6.10C). This could be due to a few reasons: 1) the Gaussian diffusion model fails at the cortical region; 2) the tissue structure is too complicated for the simple single exponential STI model; 3) the susceptibility estimation could lose accuracy due to artifacts as the voxel gets closer to the surface of the brain; 4) the origin of the diffusion anisotropy and susceptibility anisotropy

are fundamentally different. A previous study (Reveley et al., 2022) has found that diffusion MRI FA did not match the spatial distribution of myelin in the gray matter but it matches closer to the Nissl stained tissue anisotropy. More sophisticated tissue microstructure diffusion models and susceptibility models are needed to coordinate different underlying effects that may contribute to the tissue anisotropy measurements.

3. **Clinical application of DECOMPOSE-QSM:** For the *in vivo* PD vs. controls study in Chapter 5, DCS showed significant differences in multiple regions in addition to PCS differences. The differences in DCS between the two groups may suggest changes in myelination. However, further studies including *ex vivo* validation are needed. Additionally, DECOMPOSE-QSM can be integrated with studies concerning Alzheimer's Disease and other neurodegenerative diseases as DECOMPOSE-QSM can provide additional quantitative information on pathological tissue changes.

4. **Validating experiments for the PCS anisotropy:** In Chapter 6, the paramagnetic susceptibility anisotropy was observed with a postmortem chimpanzee brain. We provided one hypothesis: the geometric arrangement of the iron-bearing tissue is the source of the anisotropy. However, to justify and further investigate the existence and the origin of the paramagnetic susceptibility anisotropy, an iron-washed brain tissue sample could be deployed and followed by the same imaging experiment setups. Additionally, higher resolution STI datasets, polarized light imaging (PLI) on sample slices, or the Nissl staining-based tensor reconstruction could provide additional information and validation.

5. **Data representation and interpretation of PCS and DCS based tensor imaging:** The QSM-based SA and eigenvector maps appear to be some kind of combination of the PCS and DCS-based maps. From the initial visual comparison, the DCS-STI is more reliable when tissue is more diamagnetic and the SA of DCS is higher. The effect is likewise for PCS-STI. A method to properly combine PCS-STI and DCS-STI eigenvector maps could help reveal a more coherent and reliable STI vector map.

6. **Explore the impact from QSM referencing to the DECOMPOSE-QSM results:** Throughout the studies within this dissertation, except for the validation phantom work, no referencing process is done to the QSM values. It should not be an issue as the sample is a healthy brain, and the mean susceptibility value of the whole brain should be around zero [69, 113]. However, when investigating a brain with pathologies or tissue with a non-balanced amount of diamagnetic/paramagnetic content, referencing procedure is needed prior to computing the DECOMPOSE-QSM.

7. **Explore the impact from STI reconstruction regularization strategy to the DECOMPOSE-STI results:** Since the introduction of susceptibility tensor imaging, many STI reconstruction advances have been proposed [8, 15, 24, 39, 73, 127] to improve the robustness of reconstructing STI as well as to reconstruct reliable tensors

with as few orientations as possible. Those methods could be integrated together with the susceptibility source separation method to further extract more reliable information on the tissue susceptibility properties.

8. **Solver update for DECOMPOSE-QSM:**The algorithm relies on an accurate echo-time-dependent QSM input. If the QSM input is inaccurate, the algorithm will have an inaccurate phase to work with, then the resulting maps can be confounding. The interpretations of the individual parameters and further improving the accuracies of χ_+,χ_- at low concentration levels are still under investigation. Despite that, it is noteworthy that the composite maps (PCS and DCS) are highly accurate based on simulation and phantom experiments; the maps also enhance the contrast between paramagnetic components and diamagnetic components.

9. **Network design update for DeepDECOMPOSE:** The MLP-based framework for DECOMPOSE-QSM parameter searching shows promising results: the DeepDECOMPOSE is more robust to spatial noise and the accuracy for PCS and DCS is very high compared to the optimization-based solver. However, there are some discrepancies between the DeepDECOMPOSE and the original solver for the concentration C maps. The use of C maps is to be explored. The current setup of DeepDECOMPOSE might hinder the exploration of the C maps. An unrolled scheme could be deployed to bridge the gap between the optimization model-based solver and the MLP-based solver. Alternatively, an MLP could be used for the expensive step of searching for $\chi_{+/-}$ parameters and C parameters can be recovered using a traditional constraint least square solver.

Chapter 9

Appendix

9.1 Transverse relaxation rate at the static dephasing regime

The linear relationship between R_2^* and susceptibility is observed *in vivo* [129], and *ex vivo* [6, 53]. The relaxation theory of MR signal behavior at the static dephasing regime provides the quantification of this linearity as follows [23, 133],

$$R_2' = \frac{2\pi}{9\sqrt{3}}\mu_0\gamma\left|\Delta M\right|\delta = \frac{2\pi}{9\sqrt{3}}\gamma B_0\left|\Delta\chi\right| \ , \tag{9.1}$$

where B_0 is the external static magnetic field, μ_0 is the vacuum magnetic permeability, ΔM is the magnetization (referenced to neutral medium), γ is the gyromagnetic ratio, δ is the volume fraction of the particle of the susceptibility sources, and $\Delta\chi$ is the measurable volume susceptibility corresponding to the values in QSM (referenced to neutral medium).

The size of the susceptibility source affects the applicability of this theory [21]. Specifically, the theory of static dephasing fits better in cell settings than in nanoparticle settings. In our proposed model, susceptibility sources are treated as clusters of particles or molecules rather than individual particles or molecules of ions or lipids, which is a suitable application of the theory of transverse relaxation at the static dephasing regime, thus

$$R_2^* = R_2' + R_2 = \frac{2\pi}{9\sqrt{3}}\gamma B_0\left|\Delta\chi\right| + R_2 \ . \tag{9.2}$$

The transverse relaxation rate R_2, resulting from spin-spin interaction, is a function of local field shift, diffusion, and other intrinsic processes. The theoretical quantification of such can be derived using quantum mechanics with some proper approximations [19, 60, 94]. In the current situation, this value is being treated as a parameter to be estimated rather than pre-measured or pre-analyzed.

9.2 Magnetic field of a uniformly magnetized sphere

The source of the magnetic susceptibility is modeled as a uniformly magnetized sphere. The field of the interior of a sphere with uniformly distributed susceptibility χ situating in a static magnetic field with a strength of B_0 is

$$B_{z,in} = \frac{2}{3}\mu_0 M_0 = \frac{2}{3}\chi B_0 \tag{9.3}$$

while the field (at location r) outside such a sphere (with a radius of R_0, locating at r_0) is equivalent to a dipole field,

$$B_{z,out}\left(\theta,\ r, r_0\right) = \frac{\chi B_0 R_0^3}{3\left(r - r_0\right)^3}(3\cos^2\theta - 1). \tag{9.4}$$

Bibliography

[1] Julio Acosta-Cabronero et al. "The whole-brain pattern of magnetic susceptibility perturbations in Parkinson's disease". In: *Brain* 140.1 (2017), pp. 118–131. DOI: 10.1093/brain/aww278.

[2] Adriano Aguzzi and Tracy O'Connor. "Protein aggregation diseases: pathogenicity and therapeutic perspectives". In: *Nature Reviews Drug Discovery* 9.3 (2010), pp. 237–248. DOI: 10.1038/nrd3050.

[3] Amjad I. AlTokhis et al. "Iron Rims as an Imaging Biomarker in MS: A Systematic Mapping Review". In: *Diagnostics* 10.11 (2020), p. 968. DOI: 10.3390/diagnostics10110968.

[4] Beatrice Arezzini et al. "Iron overload enhances the development of experimental liver cirrhosis in mice". In: *The International Journal of Biochemistry & Cell Biology* 35.4 (2003), pp. 486–495. DOI: 10.1016/S1357-2725(02)00298-4.

[5] Ioannis Argyridis et al. "Quantitative magnetic susceptibility of the developing mouse brain reveals microstructural changes in the white matter". In: *NeuroImage* 88 (2014), pp. 134–142. DOI: 10.1016/j.neuroimage.2013.11.026.

[6] Francesca Bagnato et al. "Untangling the R2* contrast in multiple sclerosis: A combined MRI-histology study at 7.0 Tesla". In: *PLOS ONE* 13.3 (2018). Ed. by Quan Jiang, e0193839. DOI: 10.1371/journal.pone.0193839.

[7] Chris J. G. Bakker, Hendrik de Leeuw, and Peter R. Seevinck. "Selective depiction of susceptibility transitions using Laplace-filtered phase maps". In: *Magnetic Resonance Imaging* 30.5 (2012), pp. 601–609. DOI: 10.1016/j.mri.2011.12.023.

[8] Lijun Bao et al. "Diffusion-regularized susceptibility tensor imaging (DRSTI) of tissue microstructures in the human brain". In: *Medical Image Analysis* 67 (2021), p. 101827. DOI: 10.1016/j.media.2020.101827.

[9] Jeam Haroldo Oliveira Barbosa et al. "Quantifying brain iron deposition in patients with Parkinson's disease using quantitative susceptibility mapping, R2 and R2*". In: *Magnetic Resonance Imaging* 33.5 (2015), pp. 559–565. DOI: 10.1016/j.mri.2015.02.021.

[10] Abdel A. Belaidi and Ashley I. Bush. "Iron neurochemistry in Alzheimer's disease and Parkinson's disease: targets for therapeutics". In: *Journal of Neurochemistry* 139.S1 (2016), pp. 179–197. DOI: 10.1111/jnc.13425.

[11] Dorit Ben-Shachar, P. Riederer, and M. B. H. Youdim. "Iron-Melanin Interaction and Lipid Peroxidation: Implications for Parkinson's Disease". In: *Journal of Neurochemistry* 57.5 (1991), pp. 1609–1614. DOI: 10.1111/j.1471-4159.1991.tb06358.x.

[12] J. M. G. van Bergen et al. "Colocalization of cerebral iron with Amyloid beta in Mild Cognitive Impairment". In: *Scientific Reports* 6.1 (2016), p. 35514. DOI: 10.1038/srep35514.

[13] Matthew J. Betts et al. "High-resolution characterisation of the aging brain using simultaneous quantitative susceptibility mapping (QSM) and R2* measurements at 7T". In: *NeuroImage* 138 (2016), pp. 43–63. DOI: 10.1016/j.neuroimage.2016.05.024.

[14] Berkin Bilgic et al. "MRI estimates of brain iron concentration in normal aging using quantitative susceptibility mapping". In: *NeuroImage* 59.3 (2012), pp. 2625–2635. DOI: 10.1016/j.neuroimage.2011.08.077.

[15] Berkin Bilgic et al. "Rapid multi-orientation quantitative susceptibility mapping". In: *NeuroImage* 125 (2016), pp. 1131–1141. DOI: 10.1016/j.neuroimage.2015.08.015.

[16] Christoph Birkl et al. "Iron mapping using the temperature dependency of the magnetic susceptibility". In: *Magnetic Resonance in Medicine* 73.3 (2015), pp. 1282–1288. DOI: 10.1002/mrm.25236.

[17] Christoph Birkl et al. "The influence of iron oxidation state on quantitative MRI parameters in post mortem human brain". In: *NeuroImage* 220 (2020), p. 117080. DOI: 10.1016/j.neuroimage.2020.117080.

[18] F. Bloch. "Line-Narrowing by Macroscopic Motion". In: *Physical Review* 94.2 (1954), pp. 496–497. DOI: 10.1103/PhysRev.94.496.2.

[19] N. Bloembergen and L. O. Morgan. "Proton Relaxation Times in Paramagnetic Solutions. Effects of Electron Spin Relaxation". In: *The Journal of Chemical Physics* 34.3 (1961), pp. 842–850. DOI: 10.1063/1.1731684.

[20] Fatima Bousejra-ElGarah et al. "Iron(II) Binding to Amyloid-, the Alzheimer's Peptide". In: *Inorganic Chemistry* 50.18 (2011), pp. 9024–9030. DOI: 10.1021/ic201233b.

[21] Chris V. Bowen et al. "Application of the static dephasing regime theory to superparamagnetic iron-oxide loaded cells". In: *Magnetic Resonance in Medicine* 48.1 (2002), pp. 52–61. DOI: https://doi.org/10.1002/mrm.10192.

[22] Valentina Brainovich, Umberto Sabatini, and Gisela E. Hagberg. "Advantages of using multiple-echo image combination and asymmetric triangular phase masking in magnetic resonance venography at 3 T". In: *Magnetic Resonance Imaging* 27.1 (2009), pp. 23–37. DOI: 10.1016/j.mri.2008.05.006.

[23] Robert J. S. Brown. "Distribution of Fields from Randomly Placed Dipoles: Free-Precession Signal Decay as Result of Magnetic Grains". In: *Physical Review* 121.5 (1961), pp. 1379–1382. DOI: 10.1103/PhysRev.121.1379.

[24] Steven Cao et al. "Asymmetric susceptibility tensor imaging". In: *Magnetic Resonance in Medicine* 86.4 (2021), pp. 2266–2275. DOI: 10.1002/mrm.28823.

[25] Jingjia Chen et al. "Decompose quantitative susceptibility mapping (QSM) to sub-voxel diamagnetic and paramagnetic components based on gradient-echo MRI data". In: *NeuroImage* 242 (2021), p. 118477. DOI: 10.1016/j.neuroimage.2021.118477.

[26] Weiwei Chen et al. "Quantitative Susceptibility Mapping of Multiple Sclerosis Lesions at Various Ages". In: *Radiology* 271.1 (2013), pp. 183–192. DOI: 10.1148/radiol.13130353.

[27] Petrice M. Cogswell et al. "Associations of quantitative susceptibility mapping with Alzheimer's disease clinical and imaging markers". In: *NeuroImage* 224 (2021), p. 117433. DOI: 10.1016/j.neuroimage.2020.117433.

[28] Matthew J. Cronin et al. "Exploring the origins of echo-time-dependent quantitative susceptibility mapping (QSM) measurements in healthy tissue and cerebral microbleeds". In: *NeuroImage* 149 (2017), pp. 98–113. DOI: 10.1016/j.neuroimage.2017.01.053.

[29] J. T. Curnes et al. "MR imaging of compact white matter pathways." In: *American Journal of Neuroradiology* 9.6 (1988), pp. 1061–1068.

[30] Alfredo De Goyeneche et al. "ResoNet: Physics Informed Deep Learning based Off-Resonance Correction Trained on Synthetic Data". In: *Proceedings of the 31st ISMRM Annual Meeting*. 2022.

[31] Dinesh K. Deelchand et al. "Across-vendor standardization of semi-LASER for single-voxel MRS at 3T". In: *NMR in Biomedicine* n/a.n/a (), e4218. DOI: https://doi.org/10.1002/nbm.4218.

[32] Andreas Deistung, Ferdinand Schweser, and Jürgen R. Reichenbach. "Overview of quantitative susceptibility mapping". In: *NMR in Biomedicine* 30.4 (2017), e3569. DOI: https://doi.org/10.1002/nbm.3569.

[33] Andreas Deistung et al. "Quantitative Susceptibility Mapping Differentiates between Blood Depositions and Calcifications in Patients with Glioblastoma". In: *PLOS ONE* 8.3 (2013), e57924. DOI: 10.1371/journal.pone.0057924.

[34] Andreas Deistung et al. "Toward in vivo histology: A comparison of quantitative susceptibility mapping (QSM) with magnitude-, phase-, and R2∗-imaging at ultra-high magnetic field strength". In: *NeuroImage* 65 (2013), pp. 299–314. DOI: 10.1016/j.neuroimage.2012.09.055.

[35] Mahlon R. DeLong and Thomas Wichmann. "Basal Ganglia Circuits as Targets for Neuromodulation in Parkinson Disease". In: *JAMA Neurology* 72.11 (2015), pp. 1354–1360. DOI: 10.1001/jamaneurol.2015.2397.

[36] Paul J. Derry et al. "Revisiting the intersection of amyloid, pathologically modified tau and iron in Alzheimer's disease from a ferroptosis perspective". In: *Progress in Neurobiology* 184 (2020), p. 101716. DOI: 10.1016/j.pneurobio.2019.101716.

[37] Alexey V. Dimov et al. "Susceptibility source separation from gradient echo data using magnitude decay modeling". In: *Journal of Neuroimaging: Official Journal of the American Society of Neuroimaging* 32.5 (2022), pp. 852–859. DOI: 10.1111/jon.13014.

[38] Cornelius Eichner et al. "Increased sensitivity and signal-to-noise ratio in diffusion-weighted MRI using multi-echo acquisitions". In: *NeuroImage* 221 (2020), p. 117172. DOI: 10.1016/j.neuroimage.2020.117172.

[39] Zhenghan Fang et al. *DeepSTI: Towards Tensor Reconstruction using Fewer Orientations in Susceptibility Tensor Imaging*. 2022. DOI: 10.48550/arXiv.2209.04504.

[40] Ruimin Feng et al. "MoDL-QSM: Model-based deep learning for quantitative susceptibility mapping". In: *NeuroImage* 240 (2021), p. 118376. DOI: 10.1016/j.neuroimage.2021.118376.

[41] Véronique Fortier and Ives R. Levesque. "Phase processing for quantitative susceptibility mapping of regions with large susceptibility and lack of signal". In: *Magnetic Resonance in Medicine* 79.6 (2018), pp. 3103–3113. DOI: 10.1002/mrm.26989.

[42] Gamsu G et al. "A preliminary study of MRI quantification of simulated calcified pulmonary nodules." In: *Investigative Radiology* 22.11 (1987), pp. 853–858. DOI: 10.1097/00004424-198711000-00001.

[43] Dimitrios G. Gkotsoulias et al. *High Angular Resolution Susceptibility Imaging and Estimation of Fiber Orientation Distribution Functions in Primate Brain*. 2022. DOI: 10.1101/2022.10.23.513390.

[44] Nan-Jie Gong et al. "Imaging beta amyloid aggregation and iron accumulation in Alzheimer's disease using quantitative susceptibility mapping MRI". In: *NeuroImage* 191 (2019), pp. 176–185. DOI: 10.1016/j.neuroimage.2019.02.019.

[45] Nan-Jie Gong et al. "Imaging microstructure with diffusion and susceptibility MR: neuronal density correlation in Disrupted-in-Schizophrenia-1 mutant mice". In: *NMR in Biomedicine* 33.10 (2020), e4365. DOI: https://doi.org/10.1002/nbm.4365.

[46] Mario E. Götz et al. "The Relevance of Iron in the Pathogenesis of Parkinson's Disease". In: *Annals of the New York Academy of Sciences* 1012.1 (2004), pp. 193–208. DOI: 10.1196/annals.1306.017.

[47] Xiaojun Guan et al. "Influence of regional iron on the motor impairments of Parkinson's disease: A quantitative susceptibility mapping study". In: *Journal of Magnetic Resonance Imaging* 45.5 (2017), pp. 1335–1342. DOI: 10.1002/jmri.25434.

[48] Xiaojun Guan et al. "Quantitative susceptibility mapping as a biomarker for evaluating white matter alterations in Parkinson's disease". In: *Brain Imaging and Behavior* 13.1 (2019), pp. 220–231. DOI: 10.1007/s11682-018-9842-z.

[49] Xiaojun Guan et al. "Regionally progressive accumulation of iron in Parkinson's disease as measured by quantitative susceptibility mapping". In: *NMR in Biomedicine* 30.4 (2017), e3489. DOI: https://doi.org/10.1002/nbm.3489.

[50] E. Mark Haacke et al. "Susceptibility weighted imaging (SWI)". In: *Magnetic Resonance in Medicine* 52.3 (2004), pp. 612–618. DOI: https://doi.org/10.1002/mrm.20198.

[51] Simon Hametner et al. "Iron and neurodegeneration in the multiple sclerosis brain". In: *Annals of Neurology* 74.6 (2013), pp. 848–861. DOI: 10.1002/ana.23974.

[52] Simon Hametner et al. "The influence of brain iron and myelin on magnetic susceptibility and effective transverse relaxation - A biochemical and histological validation study". In: *NeuroImage* 179 (2018), pp. 117–133. DOI: 10.1016/j.neuroimage.2018.06.007.

[53] Jane S. Hankins et al. "R2* magnetic resonance imaging of the liver in patients with iron overload". In: *Blood* 113.20 (2009), pp. 4853–4855. DOI: 10.1182/blood-2008-12-191643.

[54] Naying He et al. "Dentate nucleus iron deposition is a potential biomarker for tremor-dominant Parkinson's disease". In: *NMR in biomedicine* 30.4 (2017), 10.1002/nbm.3554. DOI: 10.1002/nbm.3554.

[55] Naying He et al. "Region-specific disturbed iron distribution in early idiopathic Parkinson's disease measured by quantitative susceptibility mapping". In: *Human Brain Mapping* 36.11 (2015), pp. 4407–4420. DOI: https://doi.org/10.1002/hbm.22928.

[56] Kurt A. Jellinger. "The Role of Iron in Neurodegeneration". In: *Drugs & Aging* 14.2 (1999), pp. 115–140. DOI: 10.2165/00002512-199914020-00004.

[57] Mark Jenkinson et al. "FSL". In: *NeuroImage*. 20 YEARS OF fMRI 62.2 (2012), pp. 782–790. DOI: 10.1016/j.neuroimage.2011.09.015.

[58] Woojin Jung et al. "Exploring linearity of deep neural network trained QSM: QSMnet+". In: *NeuroImage* 211 (2020), p. 116619. DOI: 10.1016/j.neuroimage.2020.116619.

[59] Hyug-Gi Kim et al. "Quantitative susceptibility mapping to evaluate the early stage of Alzheimer's disease". In: *NeuroImage : Clinical* 16 (2017), pp. 429–438. DOI: 10.1016/j.nicl.2017.08.019.

[60] Seymour H. Koenig and Kenneth E. Kellar. "Theory of 1/T1 and 1/T2 NMRD profiles of solutions of magnetic nanoparticles". In: *Magnetic Resonance in Medicine* 34.2 (1995), pp. 227–233. DOI: https://doi.org/10.1002/mrm.1910340214.

[61] Christian Langkammer et al. "Quantitative Susceptibility Mapping in Parkinson's Disease". In: *PLOS ONE* 11.9 (2016), e0162460. DOI: 10.1371/journal.pone.0162460.

[62] Jingu Lee et al. "Separating positive and negative susceptibility sources in QSM". In: *ISMRM, HONOLULU, HI, USA, MRM.[Google Scholar]* (2017).

[63] Jongho Lee et al. "T2*-based fiber orientation mapping". In: *NeuroImage* 57.1 (2011), pp. 225–234. DOI: 10.1016/j.neuroimage.2011.04.026.

[64] Sang-Pil Lee et al. "Visualization of -amyloid plaques in a transgenic mouse model of Alzheimer's disease using MR microscopy without contrast reagents". In: *Magnetic Resonance in Medicine* 52.3 (2004), pp. 538–544. DOI: https://doi.org/10.1002/mrm.20196.

[65] Jun Li et al. "Imaging the Centromedian Thalamic Nucleus Using Quantitative Susceptibility Mapping". In: *Frontiers in Human Neuroscience* 13 (2020). DOI: 10.3389/fnhum.2019.00447.

[66] Wei Li, Bing Wu, and Chunlei Liu. "an improved method for integrated 3D phase unwrapping and background phase removal." In: (2015), p. 3313.

[67] Wei Li, Bing Wu, and Chunlei Liu. "Quantitative susceptibility mapping of human brain reflects spatial variation in tissue composition". In: *NeuroImage* 55.4 (2011), pp. 1645–1656. DOI: 10.1016/j.neuroimage.2010.11.088.

[68] Wei Li et al. "A method for estimating and removing streaking artifacts in quantitative susceptibility mapping". In: *NeuroImage* 108 (2015), pp. 111–122. DOI: 10.1016/j.neuroimage.2014.12.043.

[69] Wei Li et al. "Differential developmental trajectories of magnetic susceptibility in human brain gray and white matter over the lifespan". In: *Human Brain Mapping* 35.6 (2014), pp. 2698–2713. DOI: https://doi.org/10.1002/hbm.22360.

[70] Wei Li et al. "Integrated Laplacian-based phase unwrapping and background phase removal for quantitative susceptibility mapping". In: *NMR in Biomedicine* (2018), pp. 219–227. DOI: 10.1002/nbm.3056@10.1002/(ISSN)1099-1492.NMR-in-Biomedicine:30-Year-Celebration.

[71] Wei Li et al. "Magnetic susceptibility anisotropy of human brain in vivo and its molecular underpinnings". In: *NeuroImage* 59.3 (2012), pp. 2088–2097. DOI: 10.1016/j.neuroimage.2011.10.038.

[72] Wei Li et al. "Susceptibility tensor imaging (STI) of the brain". In: *NMR in Biomedicine* 30.4 (2017), e3540. DOI: https://doi.org/10.1002/nbm.3540.

[73] Xu Li and Peter C. M. van Zijl. "Mean magnetic susceptibility regularized susceptibility tensor imaging (MMSR-STI) for estimating orientations of white matter fibers in human brain". In: *Magnetic Resonance in Medicine* 72.3 (2014), pp. 610–619. DOI: 10.1002/mrm.25322.

[74] Chunlei Liu. "Susceptibility Tensor Imaging". In: *Magnetic resonance in medicine : official journal of the Society of Magnetic Resonance in Medicine / Society of Magnetic Resonance in Medicine* 63.6 (2010), pp. 1471–1477. DOI: 10.1002/mrm.22482.

[75] Chunlei Liu et al. "3D fiber tractography with susceptibility tensor imaging". In: *NeuroImage* 59.2 (2012), pp. 1290–1298. DOI: 10.1016/j.neuroimage.2011.07.096 .

[76] Chunlei Liu et al. "High-field (9.4T) MRI of brain dysmyelination by quantitative mapping of magnetic susceptibility". In: *NeuroImage* 56.3 (2011), pp. 930–938. DOI: 10.1016/j.neuroimage.2011.02.024.

[77] Chunlei Liu et al. "Quantitative Susceptibility Mapping: Contrast Mechanisms and Clinical Applications". In: *Tomography* 1.1 (2015), pp. 3–17. DOI: 10.18383/j.tom .2015.00136.

[78] Chunlei Liu et al. "Susceptibility-weighted imaging and quantitative susceptibility mapping in the brain: Brain Susceptibility Imaging and Mapping". In: *Journal of Magnetic Resonance Imaging* 42.1 (2015), pp. 23–41. DOI: 10.1002/jmri.24768.

[79] Tian Liu et al. "A novel background field removal method for MRI using projection onto dipole fields (PDF)". In: *NMR in biomedicine* 24.9 (2011), pp. 1129–1136. DOI: 10.1002/nbm.1670.

[80] Tian Liu et al. "Calculation of susceptibility through multiple orientation sampling (COSMOS): A method for conditioning the inverse problem from measured magnetic field map to susceptibility source image in MRI". In: *Magnetic Resonance in Medicine* 61.1 (2009), pp. 196–204. DOI: https://doi.org/10.1002/mrm.21828.

[81] Tian Liu et al. "Morphology enabled dipole inversion (MEDI) from a single-angle acquisition: Comparison with COSMOS in human brain imaging". In: *Magnetic Resonance in Medicine* 66.3 (2011), pp. 777–783. DOI: https://doi.org/10.1002/mrm .22816.

[82] J. Lounila et al. "Effects of orientational order and particle size on the NMR line positions of lipoproteins". In: *Physical Review Letters* 72.25 (1994), pp. 4049–4052. DOI: 10.1103/PhysRevLett.72.4049.

[83] Mark D. Meadowcroft et al. "MRI and histological analysis of beta-amyloid plaques in both human Alzheimer's disease and APP/PS1 transgenic mice". In: *Journal of Magnetic Resonance Imaging* 29.5 (2009), pp. 997–1007. DOI: 10.1002/jmri.21731.

[84] Reiko Meguro et al. "Cellular and subcellular localizations of nonheme ferric and ferrous iron in the rat brain: a light and electron microscopic study by the perfusion-Perls and -Turnbull methods". In: *Archives of Histology and Cytology* 71.4 (2008), pp. 205–222. DOI: 10.1679/aohc.71.205.

[85] Veela Mehta et al. "Iron is a sensitive biomarker for inflammation in multiple sclerosis lesions". In: *PloS One* 8.3 (2013), e57573. DOI: 10.1371/journal.pone.0057573.

[86] Y. Murakami et al. "Usefulness of Quantitative Susceptibility Mapping for the Diagnosis of Parkinson Disease". In: *American Journal of Neuroradiology* 36.6 (2015), pp. 1102–1108. DOI: 10.3174/ajnr.A4260.

[87] Alain Ndayisaba, Christine Kaindlstorfer, and Gregor K. Wenning. "Iron in Neurodegeneration – Cause or Consequence?" In: *Frontiers in Neuroscience* 13 (2019). DOI: 10.3389/fnins.2019.00180.

[88] José A. Obeso et al. "Pathophysiology of the basal ganglia in Parkinson's disease". In: *Trends in Neurosciences* 23 (2000), S8–S19. DOI: 10.1016/S1471-1931(00)00028-8.

[89] Se-Hong Oh et al. "Direct visualization of short transverse relaxation time component (ViSTa)". In: *NeuroImage* 83 (2013), pp. 485–492. DOI: 10.1016/j.neuroimage.2013.06.047.

[90] Ana-Maria Oros-Peusquens et al. "A Single-Scan, Rapid Whole-Brain Protocol for Quantitative Water Content Mapping With Neurobiological Implications". In: *Frontiers in Neurology* 10 (2019).

[91] Adam Paszke et al. "PyTorch: An Imperative Style, High-Performance Deep Learning Library". In: *Advances in Neural Information Processing Systems 32*. Curran Associates, Inc., 2019, pp. 8024–8035.

[92] Marie A Philippe, Richard G Ruddell, and Grant A Ramm. "Role of iron in hepatic fibrosis: One piece in the puzzle". In: *World Journal of Gastroenterology : WJG* 13.35 (2007), pp. 4746–4754. DOI: 10.3748/wjg.v13.i35.4746.

[93] Simon Daniel Robinson et al. "An illustrated comparison of processing methods for MR phase imaging and QSM: combining array coil signals and phase unwrapping: Phase image combination and unwrapping". In: *NMR in Biomedicine* 30.4 (2017), e3601. DOI: 10.1002/nbm.3601.

[94] Alain Roch, Robert N. Muller, and Pierre Gillis. "Theory of proton relaxation induced by superparamagnetic particles". In: *The Journal of Chemical Physics* 110.11 (1999), pp. 5403–5411. DOI: 10.1063/1.478435.

[95] Pascal P. R. Ruetten, Jonathan H. Gillard, and Martin J. Graves. "Introduction to Quantitative Susceptibility Mapping and Susceptibility Weighted Imaging". In: *The British Journal of Radiology* 92.1101 (2019), p. 20181016. DOI: 10.1259/bjr.20181016.

[96] Tom W. J. Scheenen, Arend Heerschap, and Dennis W. J. Klomp. "Towards 1H-MRSI of the human brain at 7T with slice-selective adiabatic refocusing pulses". In: *Magma (New York, N.y.)* 21.1-2 (2008), pp. 95–101. DOI: 10.1007/s10334-007-0094-y.

[97] John F. Schenck. "Imaging of brain iron by magnetic resonance: T2 relaxation at different field strengths". In: *Journal of the Neurological Sciences* 134 (1995), pp. 10–18. DOI: 10.1016/0022-510X(95)00203-E.

[98] Marvin A. Schofield and Yimei Zhu. "Fast phase unwrapping algorithm for interferometric applications". In: *Optics Letters* 28.14 (2003), pp. 1194–1196. DOI: 10.1364/ol.28.001194.

[99] Roey Schurr and Aviv A. Mezer. "The glial framework reveals white matter fiber architecture in human and primate brains". In: *Science* 374.6568 (2021), pp. 762–767. DOI: 10.1126/science.abj7960.

[100] F Schweser et al. "SEMI-TWInS: simultaneous extraction of myelin and iron using a T2*-weighted imaging sequence". In: *Proceedings of the 19th Meeting of the International Society for Magnetic Resonance in Medicine*. 2011, p. 120.

[101] Ferdinand Schweser et al. "Disentangling contributions from iron and myelin architecture to brain tissue magnetic susceptibility by using Quantitative Susceptibility Mapping (QSM)". In: 20 (2012), p. 409.

[102] Ferdinand Schweser et al. "Quantitative imaging of intrinsic magnetic tissue properties using MRI signal phase: An approach to in vivo brain iron metabolism?" In: *NeuroImage* 54.4 (2011), pp. 2789–2807. DOI: 10.1016/j.neuroimage.2010.10.070.

[103] Anwar S. Shatil, Kant M. Matsuda, and Chase R. Figley. "A Method for Whole Brain Ex Vivo Magnetic Resonance Imaging with Minimal Susceptibility Artifacts". In: *Frontiers in Neurology* 7 (2016). DOI: 10.3389/fneur.2016.00208.

[104] Yuting Shi et al. "Regularized Asymmetric Susceptibility Tensor Imaging in the Human Brain in Vivo". In: *IEEE Journal of Biomedical and Health Informatics* 26.9 (2022), pp. 4508–4518. DOI: 10.1109/JBHI.2022.3182969.

[105] Hyeong-Geol Shin et al. "-separation: Magnetic susceptibility source separation toward iron and myelin mapping in the brain". In: *NeuroImage* 240 (2021), p. 118371. DOI: 10.1016/j.neuroimage.2021.118371.

[106] Henrik Sjöström et al. "Quantitative susceptibility mapping differentiates between parkinsonian disorders". In: *Parkinsonism & Related Disorders* 44 (2017), pp. 51–57. DOI: 10.1016/j.parkreldis.2017.08.029.

[107] J. Slotboom and W. M. M. J. Bovée. "Adiabatic slice-selective rf pulses and a single-shot adiabatic localization pulse sequence". In: *Concepts in Magnetic Resonance* 7.3 (1995), pp. 193–217. DOI: https://doi.org/10.1002/cmr.1820070303.

[108] Stephen M. Smith et al. "Advances in functional and structural MR image analysis and implementation as FSL". In: *NeuroImage*. Mathematics in Brain Imaging 23 (2004), S208–S219. DOI: 10.1016/j.neuroimage.2004.07.051.

[109] Surabhi Sood et al. "Echo time based influences on quantitative susceptibility mapping". In: (2016).

[110] Surabhi Sood et al. "Echo time-dependent quantitative susceptibility mapping contains information on tissue properties". In: *Magnetic Resonance in Medicine* 77.5 (2017), pp. 1946–1958. DOI: https://doi.org/10.1002/mrm.26281.

[111] Nitish Srivastava et al. "Dropout: A Simple Way to Prevent Neural Networks from Overfitting". In: *Journal of Machine Learning Research* 15.56 (2014), pp. 1929–1958.

[112] Sina Straub et al. "Potential of quantitative susceptibility mapping for detection of prostatic calcifications". In: *Journal of Magnetic Resonance Imaging* 45.3 (2017), pp. 889–898. DOI: https://doi.org/10.1002/jmri.25385.

[113] Sina Straub et al. "Suitable reference tissues for quantitative susceptibility mapping of the brain". In: *Magnetic Resonance in Medicine* 78.1 (2017), pp. 204–214. DOI: 10.1002/mrm.26369.

[114] Carsten Stüber et al. "Myelin and iron concentration in the human brain: A quantitative study of MRI contrast". In: *NeuroImage* 93 (2014), pp. 95–106. DOI: 10.1016/j.neuroimage.2014.02.026.

[115] Hongfu Sun and Alan H. Wilman. "Background field removal using spherical mean value filtering and Tikhonov regularization". In: *Magnetic Resonance in Medicine* 71.3 (2014), pp. 1151–1157. DOI: 10.1002/mrm.24765.

[116] Neil D. Telling et al. "Iron Biochemistry is Correlated with Amyloid Plaque Morphology in an Established Mouse Model of Alzheimer's Disease". In: *Cell Chemical Biology* 24.10 (2017), 1205–1215.e3. DOI: 10.1016/j.chembiol.2017.07.014.

[117] Peter Verwilst et al. "Shedding light on tau protein aggregation: the progress in developing highly selective fluorophores". In: *Chemical Society Reviews* 47.7 (2018), pp. 2249–2265. DOI: 10.1039/C7CS00706J.

[118] Josef Vymazal et al. "The relation between brain iron and NMR relaxation times: An in vitro study". In: *Magnetic Resonance in Medicine* 35.1 (1996), pp. 56–61. DOI: 10.1002/mrm.1910350108.

[119] Chaoyue Wang et al. "Quantitative Susceptibility Mapping for Characterization of Intraplaque Hemorrhage and Calcification in Carotid Atherosclerotic Disease". In: *Journal of Magnetic Resonance Imaging* 52.2 (2020), pp. 534–541. DOI: https://doi.org/10.1002/jmri.27064.

[120] Nian Wang et al. "Probing demyelination and remyelination of the cuprizone mouse model using multimodality MRI". In: *Journal of Magnetic Resonance Imaging* 50.6 (2019), pp. 1852–1865. DOI: 10.1002/jmri.26758.

[121] Yi Wang and Tian Liu. "Quantitative susceptibility mapping (QSM): Decoding MRI data for a tissue magnetic biomarker". In: *Magnetic Resonance in Medicine* 73.1 (2015), pp. 82–101. DOI: https://doi.org/10.1002/mrm.25358.

[122] Hongjiang Wei et al. "Imaging diamagnetic susceptibility of collagen in hepatic fibrosis using susceptibility tensor imaging". In: *Magnetic Resonance in Medicine* 83.4 (2020), pp. 1322–1330. DOI: https://doi.org/10.1002/mrm.27995.

[123] Hongjiang Wei et al. "Streaking Artifact Reduction for Quantitative Susceptibility Mapping of Sources with Large Dynamic Range". In: *NMR in biomedicine* 28.10 (2015), pp. 1294–1303. DOI: 10.1002/nbm.3383.

[124] Hongjiang Wei et al. "Susceptibility tensor imaging and tractography of collagen fibrils in the articular cartilage". In: *Magnetic Resonance in Medicine* 78.5 (2017), pp. 1683–1690. DOI: 10.1002/mrm.26882.

[125] S. Wharton and R. Bowtell. "Fiber orientation-dependent white matter contrast in gradient echo MRI". In: *Proceedings of the National Academy of Sciences* 109.45 (2012), pp. 18559–18564. DOI: 10.1073/pnas.1211075109.

[126] Samuel Wharton and Richard Bowtell. "Effects of white matter microstructure on phase and susceptibility maps". In: *Magnetic Resonance in Medicine* 73.3 (2015), pp. 1258–1269. DOI: https://doi.org/10.1002/mrm.25189.

[127] Cynthia Wisnieff et al. "Magnetic susceptibility anisotropy: Cylindrical symmetry from macroscopically ordered anisotropic molecules and accuracy of MRI measurements using few orientations". In: *NeuroImage* 70 (2013), pp. 363–376. DOI: 10.1016/j.neuroimage.2012.12.050.

[128] Cynthia Wisnieff et al. "Quantitative susceptibility mapping (QSM) of white matter multiple sclerosis lesions: Interpreting positive susceptibility and the presence of iron: Iron and Myelin Content of MS Lesions with MRI". In: *Magnetic Resonance in Medicine* 74.2 (2015), pp. 564–570. DOI: 10.1002/mrm.25420.

[129] Bing Wu et al. "Fast and tissue-optimized mapping of magnetic susceptibility and T2* with multi-echo and multi-shot spirals". In: *NeuroImage*. Neuroergonomics: The human brain in action and at work 59.1 (2012), pp. 297–305. DOI: 10.1016/j.neuroimage.2011.07.019.

[130] Bing Wu et al. "Whole brain susceptibility mapping using compressed sensing". In: *Magnetic Resonance in Medicine* 67.1 (2012), pp. 137–147. DOI: 10.1002/mrm.23000.

[131] Luke Xie et al. "Quantitative susceptibility mapping of kidney inflammation and fibrosis in type 1 angiotensin receptor-deficient mice". In: *NMR in Biomedicine* 26.12 (2013), pp. 1853–1863. DOI: 10.1002/nbm.3039.

[132] Luke Xie et al. "Susceptibility tensor imaging of the kidney and its microstructural underpinnings". In: *Magnetic Resonance in Medicine* 73.3 (2015), pp. 1270–1281. DOI: 10.1002/mrm.25219.

[133] Dmitriy A. Yablonskiy and E. Mark Haacke. "Theory of NMR signal behavior in magnetically inhomogeneous tissues: The static dephasing regime". In: *Magnetic Resonance in Medicine* 32.6 (1994), pp. 749–763. DOI: 10.1002/mrm.1910320610.

[134] Sue Y. Yi et al. "Detecting Microglial Density With Quantitative Multi-Compartment Diffusion MRI". In: *Frontiers in Neuroscience* 13 (2019). DOI: 10.3389/fnins.2019.00081.

[135] Jaeyeon Yoon et al. "Quantitative susceptibility mapping using deep neural network: QSMnet". In: *NeuroImage* 179 (2018), pp. 199–206. DOI: 10.1016/j.neuroimage.2018.06.030.

[136] Koichi Yoshimura et al. "Development of a tissue-equivalent MRI phantom using carrageenan gel". In: *Magnetic Resonance in Medicine* 50.5 (2003), pp. 1011–1017. DOI: 10.1002/mrm.10619.

[137] Paul A. Yushkevich et al. "User-guided 3D active contour segmentation of anatomical structures: significantly improved efficiency and reliability". In: *NeuroImage* 31.3 (2006), pp. 1116–1128. DOI: 10.1016/j.neuroimage.2006.01.015.

[138] Quan-Guang Zhang et al. "Critical Role of NADPH Oxidase in Neuronal Oxidative Damage and Microglia Activation following Traumatic Brain Injury". In: *PLOS ONE* 7.4 (2012), e34504. DOI: 10.1371/journal.pone.0034504.

[139] Yan Zhang et al. "Longitudinal change in magnetic susceptibility of new enhanced multiple sclerosis (MS) lesions measured on serial quantitative susceptibility mapping (QSM): Magnetic Susceptibility Changes in MS". In: *Journal of Magnetic Resonance Imaging* 44.2 (2016), pp. 426–432. DOI: 10.1002/jmri.25144.

[140] Yuyao Zhang et al. "Longitudinal atlas for normative human brain development and aging over the lifespan using quantitative susceptibility mapping". In: *NeuroImage* 171 (2018), pp. 176–189. DOI: 10.1016/j.neuroimage.2018.01.008.

[141] Dong Zhou et al. "Background field removal by solving the Laplacian boundary value problem". In: *NMR in Biomedicine* 27.3 (2014), pp. 312–319. DOI: 10.1002/nbm.3064.